Retrospective Theses and Dissertations

Iowa State University Capstones, Theses and Dissertations

2007

Accurate electromagnetic full-wave modeling for interconnects in semiconductor integrated circuits

Lu Zhang
Iowa State University

Accurate electromagnetic full-wave modeling for interconnects in semiconductor integrated circuits

by

Lu Zhang

A dissertation submitted to the graduate faculty

in partial fulfillment of the requirements for the degree of

DOCTOR OF PHILOSOPHY

Major: Electrical Engineering

Program of Study Committee:
Jiming Song, Major Professor
Roger K. Alexander
John R. Bowler
Chris Chong-Nuen Chu
Robert J. Weber

Iowa State University

Ames, Iowa

2007

UMI Number: 3289397

UMI®

To my beloved Mom and Dad

TABLE OF CONTENTS

LIST OF TABLES

LIST OF FIGURES

ACKNOWLEDGEMENTS

I would like to express my gratitude to those who helped me with various aspects of conducting research and the writing of this dissertation.

First of all, I would like to thank my major professor, Dr. Jiming Song, for his direction, patience, and support throughout my Ph.D. study. His instructions, insights, and motivation always help me to proceed to the destiny. I have learned so much from his preciseness in every detail of academic research.

I would also like to thank my committee members for their valuable comments and suggestions to my research work: Dr. Roger K. Alexander, Dr. John R. Bowler, Dr. Chris Chong-Nuen Chu, and Dr. Robert J. Weber.

Finally, I sincerely thank my parents, who have supported me all these years. Their unconditional love and warm encouragement have often renewed my hopes for the future. Also, I would like to thank all my friends for their care and help in my life at Iowa State University.

ABSTRACT

Semiconductor-based integrated circuits have become the mainstream for very-large-scale integration systems such as high-speed digital circuits, radio-frequency integrated circuits, and even monolithic microwave integrated circuits. The shrinking feature size and increasing frequency promote high integration density and interconnection complexity that demand high-accuracy modeling techniques. The current design paradigm has shifted from the transistor-driven design to the interconnect-driven design. Thus the accurate electromagnetic full-wave modeling of on-chip interconnect becomes critical for the computer-aided design tools to analyze the overall system performance.

In this research, the full-wave spectral domain approach is implemented to investigate the electromagnetic properties of multilayered transmission lines with semiconductor substrates. In particular, finite thin metallization components, such as the thin metal ground layer and signal strips, are focused on. The thin metal ground layer is generally designed as a shield or a ground plane to depress the coupling and noise from neighboring components. But its fabricated thickness is often a small fraction of one micron, which may allow electromagnetic fields to penetrate through at some low frequencies. Such electromagnetic leakage phenomena play a significant role in the overall dispersive performance of transmission lines, and their consideration is inevitable.

For the spectral domain approach, the metallization layer can be rigorously modeled as a dielectric with a complex permittivity. However, due to the large conductivity of metal, the conventional transfer matrix method has potential overflow problems in obtaining the multilayered Green's function. In our research, a new formulation of the cascaded matrix is developed to overcome such numerical difficulties. Based on this formulation, the complete character-

istics of multilayered transmission lines with thin metallization components are studied by parameters like the propagation constant, attenuation per unit length, field distribution, characteristic impedance, transient response, and extracted resistance, inductance, capacitance, and conductance of equivalent circuits. The parallel-plate waveguide model is applied to study a metal-insulator-metal-semiconductor structure. The first- and second-order low-frequency approximations for the fundamental propagation mode are derived with corresponding equivalent circuit models. In addition, other approximate models for the thin metal ground are compared numerically to assess their validity.

Two transmission lines with the metal-insulator-metal-semiconductor and the metal-insulator-metal-insulator structures are analyzed. Numerical results indicate that the thin metallization components have significant impacts on the propagation characteristics. The thin metal layer can enhance or even excite the slow-wave mode. Thus, it is necessary to take these effects into account to achieve accurate and reliable analysis of integrated circuit interconnects from dc to millimeter-wave frequencies.

CHAPTER 1. INTRODUCTION

During the last three decades, the semiconductor-based integrated circuits (ICs), such as very-large-scale integration (VLSI) circuits, radio-frequency integrated circuits (RFICs), monolithic microwave and millimeter-wave integrated circuits, and high-speed digital circuits, have progressed rapidly. The operating frequency keeps increasing. And the feature size, defined as the smallest width that can be reliably manufactured on semiconductor wafers, goes into the deep submicron region. For example, current leading-edge technology is the 45 nm process (Intel, 2007). By 2020, according to the report of *International Technology Roadmap for Semiconductors* (ITRS) [1], the feature size will shrink to about 14 nm. In addition, many complex interconnect technologies, such as the multichip module, the hierarchical wiring topology, and multilevel and multilayered interconnect networks, have been introduced to promote high integration density. Chips stacking up to ten layers vertically through via connections have been widely adopted. The 3-dimensional packaging technology plus vertical integration has also been available.

However, such complicated interconnect structures also bring new challenges. Due to the reduction of device size and increase of overall chip size, the signal delays on interconnect networks become critical in determining the overall circuit performance. Currently the VLSI design paradigm is shifting from the conventional transistor-driven to the interconnect-driven design to satisfy the total technical requirements. Moreover, the high integration density makes circuits vulnerable to the harsh electromagnetic interference (EMI). The requirement of signal integrity demands that the computer-aided design (CAD) tools should accurately and efficiently predict the electrical properties of transmission systems. To accomplish this goal, the accurate modeling of electromagnetic (EM) properties of interconnects is the key [2].

The goal of the this research is the full-wave EM modeling and simulation for multilayered planar interconnects with imperfect finite metallization. The frequency range is from the sub-kilohertz to hundreds of gigahertz or even terahertz regimes. Specifically, in our research the effects of the thin-film metal ground and finite thin signal strips are focused on. The impacts on the overall transmission-line properties, such as propagation speed, loss, and characteristic impedance, are studied.

1.1 Research Motivation

The planar passive transmission lines are extensively implemented in ICs. Since high-speed digital chips and VLSI circuits can operate at a frequency of up to $100\,\mathrm{GHz}$, the interference between neighboring passive components rises remarkably with the scaling down of device size [3]. In particular, the consideration of crosstalk, couplings, power supply noises, ground bouncing, ringing, and electromagnetic radiation is inevitable across the whole circuits and chip-to-chip links.

To depress the interference, one widely used solution is to add properly designed neighboring metallization or highly conductive layers as ground planes. The inner metallic layer is usually fabricated with a thickness of only a small fraction of one micron. This uniform metal plane presents a current return path with very small impedance for all interconnects above and below. Fig. 1.1 illustrates examples of the metal-insulator-semiconductor (MIS), the thin-film microstrip line (TFMSL), the inverted embedded microstrip (IEM), and the patterned ground shield, in which thin metallization components are embedded.

Two major obstacles have been encountered for analyzing such structures. One is the broad frequency range. Signals and their harmonics in interconnects can spread in a broad frequency spectrum from dc up to even millimeter waves. The other is the impact of imperfect conductors with finite conductivities. For a good conductor, the EM waves cannot be completely shielded outside but rather decay exponentially inside the conductor. The $1/e$ attenuation distance is defined as the skin depth δ. For example, the skin depth of copper is around $2\,\mu\mathrm{m}$ at $1\,\mathrm{GHz}$, which is already larger than the metallization profiles fabricated in current VLSI circuits.
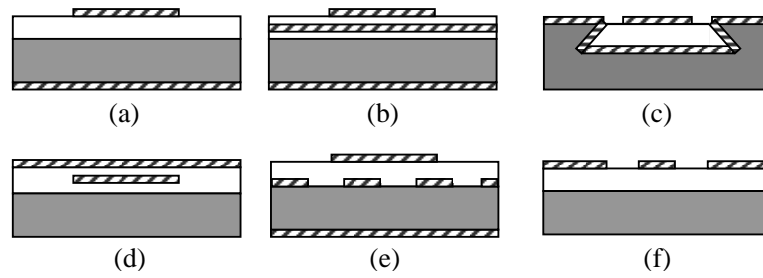
Figure 1.1: Multilayered transmission lines with thin metallization components: (a) metal-insulator-semiconductor microstrip line, (b) thin-film microstrip line, (c) suspended membrane microshielded line, (d) inverted embedded microstrip line, (e) MIS with patterned ground shield, (f) coplanar waveguide (region filled with diagonal lines: thin metallization, grey region: semiconductor, white region: dielectric or insulator).

Therefore, the EM fields can penetrate the conductors and reach substrates underneath at low frequencies, which consequentially influence the overall electric properties of interconnects. Moreover, signal strips, which account for the major part of propagation loss and attenuation, exhibit the skin effect and current proximity effect at high frequencies. The skin effect reveals that a majority of current is confined within small regions near the surfaces and corners. The current proximity effect is that current distribution tends to congregate due to neighboring conductors. Such EM penetration, skin effects, and current proximity effects are all frequency dependent and generate exponentially varying currents inside conductors, which are critical for the overall interconnect performance. However, these effects are so troublesome that they are usually neglected in today's CAD tools.

In addition, high accuracy demands are posed on CAD tools to model lossy transmission lines with via connections, which have become a generic trend in IC designs. Two aspects must be considered: the electromagnetic properties of passive components and the presence of lossy semiconductor layers. However, most present circuit-model-based CAD solvers are based on the static or quasi-static approximation. And the propagation waves are assumed to be the quasi-transverse electromagnetic (quasi-TEM) mode. These assumptions may eventually be violated due to the steady technology progress toward higher frequencies and EM wave phenomena of interconnects. In addition, most EM field-based solvers model the metallization components as the perfect electric conductor (PEC) or the impedance boundary condition

(IBC). These two boundary conditions (BCs) are impenetrable and improper in describing the EM penetrating phenomena as discussed before. So far no specific attention in the literature and measurement has been paid to the thin metal ground in multilayered structures.

To predict accurately the electrical performance of interconnects over a broad frequency range, the full-wave EM methodology is necessary. This dissertation investigates the interconnect structures with configurations of thin metal conductors. In our research, the imperfect conductor effects are systematically investigated by specific parameters such as the propagation constant (effective permittivity and slow wave factor); attenuation (loss) per unit length; characteristic impedance; equivalent resistance, inductance, capacitance, and conductance (RLCG) per unit length, and others. The resulting design rules should give designers the capabilities to simulate and explore interconnect easily and accurately.

1.2   Relevant Literature Review

Although the original microstrip line was introduced as early as the 1950s [4], the relevant planar transmission lines have played an important role in the advanced RF, microwave, and millimeter-wave technologies. Within these technologies, the analysis methodology is of fundamental importance.

Microstrip lines are planar transmission systems through which EM waves propagate. For multilayered structures, specifically, the problems belong to the guided waves theory and EM propagation in stratified media. These topics have been researched systematically for decades [5]-[7]. Early studies of microstrip lines were mostly based on empirical formulas from experimental data [8]. Apart from those, analyzing techniques are categorized into two main groups: static or quasi-static and dynamic or full-wave approaches [9].

The early theoretical work was primarily based on equivalent physical circuit models. The researchers used the quasi-TEM models that are valid only at dc and low frequencies. This model presumes that the propagation waves resemble the pure TEM modes by ignoring the longitudinal field components. Two techniques, the static and the quasi-static, have been developed for the quasi-TEM analysis. For the static analysis, electric and magnetic fields

are independent to each other. By solving the Laplace and Poisson equations, corresponding circuit parameters like the resistance, capacitance, and inductance are calculated from the static charges and current distributions. For the quasi-static analysis, electric and magnetic fields are coupled by the conductive current, whereas the displacement currents are neglected.

Many approaches have been proposed primarily based on the quasi-TEM assumption. Wheeler [10], [11] first studied the strip lines by the conformal mapping to evaluate the static capacitance. The variational method was applied by Yamashita and Mittra [12] and later by Medina and Horno [13]. Wei *et al.* [14] solved for the capacitance and inductance of multi-layered multiconductor transmission lines by using free-space Green's functions with total and polarization charges on interfaces. The quasi-TEM spectral domain analysis was introduced by Itoh [15] to solve the Poisson equation. Green [16] applied the finite difference (FD) method to solve the Laplace's equation for transmission lines.

Generally, the quasi-TEM analysis is computationally efficient but restricted to yield accurate results only at the low-frequency region. There is no clear-cut upper boundary of frequency to guarantee its validity. Moreover, with frequency increasing and structure being more complicated, the dispersive characteristics of microstrip lines become more dominant to invalidate the quasi-TEM assumption. Thus, all these characteristics promote the full-wave analysis techniques with regard to accuracy.

The full-wave analysis methods can analyze strictly the hybrid modes at any frequency by solving Maxwell's equations with specific BCs. Mathematically rigorous full-wave methods include the integral-equation-based method, such as the full-wave spectral domain approach (SDA), and the differential-equation-based method, such as the finite element method (FEM). The integral-equation-based methods require accurate Green's functions for the multilayered structures [17], [18]. In details, the Green's functions are derived either in the spatial domain or in the spectral domain. These two domains can be transformed into each other by the forward and inverse Fourier transformations. For example, the mixed-potential-integral-equation method obtains spatial Green's functions through so-called Sommerfeld integrals from the spectral domain to the spatial domain [19].

The SDA is an efficient method widely applied to the planar transmission lines, filters, and antennas. A brief review of relevant development for the SDA can be found in [20]-[26]. By the Fourier transformation, the differential equations are transformed from the spatial domain into the spectral domain so as to simplify the problem. The method of moments (MoM) is used to solve the integral equations, from which the characteristic equation is obtained by using the Galerkin's technique and Parseval's theorem. Then the characteristic equation yields the eigenvalues as the propagation constants of different modes, with which other transmission line properties like characteristic impedance and field distribution can be computed. Itoh and Menzel [27] pointed out the connection between the Green's functions in the spatial and spectral domains. Livernois and Katehi [28] applied the principle of scattering superposition to find the spatial domain Green's functions and to analyze multilayered structures. In [29], closed-form spatial Green's functions for thick microstrip substrate were derived using the complex image technique.

The differential-equation-based methods directly discretize the entire simulation domain to result in a huge linear system of equations. Although being flexible to handle inhomogeneous problems, they prefer truncated problem domains rather than open ones. Examples of these approaches are the FD [30], [31], the finite difference in time domain (FDTD), the FEM [32]-[35], the method of lines (MoL) [36], and the transmission line matrix (TLM) method [37]. Zhao *et al.* [38] proposed a full-wave compact 2-dimensional finite difference frequency-domain method for general guided transmission lines. Shibata and Sano [39] used the FDTD method to study the MIS structure with the metallization effect. Yook *et al.* [40] considered and analyzed the 3-dimensional interconnect with through-substrate vertical vias using the FDTD and FEM, respectively. Rather than the Fourier transform in the SDA, the MoL uses the finite difference along the lateral direction and solves for analytical solutions along the vertical direction. The TLM requires the 3-dimensional grid partitioning. Neighboring grid points are connected by distributed transmission lines that model the wave phenomena inside the structure. The local transmission line parameters are obtained by the media and boundary conditions.

Another full-wave approach is the mode-matching method that is useful when the whole

problem region can be partitioned and each sub-region has well-defined solutions that satisfy the BCs. The orthogonality of solutions is applied to generate a linear system of equations [41], [42]. The details of other numerical methods can be found in [43].

Besides the study of general multilayered transmission lines, the characteristics of microstrip-type and coplanar waveguide-type interconnects over lossy semiconductor substrate have also been studied extensively. Many accurate electromagnetic models have been built to predict these frequency-dependent properties. Early research work on guided-wave structures formed by metallic strips on semiconductor wafers can be traced back to the 1960s. Guckel *et al.* [44] suggested that the very low phase-velocity wave could exist within MIS structures. In 1971, Hasegawa *et al.* [45] experimentally verified Guckel's prediction and further proposed three fundamental modes. In both papers, the transmission line model with lumped elements were derived. Jäger [46] investigated the slow-wave propagation and the effect of metallic losses. Kennis and Faucon [47] used the SDA to verify the numerical results with the measurement. A similar full-wave approach was applied by Cano *et al.* [48] to the microstrip lines with anisotropic substrates. The close-form expressions for the extracted RLCG parameters for MIS lines were proposed by Williams [49]. A fast EM integral equation method was implemented by Morsey *et al.* [50] for the frequency domain modeling of lossy interconnect. Plaza *et al.* [51] presented a quasi-transverse magnetic (TM) MoL to the lossy transmission lines. All these efforts took into account the conductor loss of transmission lines and hybrid nature of the fundamental modes in layered structures.

One shortcoming of the canonical SDA is its inability to model thick conductors like the finite metallization of signal strips. To analyze the transmission line loss, several improved and modified SDA models have been proposed. For example, Das and Pozar [52], [53] used the SDA to develop the general Green's functions and analyze the conductor, dielectric, and radiation loss for multilayered transmission lines.

1.3 Organization of the Dissertation

The rest of the dissertation is organized as follows. Chapter 2 investigates the parallel-plate waveguide model to study the metal-insulator-metal-semiconductor (MIMS) structure. The exact eigenvalue equation is derived to solve for the fundamental TM modes. Furthermore, the integral-based formulations of field distribution and characteristic impedance are presented. Based on the eigenvalue equation, the first- and second-order low-frequency approximations are derived for the propagation modes and equivalent circuit models.

Chapter 3 briefly reviews the electromagnetic background of the full-wave SDA. The Green's functions for 2-dimensional multilayered transmission lines are derived using the transfer matrix method [22] and the immitance approach [23]. A new formulation of transfer matrices is developed to avoid the potential overflow in [22]. Resulting integral equations are solved by the Galerkin's method. The propagation constants are found by the complex-root-finding algorithm as the eigenvalues of transmission line systems.

Chapter 4 discusses separately the modeling of thin metal ground layers and signal strips. Different approximation models in the literature are listed and compared through the numerical simulation. The modified SDA is used to study the influence of imperfect conductors with finite thickness.

In Chapter 5, a complete picture of transmission line properties is presented. This chapter embodies in detail the formulations and expressions that are useful for analyzing the loss, characteristic impedance, field distribution, and transient response of transmission lines. Some computational topics such as complex-root finding and numerical integration are discussed.

The overall analysis of transmission lines is implemented with examples of MIMS and metal-insulator-metal-insulator (MIMI) structures in Chapter 6. The full-wave numerical simulations are utilized to study the slow-wave effect and the influence of finite metallization thickness and conductivity. Conclusions and future work are discussed in Chapter 7.

There are three appendices in the dissertation. Appendix A is devoted to the formulation of the parallel-plate waveguide model. Appendix B contains the details of the transfer matrices under different BCs. Appendix C lists all the abbreviations used in this dissertation.

CHAPTER 2.   THE PARALLEL-PLATE WAVEGUIDE MODEL FOR LOSSY TRANSMISSION LINES

2.1   Introduction

Among the diverse models for multilayered microstrip lines, the parallel-plate waveguide model is the simplest one to study the wave propagation phenomenon in inhomogeneous medias. Its basic assumption is that, when the width-to-height (w/h) ratio is large enough, microstrip lines can be approximated by the parallel-plate waveguides. All planar structures, even including ground planes and signal strips, are modeled as uniform dielectric sheets. The field distribution becomes uniform and no radiation exists along the lateral directions, which also implies that the fringing fields are ignored. To ensure propagation modes along the longitudinal direction, the transverse resonance condition must be satisfied. This condition greatly simplifies the complicated 2-dimensional eigenvalue problems into 1-dimensional ones. Thus it is easy to gain a good physical insight into the propagation mechanism. Different propagation modes were found using this model. And equivalent transmission-line circuits were built accordingly.

Unlike the homogeneous parallel-plate waveguide that supports pure TEM waves, the multilayered one only supports hybrid transverse electric (TE) and transverse magnetic (TM) waves because of the coupling between electric and magnetic fields on the dielectric interfaces. The dominant propagation mode is the TM_0 or E mode. Only at low frequencies, when the longitudinal field components are negligible, can the quasi-TEM mode approximation be applied.

The original work of the parallel-plate waveguide can be traced back to J. C. Maxwell who studied the interfacial and space-charge polarization for the Maxwell-Wagner two-layer con-

denser [54]. The condenser consists of two parallel sheets of dielectric materials and is bounded by perfect conductor plates. In the proposed equivalent circuit, each layer was modeled by a shunt capacitor and a shunt resister, and all layers were in series relationship.

Guckel *et al.* [44], Hasegawa *et al.* [45], and Jäger [46] did the initial work to study the MIS transmission lines using the parallel-plate waveguide models. Guckel *et al.* found a critical conductivity $\sigma_{\min}$ where the line attenuation is a minimum. When the semiconductor conductivity $\sigma_s > \sigma_{\min}$, the structure is controlled by the series loss from the semiconductor substrate, and by the shunt loss vice versa. Three frequency intervals were found: the diffusion-like propagation at low frequencies, the very-low-phase-velocity region, and the skin-effect and dielectric loss behavior in higher frequencies. The low-frequency and second-order approximations of the propagation constant were derived along with different equivalent circuit models. Hasegawa *et al.* extended the concept of the operation regions and defined three fundamental "modes": the dielectric quasi-TEM mode, the skin-effect mode, and the slow-wave mode. Between them are the transition regions. Equivalent circuits for different modes were proposed accordingly. Jäger studied the slow-wave propagation of Schottky-contact microstrip lines. Unlike the PEC boundary conditions used by previous researchers, the metallic strip conductor as well as the ground plane were modeled as ohmic metallization layers, and the perfect magnetic conductor (PMC) BCs were used to derive the formulas for impedance and propagation constant. In the equivalent circuit, the resistance from longitudinal losses in substrate was modeled as in parallel, instead of in series, with the resistance of metallic conductors. The influence of the imperfect conductors was found to be dominant. More recently, based on the volume integral, Williams [49] developed the close-form expressions for the RLCG parameters of equivalent circuits. All these investigations build the foundation of semiconductor-based lossy transmission lines.

The chapter is organized as follows. In Section 2.2, a MIMS structure is studied using the exact eigenvalue equations. Section 2.3 derives corresponding low-frequency approximations and proposes the equivalent circuits. Numerical simulations are exhibited in Section 2.4, and the limitations of the parallel-plate waveguide model are discussed in Section 2.5.

2.2 The Metal-Insulator-Metal-Semiconductor Structure With a Thin Metal Layer

To study the effect of the thin metallization layer, a MIMS structure is studied using the parallel-plate waveguide model. Fig. 2.1 includes two model structures, where Fig. 2.1(a) shows a three-layered parallel-plate waveguide model with PEC-PEC BCs and Fig. 2.1(b) shows a four-layered model with PEC-PMC BCs.[1] The four-layered structure is much closer to the open microstrip case with thin metallization ground and signal strip. All parallel-plate structures are infinite in the x and z directions. The gray layer stands for the silicon substrate; the white layer stands for the silicon dioxide. A thin metallization layer is inserted in the middle. In the figures, ε_{ri} and μ_{ri} stand for the relative permittivity and relative permeability of ith layer. l_i and σ_i are the thickness and conductivity, respectively. In this case, the conductivity of silicon dioxide σ_3 is assumed to be zero. As the models in [49], the thin metal layer is regarded as a dielectric with a complex relative permittivity defined as

$$\dot{\varepsilon}_{ri} = \varepsilon'_{ri} - j\varepsilon''_{ri} = \varepsilon_{ri} - j\sigma_i/(\omega\varepsilon_0) \tag{2.1}$$

where σ_i is the metal conductivity and ω is the angular frequency.
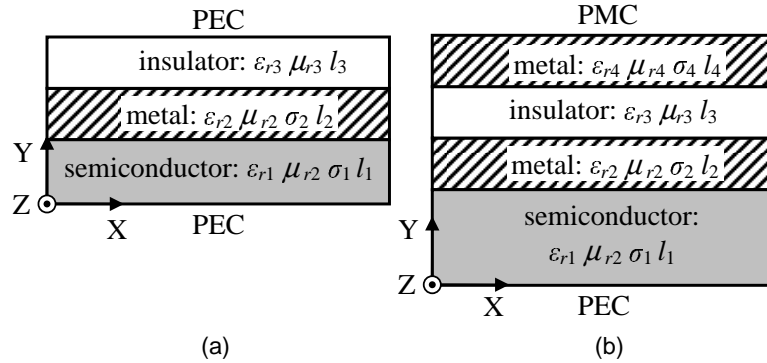
Figure 2.1: Two parallel-plate waveguide models for a MIMS structure: (a) three-layered model with PEC-PEC BCs, (b) four-layered model with PEC-PMC BCs.

In the z direction, this guided-wave structure is assumed to have a longitudinal propagation constant γ_z, and the propagation wave owns $e^{+j\omega t}e^{-j\gamma_z z}$ as the factor.[2] Instantly, we get the

---

[1] The PMC is an approximation for the open space BC.

[2] Compared with γ defined in [44], [46], the relation $j\gamma_z = \gamma$ holds.

relationship as follows

$$\gamma_i^2 - \gamma_z^2 = -k_0^2 \dot\varepsilon_{ri} \mu_{ri}, \ i = 1, \ldots, N \tag{2.2}$$

where N is the number of layers; $k_0^2 = \omega^2 \varepsilon_0 \mu_0$ is the free-space wave number; i is the layer index. Unlike otherwise specified, γ_i here is actually the simple showing of γ_{yi}, the transverse propagation constant along the y direction as $e^{-\gamma_i y}$. In such structure, the fundamental propagation mode is the TM or the E mode. According to the transverse resonance condition, the up and down impedances are matched on the interface as [46], [55]

$$\sum_{i=1}^{C_1^N} Z_i t_i + \sum_{\substack{(i,j,k) \\ i<j<k}}^{C_3^N} \frac{Z_i Z_k}{Z_j} t_i t_j t_k + \sum_{\substack{(i,j,k,l,m) \\ i<j<k<l<m}}^{C_5^N} \frac{Z_i Z_k Z_m}{Z_j Z_l} t_i t_j t_k t_l t_m + \cdots$$
$$+ \sum_{\substack{(i,j,k,\ldots,n_p) \\ i<j<k<\cdots<n_p}}^{C_p^N} \frac{Z_i Z_k \cdots Z_{n_p}}{Z_j Z_l \cdots Z_{n_{p-1}}} t_i t_j t_k \cdots t_{n_p} = 0 \tag{2.3}$$

where p is the maximum odd number that does not exceed N. The last summation is denoted over all the arrangement $(i, j, k, \cdots, n_p)$ in which p integers are chosen out of $1, 2, \cdots, N$ and arranged in the order of increasing magnitude. C_p^N is the number of combinations of p objects from N

$$C_p^N \equiv \binom{N}{p} \equiv \frac{N!}{p!(N-p)!}. \tag{2.4}$$

t_i is defined as follows

$$t_i = \begin{cases} \tanh{(\gamma_i l_i)} & (i = 2, \cdots, N-1) \\ \tanh{(\gamma_i l_i)} & (i = 1, N, \text{ PEC}) \\ \coth{(\gamma_i l_i)} & (i = 1, N, \text{ PMC}) \end{cases} . \tag{2.5}$$

Z_i denotes the characteristic field impedance as

$$Z_i = \frac{\gamma_i}{j\omega\varepsilon_0\dot\varepsilon_{ri}} \ (\text{TM modes}) \tag{2.6}$$

$$Z_i = \frac{j\omega\mu_0\mu_{ri}}{\gamma_i} \ (\text{TE modes}). \tag{2.7}$$

At certain frequency, the unknown propagation constant γ_z can be solved from the characteristic equations (2.3).

2.3   The Low-Frequency Approximations and Equivalent Circuit Models

Follow the same procedures in [44], [46], the low-frequency approximate solutions of γ_z are deduced for the specific three-layered MIMS structure in Fig. 2.1(a). First, three separate conditions are formulated from equation (2.2) as follows

$$\gamma_i^2 - \gamma_z^2 \;=\; -k_0^2 \dot{\varepsilon}_{ri}\mu_{ri}, \quad i = 1, 2, 3. \tag{2.8}$$

The impedances are matched on the interfaces to satisfy the transverse resonant condition to yield the simplified condition as

$$\sum_{i=1}^{3} \frac{\gamma_i}{\dot{\varepsilon}_{ri}} \tanh\left(\gamma_i l_i\right) + \frac{\gamma_1 \gamma_3 \dot{\varepsilon}_{r2}}{\gamma_2 \dot{\varepsilon}_{r1} \dot{\varepsilon}_{r3}} \tanh(\gamma_1 l_1) \tanh(\gamma_2 l_2) \tanh(\gamma_3 l_3) = 0. \tag{2.9}$$

By timing $\tanh\left(\gamma_i l_i\right)/\left(\gamma_i \varepsilon_{ri}\right)$ to both sides of (2.8) and summing them from $i = 1$ to 3, the eigenvalue equation (2.9) may be expressed as

$$\gamma_z^2 = \frac{k_0^2 \sum_{i=1}^{3} \frac{\mu_{ri}}{\gamma_i} \tanh\left(\gamma_i l_i\right) - \frac{\gamma_1 \gamma_3 \dot{\varepsilon}_{r2}}{\gamma_2 \dot{\varepsilon}_{r1} \dot{\varepsilon}_{r3}} \tanh\left(\gamma_1 l_1\right) \tanh\left(\gamma_2 l_2\right) \tanh\left(\gamma_3 l_3\right)}{\sum_{i=1}^{3} \frac{1}{\gamma_i \dot{\varepsilon}_{ri}} \tanh\left(\gamma_i l_i\right)} \tag{2.10}$$

The conductivity of the silicon dioxide layer is normally zero ($\sigma_3 = 0$). At low frequencies, the propagation mode is close to the quasi-TEM wave where γ_z tends to be negligible. In this section, two cases will be discussed: the low-resistance silicon substrate and the high-resistance silicon substrate. For the low-resistance silicon substrate, the propagation constants in metallization layer and lossy silicon substrate have the following approximations

$$\begin{aligned}
\gamma_1^2 &\approx -\omega^2 \varepsilon_0 \mu_0 \mu_{r1} \left(\varepsilon_{r1} + \frac{\sigma_1}{j\omega\varepsilon_0}\right) \approx j\omega\mu_0 \mu_{r1}\sigma_1 \\
\gamma_2^2 &\approx -\omega^2 \varepsilon_0 \mu_0 \mu_{r2} \left(\varepsilon_{r2} + \frac{\sigma_2}{j\omega\varepsilon_0}\right) \approx j\omega\mu_0 \mu_{r2}\sigma_2 \\
\gamma_3^2 &\approx \omega^2 \varepsilon_0 \mu_0 \varepsilon_{r3}\mu_{r3}
\end{aligned} \tag{2.11}$$

when

$$\omega << \min\left\{\frac{2}{\mu_0\sigma_1 l_1^2}, \frac{2}{\mu_0\sigma_2 l_2^2}\right\} \text{ and } \omega << \min\left\{\frac{\sigma_1}{\varepsilon_{r0}\varepsilon_{r1}}, \frac{\sigma_2}{\varepsilon_{r0}\varepsilon_{r2}}\right\}. \tag{2.12}$$

14

Thus, for the low-frequency approximation, the following qualities hold

$$
\begin{aligned}
\gamma_1 &\propto \sqrt{\omega}, \ \dot{\varepsilon}_{r1} \approx \frac{\sigma_1}{j\omega\varepsilon_0} \\
\gamma_2 &\propto \sqrt{\omega}, \ \dot{\varepsilon}_{r2} \approx \frac{\sigma_2}{j\omega\varepsilon_0} \\
\gamma_3 &\propto \omega.
\end{aligned}
\tag{2.13}
$$

On the contrary, for the case of high-resistance silicon substrate, the silicon substrate tends to be a lossless dielectric that has $\sigma_1 = 0$. The corresponding low-frequency approximations become

$$
\begin{aligned}
\gamma_1 &\propto \omega \\
\gamma_2 &\propto \sqrt{\omega}, \ \dot{\varepsilon}_{r2} \approx \frac{\sigma_2}{j\omega\varepsilon_0} \\
\gamma_3 &\propto \omega.
\end{aligned}
\tag{2.14}
$$

In addition, for the typical manufactured silicon wafers, $l_1 >> l_2, l_3$ and l_2 could be rather small if the thin metallization layer is fabricated.

Based on the pervious assumptions, when the frequency ω approaches to zero, above propagation constant γ_z has the first-order and second-order approximations, which will be discussed below.

2.3.1 First-Order Approximation

At low frequencies, the small argument approximation as $\tanh(\gamma_i l_i) \approx \gamma_i l_i$ $(i = 1, 2, 3)$ reduces (2.10), by ignoring the high-order terms, to

$$
\gamma_z^2 \approx \frac{k_0^2 \left(\mu_{r1}l_1 + \mu_{r2}l_2 + \mu_{r3}l_3\right) - \frac{\dot{\varepsilon}_{r2}}{\dot{\varepsilon}_{r1}\dot{\varepsilon}_{r3}}\gamma_1^2\gamma_3^2 l_1 l_2 l_3}{\frac{l_1}{\dot{\varepsilon}_{r1}} + \frac{l_2}{\dot{\varepsilon}_{r2}} + \frac{l_3}{\dot{\varepsilon}_{r3}}}.
\tag{2.15}
$$

Using the conditions of (2.11) and (2.12) for the low-resistance silicon case, above equation is changed into

$$
\begin{aligned}
\gamma_z^2 &\approx \frac{\omega^2\mu_0\varepsilon_0\left(\mu_{r1}l_1 + \mu_{r2}l_2 + \mu_{r3}l_3\right) - j\omega^3\mu_0^2\varepsilon_0\mu_{r1}\mu_{r3}\sigma_2 l_1 l_2 l_3}{\frac{j\omega\varepsilon_0 l_1}{\sigma_1} + \frac{j\omega\varepsilon_0 l_2}{\sigma_2} + \frac{l_3}{\varepsilon_{r3}}} \\
&\approx \frac{-j\omega\mu_0\left(\mu_{r1}l_1 + \mu_{r2}l_2 + \mu_{r3}l_3\right)}{\frac{l_1}{\sigma_1} + \frac{l_2}{\sigma_2} + \frac{l_3}{j\omega\varepsilon_0\varepsilon_{r3}}}.
\end{aligned}
\tag{2.16}
$$

In this equation, only the ω^2, ω, and constant terms are reserved, whereas the high-order terms such as ω^3 are ignored. The first-order approximation corresponds to an equivalent distributed circuit with a series impedance per unit length and a shunt admittance per unite length. The series impedance comes from three inductors in series, whereas the shunt admittance comes from one capacitor and two conductors that are connected in series relationship as shown in Fig. 2.2(a).

For the high-resistance silicon substrate case, the similar approximation becomes

$$\gamma_z^2 = \frac{-j\omega\mu_0\left(\mu_{r1}l_1 + \mu_{r2}l_2 + \mu_{r3}l_3\right)}{\frac{l_1}{j\omega\varepsilon_0\varepsilon_{r1}} + \frac{l_2}{\sigma_2} + \frac{l_3}{j\omega\varepsilon_0\varepsilon_{r3}}} \tag{2.17}$$

where the denominator shows the equivalent shunt elements in the distributed circuit are two capacitors and one conductor in series. The equivalent circuit and corresponding component parameters are shown in Fig. 2.2(b).

Specifically, if all three layers are lossless ($\sigma_1 = \sigma_2 = \sigma_3 = 0$), the low-frequency approximation is

$$\gamma_z^2 = \frac{k_0^2\left(\mu_{r1}l_1 + \mu_{r2}l_2 + \mu_{r3}l_3\right)}{\frac{l_1}{\varepsilon_{r1}} + \frac{l_2}{\varepsilon_{r2}} + \frac{l_3}{\varepsilon_{r3}}} \tag{2.18}$$

which directly relates to an equivalent circuit with three series inductors for the series impedance and three series capacitors for the shunt admittance.
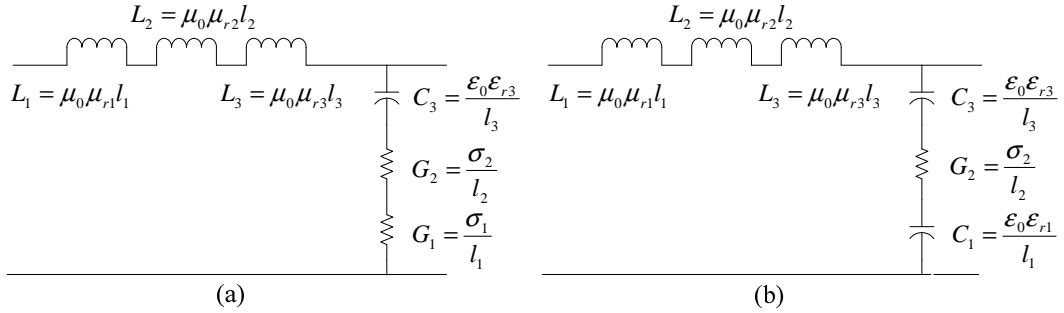
Figure 2.2: Equivalent circuits for the first-order approximation: (a) low-resistance substrate, (b) high-resistance substrate.

2.3.2 Second-Order Approximation

By using the two-term approximation as $\tanh(\gamma_i l_i) \approx \gamma_i l_i - \frac{1}{3}\left(\gamma_i l_i\right)^3$ ($i = 1, 2, 3$), the previous eigenvalue equation (2.10) can be approximated according to different conditions of the

silicon substrate.

2.3.2.1 Low-resistance silicon substrate

In this case, the silicon substrate ($i = 1$) has a large conductivity ($\sigma_1 >> \omega\varepsilon_0\varepsilon_{r1}$) as (2.12) so that $\gamma_1 \propto \sqrt{\omega}$, $\gamma_2 \propto \sqrt{\omega}$, and $\gamma_3 \propto \omega$. The characteristic equation becomes

$$
\begin{aligned}
\gamma_z^2 \approx \Bigg[& k_0^2 \left(\mu_{r1} l_1 + \mu_{r2} l_2 + \mu_{r3} l_3 \right) - k_0^2 \left(\mu_{r1} \gamma_1^2 l_1^3 + \mu_{r2} \gamma_2^2 l_2^3 + \mu_{r3} \gamma_3^2 l_3^3 \right) /3 \\
& - \frac{\dot{\varepsilon}_{r2}\gamma_1\gamma_3}{\dot{\varepsilon}_{r1}\dot{\varepsilon}_{r3}\gamma_2} \left(\gamma_1 l_1 - \frac{1}{3}\gamma_1^3 l_1^3 \right) \left(\gamma_2 l_2 - \frac{1}{3}\gamma_2^3 l_2^3 \right) \left(\gamma_3 l_3 - \frac{1}{3}\gamma_3^3 l_3^3 \right) \Bigg] \\
& \Bigg/ \left[\frac{l_1}{\dot{\varepsilon}_{r1}} + \frac{l_2}{\dot{\varepsilon}_{r2}} + \frac{l_3}{\dot{\varepsilon}_{r3}} - \frac{1}{3} \left(\frac{\gamma_1^2 l_1^3}{\dot{\varepsilon}_{r1}} + \frac{\gamma_2^2 l_2^3}{\dot{\varepsilon}_{r2}} + \frac{\gamma_3^2 l_3^3}{\dot{\varepsilon}_{r3}} \right) \right].
\end{aligned} \tag{2.19}
$$

The first term in the numerator is proportional to ω^2. The second term is truncated as

$$
-\frac{k_0^2}{3} \left(\mu_{r1} \gamma_1^2 l_1^3 + \mu_{r2} \gamma_2^2 l_2^3 + \mu_{r3} \gamma_3^2 l_3^3 \right) \approx -\frac{k_0^2}{3} \left(\mu_{r1} \gamma_1^2 l_1^3 + \mu_{r2} \gamma_2^2 l_2^3 \right) \tag{2.20}
$$

where the ω^4 term is neglected. In the same way, the third term in the numerator becomes

$$
\frac{\dot{\varepsilon}_{r2}\gamma_1\gamma_3}{\dot{\varepsilon}_{r1}\dot{\varepsilon}_{r3}\gamma_2} \left(\gamma_1 l_1 - \frac{1}{3}\gamma_1^3 l_1^3 \right) \left(\gamma_2 l_2 - \frac{1}{3}\gamma_2^3 l_2^3 \right) \left(\gamma_3 l_3 - \frac{1}{3}\gamma_3^3 l_3^3 \right) \approx \frac{\dot{\varepsilon}_{r2}}{\dot{\varepsilon}_{r1}\dot{\varepsilon}_{r3}}\gamma_1^2\gamma_3^2 l_1 l_2 l_3 \tag{2.21}
$$

where $\frac{\dot{\varepsilon}_{r2}}{\dot{\varepsilon}_{r1}\dot{\varepsilon}_{r3}} \approx \frac{\sigma_2}{\sigma_1\varepsilon_{r3}}$ is a constant. So only the ω^3 terms are kept in the numerator. Similarly, all the terms are kept in the denominator because its highest order terms are only of ω^2. By neglecting the high-order terms of ω, the characteristic equation (2.19) has the second-order approximate solution as

$$
\begin{aligned}
\gamma_z^2 \approx & \left[k_0^2(\mu_{r1} l_1 + \mu_{r2} l_2 + \mu_{r3} l_3) - \frac{k_0^2}{3} \left(\mu_{r1} \gamma_1^2 l_1^3 + \mu_{r2} \gamma_2^2 l_2^3 \right) - \frac{\dot{\varepsilon}_{r2}}{\dot{\varepsilon}_{r1}\dot{\varepsilon}_{r3}}\gamma_1^2\gamma_3^2 l_1 l_2 l_3 \right] \\
& \Bigg/ \left[\frac{l_1}{\dot{\varepsilon}_{r1}} + \frac{l_2}{\dot{\varepsilon}_{r2}} + \frac{l_3}{\dot{\varepsilon}_{r3}} - \frac{1}{3} \left(\frac{\gamma_1^2 l_1^3}{\dot{\varepsilon}_{r1}} + \frac{\gamma_2^2 l_2^3}{\dot{\varepsilon}_{r2}} + \frac{\gamma_3^2 l_3^3}{\dot{\varepsilon}_{r3}} \right) \right].
\end{aligned} \tag{2.22}
$$

Substituted by (2.8), above characteristic equation can be rewritten as a quadric equation of γ_z^2

$$
A\gamma_z^4 - B\gamma_z^2 + C = 0 \tag{2.23}
$$

where

$$A = \frac{1}{3}\left(\frac{l_1^3}{\dot{\varepsilon}_{r1}} + \frac{l_2^3}{\dot{\varepsilon}_{r2}} + \frac{l_3^3}{\dot{\varepsilon}_{r3}}\right) - \frac{\dot{\varepsilon}_{r2}}{\dot{\varepsilon}_{r1}\dot{\varepsilon}_{r3}}l_1l_2l_3 \tag{2.24}$$

$$B = \sum_{i=1}^{3}\frac{l_i}{\dot{\varepsilon}_{ri}} + \frac{k_0^2}{3}(2\mu_{r1}l_1^3 + 2\mu_{r2}l_2^3 + \mu_{r3}l_3^3) - \frac{\dot{\varepsilon}_{r2}}{\dot{\varepsilon}_{r1}\dot{\varepsilon}_{r3}}k_0^2\left(\dot{\varepsilon}_{r1}\mu_{r1} + \dot{\varepsilon}_{r3}\mu_{r3}\right)l_1l_2l_3 \tag{2.25}$$

$$C = k_0^2\left(\mu_{r1}l_1 + \mu_{r2}l_2 + \mu_{r3}l_3\right) + \frac{k_0^4}{3}\left(\dot{\varepsilon}_{r1}\mu_{r1}^2l_1^3 + \dot{\varepsilon}_{r2}\mu_{r2}^2l_2^3 - 3\dot{\varepsilon}_{r2}\mu_{r1}\mu_{r3}l_1l_2l_3\right). \tag{2.26}$$

The basic solutions of the quadric characteristic equation (2.23) are found through

$$\gamma_z^2 = \frac{B}{2A}\left(1 \pm \sqrt{1 - \frac{4AC}{B^2}}\right). \tag{2.27}$$

With the consideration of fabrication specifics, above coefficients yield

$$A \approx -\frac{\sigma_2}{\sigma_1\varepsilon_2}l_1l_2l_3\left(1 - \frac{\sigma_1l_3^2}{3\sigma_2l_1l_2} - j\omega\frac{\varepsilon_0\varepsilon_{r3}l_1^2}{3\sigma_2l_2l_3}\right) \tag{2.28}$$

$$B \approx \frac{l_3}{\varepsilon_{r3}} + \frac{\omega^2\varepsilon_0\mu_0}{3}\left(2\mu_{r1}l_1^3 - \frac{3\sigma_2}{\sigma_1}\mu_{r3}l_1l_2l_3\right) + j\omega\left(\frac{\varepsilon_0l_1}{\sigma_1} + \frac{\varepsilon_0l_2}{\sigma_2} + \frac{\mu_0\mu_{r1}\sigma_2l_1l_2l_3}{\varepsilon_{r3}}\right) \tag{2.29}$$

$$C \approx \omega^2\varepsilon_0\mu_0\sum_{i=1}^{3}\mu_{ri}l_i - j\frac{\omega^3\varepsilon_0\mu_0^2}{3}\left(\sigma_1\mu_{r1}^2l_1^3 + \sigma_2\mu_{r2}^2l_2^3 - 3\sigma_2\mu_{r1}\mu_{r3}l_1l_2l_3\right) \tag{2.30}$$

if

$$l_1 >> l_3 >> l_2$$

$$\sigma_2 >> \sigma_1 \tag{2.31}$$

where l_1 is in the order of hundreds of microns; l_3 is about several microns. For the very thin metallization, l_2 is less than one micron. The silicon substrate has a conductivity σ_1 in the order of $10^1\,\text{S/m}$, while the conductivity σ_2 of metallization is in the order of $10^7\,\text{S/m}$. Thus, above conditions (2.31) hold.

From (2.28)-(2.30), it is apparent that $B^2 >> 4AC$ when ω approaches to zero. Thus, with this low-frequency assumption, we can choose the minimal solution as the desired propagation constant γ_z

$$\gamma_z^2 \approx \frac{B}{2A}\left[1 - \left(1 - \frac{2AC}{B^2}\right)\right] = \frac{C}{B}. \tag{2.32}$$

Then the low-frequency approximate solution may be written as

$$
\frac{\gamma_z^2}{k_0^2} \approx \frac{(\mu_{r1}l_1 + \mu_{r2}l_2 + \mu_{r3}l_3) - j\frac{\omega\mu_0}{3}\left(\sigma_1\mu_{r1}^2 l_1^3 + \sigma_2\mu_{r2}^2 l_2^3 - 3\sigma_2\mu_{r1}\mu_{r3}l_1l_2l_3\right)}{\frac{l_3}{\varepsilon_{r3}} + \frac{\omega^2\varepsilon_0\mu_0}{3}\left(2\mu_{r1}l_1^3 - \frac{3\sigma_2}{\sigma_1}\mu_{r3}l_1l_2l_3\right) + j\omega\left(\frac{\varepsilon_0 l_1}{\sigma_1} + \frac{\varepsilon_0 l_2}{\sigma_2} + \frac{\mu_0\mu_{r1}\sigma_1 l_1 l_2 l_3}{\varepsilon_{r3}}\right)}
$$

$$
\approx \frac{\varepsilon_{r3}}{l_3}\left(\sum_{i=1}^{3}\mu_{ri}l_i\right)\left[1 - j\omega\mu_0\mu_{r1}\sigma_2 l_1 l_2\left(1 - \frac{\mu_{r3}l_3 - \frac{\sigma_1\mu_{r1}l_1^2}{3\sigma_2 l_2} - \frac{\mu_{r2}^2 l_2^2}{3\mu_{r1}l_1}}{\mu_{r1}l_1 + \mu_{r2}l_2 + \mu_{r3}l_3}\right)\right] \quad (2.33)
$$

where the high-order terms like ω^2 are neglected. From this approximation, we can find that the attenuation is proportional to the square of frequency. No local minima for the attenuation exist with respect to the conductivity and thickness parameters: σ_1, σ_2, l_1, and l_2. Thus, it is evident that the low-frequency critical $\sigma_{\min}$ in [44] and [46] cannot be applied to current MIMS parallel-plate waveguide structure. Fig. 2.3(a) shows the equivalent circuit model and circuit parameters. Compared with the first-order approximations, R_X, L_X, and G_X are attributed to the complicated EM couplings between layers.
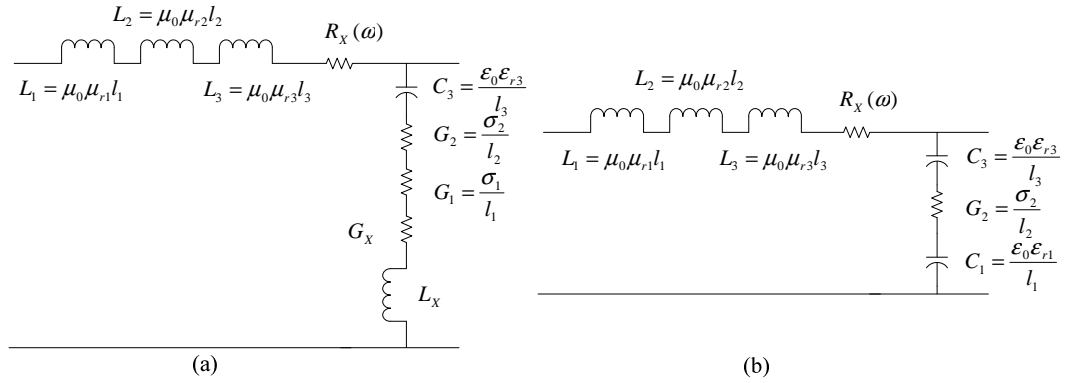
Figure 2.3: Equivalent circuits for the second-order approximation: (a) low-resistance substrate with $R_X = \omega^2\mu_0^2\left(\sigma_1\mu_{r1}^2 l_1^3 + \sigma_2\mu_{r2}^2 l_2^3 - 3\sigma_2\mu_{r1}\mu_{r3}l_1l_2l_3\right)/3$, $G_X = \varepsilon_0\varepsilon_{r3}/\left(\mu_0\mu_{r1}\sigma_2 l_1 l_2 l_3\right)$, and $L_X = \mu_0\left(\frac{3\sigma_2}{\sigma_1}\mu_{r3}l_1l_2l_3 - 2\mu_{r1}l_1^3\right)/3$, (b) high-resistance substrate with $R_X = \sigma_2\omega^2\mu_0^2\mu_{r2}^2 l_2^3/3$.

2.3.2.2   High-resistance silicon substrate

In this case, the silicon substrate has a small conductivity σ_1 ($\sigma_1 \ll \omega\varepsilon_0\varepsilon_{r1}$) or a loss tangent so that $\gamma_1 \propto \omega$, $\gamma_2 \propto \sqrt{\omega}$, and $\gamma_3 \propto \omega$. Following the same process as previous section, the second-order approximation becomes

$$
\gamma_z^2 \approx \frac{k_0^2(\mu_{r1}l_1 + \mu_{r2}l_2 + \mu_{r3}l_3) - \frac{k_0^2}{3}\mu_{r2}\gamma_{r2}^2 l_2^3}{\frac{l_1}{\dot{\varepsilon}_{r1}} + \frac{l_2}{\dot{\varepsilon}_{r2}} + \frac{l_3}{\dot{\varepsilon}_{r3}} - \frac{1}{3}\left(\frac{\gamma_1^2 l_1^3}{\dot{\varepsilon}_{r1}} + \frac{\gamma_2^2 l_2^3}{\dot{\varepsilon}_{r2}} + \frac{\gamma_3^2 l_3^3}{\dot{\varepsilon}_{r3}}\right)}. \quad (2.34)
$$

Corresponding A, B, and C coefficients are

$$A = \frac{1}{3}\left(\frac{l_1^3}{\dot{\varepsilon}_{r1}} + \frac{l_2^3}{\dot{\varepsilon}_{r2}} + \frac{l_3^3}{\dot{\varepsilon}_{r3}}\right) \tag{2.35}$$

$$B = \frac{l_1}{\dot{\varepsilon}_{r1}} + \frac{l_2}{\dot{\varepsilon}_{r2}} + \frac{l_3}{\dot{\varepsilon}_{r3}} + \frac{k_0^2}{3}(\mu_{r1}l_1^3 + 2\mu_{r2}l_2^3 + \mu_{r3}l_3^3) \tag{2.36}$$

$$C = k_0^2(\mu_{r1}l_1 + \mu_{r2}l_2 + \mu_{r3}l_3) + \frac{k_0^4}{3}\dot{\varepsilon}_{r2}\mu_{r2}^2l_2^3. \tag{2.37}$$

The approximation of γ_z yields the formulation as

$$\begin{aligned}
\frac{\gamma_z^2}{k_0^2} &\approx \frac{(\mu_{r1}l_1 + \mu_{r2}l_2 + \mu_{r3}l_3) - j\omega\frac{\mu_0\sigma_2\mu_{r2}^2l_2^3}{3}}{\frac{l_1}{\varepsilon_{r1}} + \frac{l_3}{\varepsilon_{r3}} + j\omega\frac{\varepsilon_0 l_2}{\sigma_2}} \\
&\approx (\mu_{r1}l_1 + \mu_{r2}l_2 + \mu_{r3}l_3)\left(\frac{l_1}{\varepsilon_{r1}} + \frac{l_3}{\varepsilon_{r3}}\right)^{-1} \\
&\quad \left\{1 - j\omega l_2\left[\frac{\mu_0\sigma_2\mu_{r2}^2l_2^2}{3(\mu_{r1}l_1 + \mu_{r2}l_2 + \mu_{r3}l_3)} + \frac{\varepsilon_0\varepsilon_{r1}\varepsilon_{r3}}{\sigma_2(\varepsilon_{r1}l_3 + \varepsilon_{r3}l_1)}\right]\right\}.
\end{aligned} \tag{2.38}$$

Similarly, the attenuation is proportional to the square of frequency and no critical $\sigma_{\min}$ exists in the low-frequency approximations. Fig. 2.3(b) shows the equivalent distributed circuit model. With γ_z founded, the effective permittivity $\varepsilon_{r\text{eff}}$ and attenuation α per unit length can be calculated as

$$\varepsilon_{r\text{eff}} = \left[\text{Re}\left(\frac{\gamma_z}{k_0}\right)\right]^2 \tag{2.39}$$

$$\alpha = -\text{Im}(\gamma_z). \tag{2.40}$$

2.4   Numerical Simulation of Metal-Insulator-Metal-Semiconductor Structures

The Newton's method is used to solve for the eigenvalue equations of layered MIMS structures in Fig. 2.1. The relevant result is called the exact solution of (2.9) to calibrate the first-order and second-order approximations in (2.16) and (2.32), respectively. Fig. 2.4 illustrates the results of the normalized wavelength λ_0/λ_g ($= \sqrt{\varepsilon_{r\text{eff}}}$) and attenuation constant α, where λ_g and λ_0 are denoted as the propagation wavelengths along the transmission line and in free space, respectively. The normalized wavelength is also the slowing factor of propagation
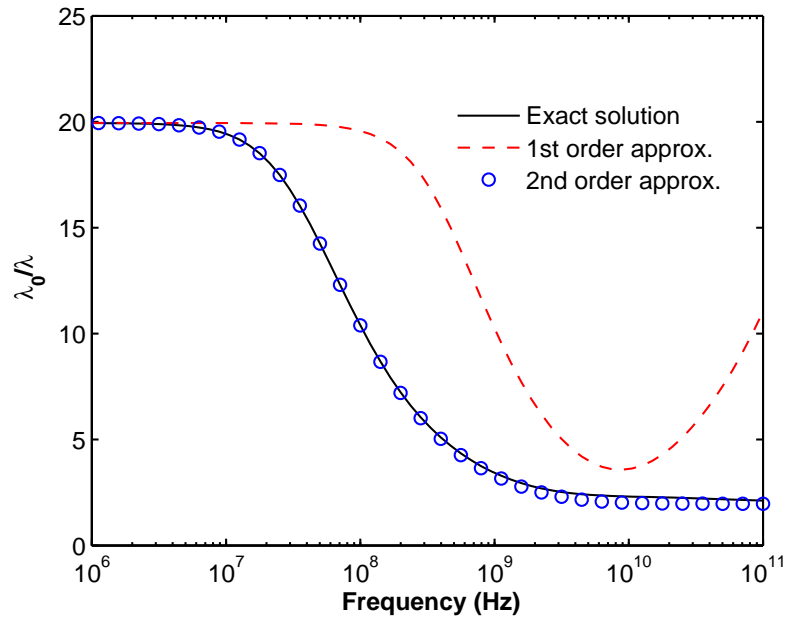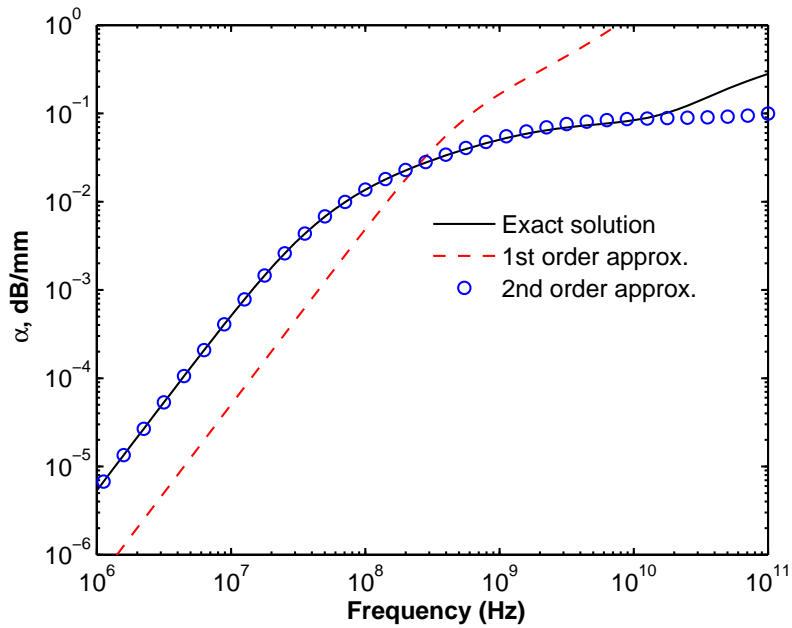
Figure 2.4: Exact and approximate solutions of propagation parameters for a 3-layered MIMS transmission line (PEC-PEC case) with semiconductor: $\varepsilon_{r1} = 11.7$, $\sigma_1 = 10\,\mathrm{S/m}$, $l_1 = 100\,\mu\mathrm{m}$, metallization: $\sigma_2 = 3 \times 10^7\,\mathrm{S/m}$, $l_2 = 1\,\mu\mathrm{m}$, insulator: $\varepsilon_{r3} = 3.9$, $l_3 = 1\,\mu\mathrm{m}$: (a) normalized wavelength, (b) attenuation per unit length.

velocity. As seen from Fig. 2.4, the first-order approximation only presents the acceptable normalized wavelength at very low frequency region, whereas an obvious deviation for the attenuation exists if compared with the exact solution. This shows that the first-order approximation is not appropriate to interpret the performance of lossy transmission lines, especially for the loss. One the contrary, the second-order approximation presents a good agreement with the exact solution up to about 10 GHz. Moreover, it is observed that the valid frequency range strongly depends on the conductivity σ_1 of semiconductor substrates. For instance, the upper valid boundary of the second-order approximation is reduced to about 1 GHz when $\sigma_1 = 1000\,\text{S/m}$.

Fig. 2.5 shows that the normalized wavelength and attenuation varying with the frequency and the metallization thicknesses l_2 for a MIMS shown in Fig. 2.1(a). Stepwise-convergence phenomena are observed. The curves that stand for very thin metallization converge to the zero-thickness limit, while thick metallization curves merge together when the frequency increases. Fig. 2.5 also shows clearly that the slope of attenuation at the low frequency region is the square of frequency, which is predicted by the imaginary part of the second-order approximation in (2.33). In this PEC-PEC model, it is shown that the transmission line parameters are influenced by the metallization thickness over a broad frequency range.

The influence of the signal strip is shown in Fig. 2.6. The PEC-PMC BCs are much closer to the reality of open microstrip lines than the PEC-PEC case [49]. The corresponding normalized wavelength and attenuation versus the frequency, metallization thicknesses l_2, and l_4 (l_2 and l_4 change simultaneously and own same values) are plotted. The results of PEC-PEC cases are also referenced for comparison. Unlike the PEC-PEC BCs that give bounded normalized wavelengths at low frequencies, the PEC-PMC BCs give large values of effective permittivity when the frequency decreases. This shows that the PMC BCs have more polarization effects and higher attenuation from the top metallization layer. In the PEC-PEC cases, the PEC shortens the top imperfect metallization and provides a perfect current return path, which actually diminishes the loss.

In Fig. 2.7, the equivalent transmission line circuit parameters (RLCG) of a 4-layered

MIMS line are extracted.[3] The signal strip thickness l_4 is fixed, while the metallization ground thickness l_2 changes. When $l_2 = 0$, the 4-layered MIMS structure is reduced to a MIS structure. The calculated RLCG results agree well with [49]. Fig. 2.7 shows that the thickness effects from the thin metal ground are evident. The extracted resistance and inductance are more sensitive to the influence of metallization thickness compared to the conductance and capacitance.

2.5   Discussion and Limitation

Although greatly simplifying the transmission line problem, the parallel-plate waveguide model has certain inevitable limitations. First, multilayered structures are assumed to have large width-to-height (w/h) ratios so that the fringing fields at edges are ignored. Thus, the parallel-plate waveguide model cannot describe the leakage waves that propagate along the lateral direction. This assumption also implies that spatial structure variations along the lateral directions are not allowed. Structures, such as the coplanar waveguides, corrugated ground planes, and inhomogeneous media with different depletion or doping regions, cannot be studied by this model. Second, the propagation modes in the parallel-plate waveguides are separated into independent TM and TE modes. But the real propagation modes for transmission lines are often hybrid ones. Third, the parallel-palate waveguide model and transmission line circuit model are accurate only at low frequencies. There is no a clear upper boundary of frequency to decide where the model becomes invalid. Normally the accuracy will lost when the frequency becomes higher than $10\,\mathrm{GHz}$.

All above aspects limit the application of the parallel-plate waveguide model and equivalent circuits to the real-world problems. But they are still good for presenting clear physical aspects for the guided-wave systems.

---

[3]The formulation for the characteristic impedance and RLCG parameters is presented in Appendix A.
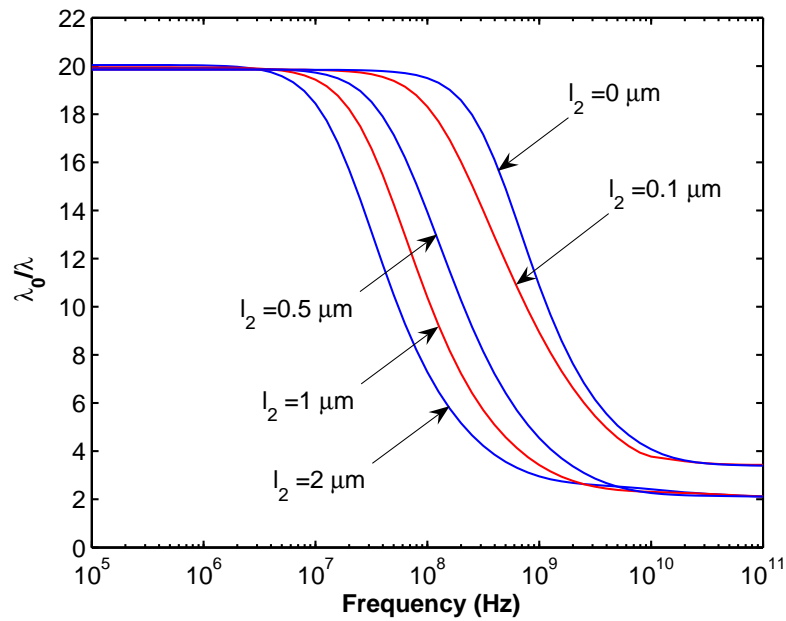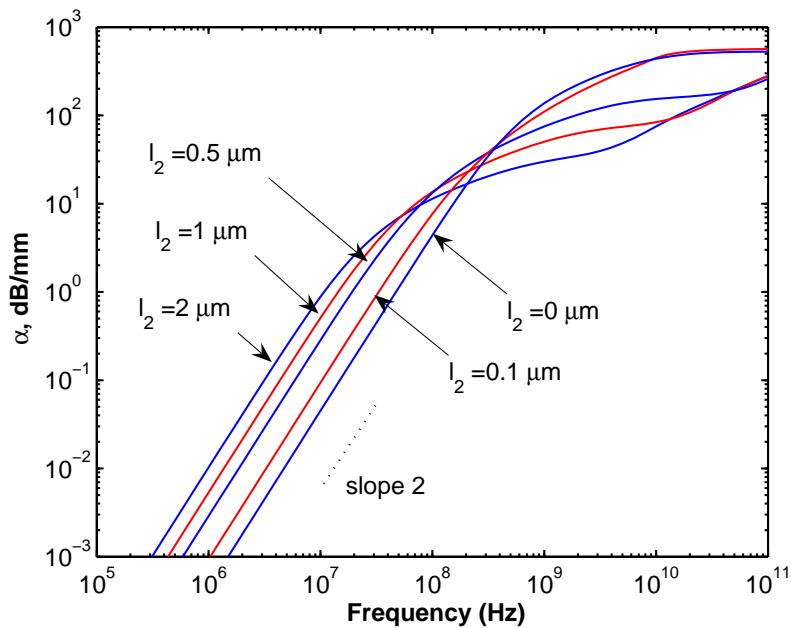
Figure 2.5: Frequency-dependent transmission line parameters versus thickness l_2 of a 3-layered MIMS transmission line (PEC-PEC case) with semiconductor: $\varepsilon_{r1} = 11.7$, $\sigma_1 = 10\,\mathrm{S/m}$, $l_1 = 100\,\mu\mathrm{m}$, metallization: $\sigma_2 = 3 \times 10^7\,\mathrm{S/m}$, insulator: $\varepsilon_{r3} = 3.9$, $l_3 = 1\,\mu\mathrm{m}$: (a) normalized wavelength, (b) attenuation per unit length.
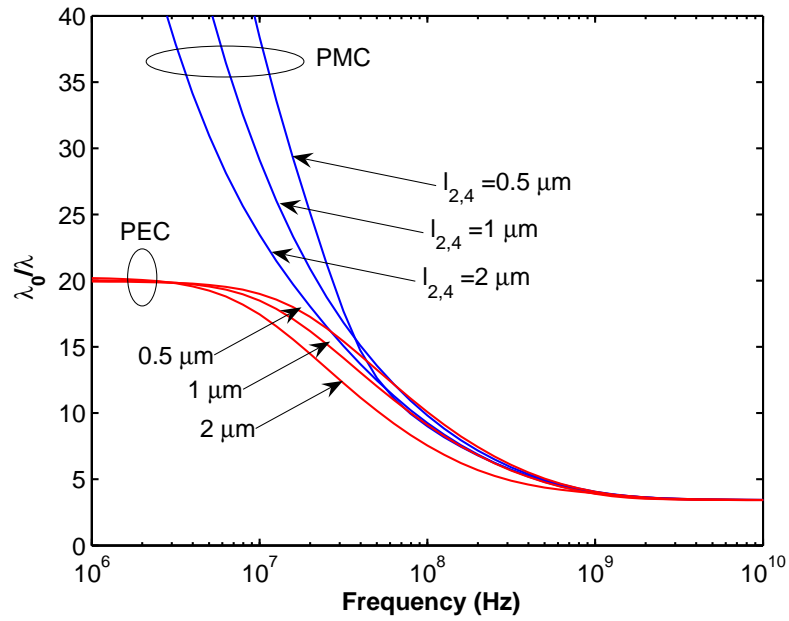
(a)
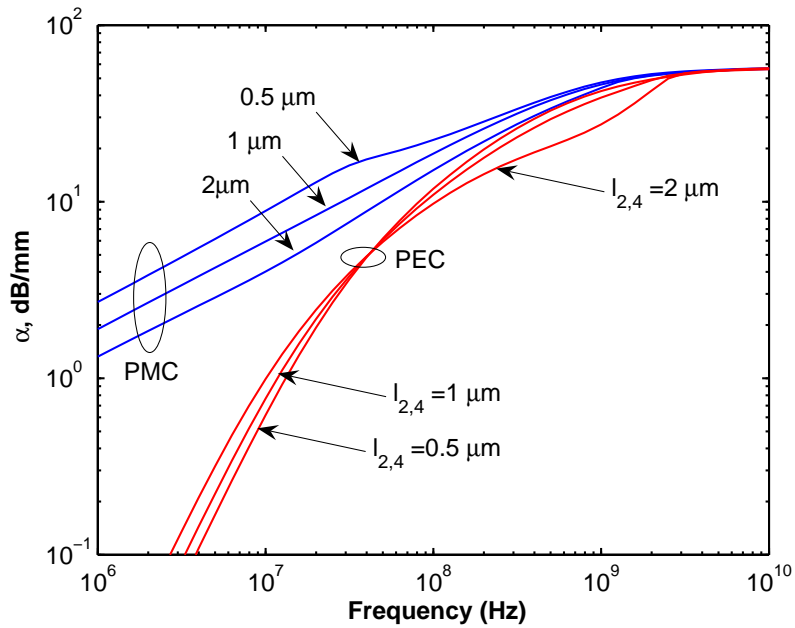
(b)

Figure 2.6: Frequency-dependent transmission line parameters versus thickness l_2 and l_4 of a 4-layered MIMS transmission line in Fig. 2.1(b), semiconductor: $\varepsilon_{r1} = 11.7$, $\sigma_1 = 1\,\mathrm{S/m}$, $l_1 = 100\,\mu\mathrm{m}$, insulator: $\varepsilon_{r3} = 3.9$, $l_3 = 1\,\mu\mathrm{m}$, metallization: $\sigma_2 = \sigma_4 = 3 \times 10^7\,\mathrm{S/m}$: (a) normalized wavelength, (b) attenuation per unit length.
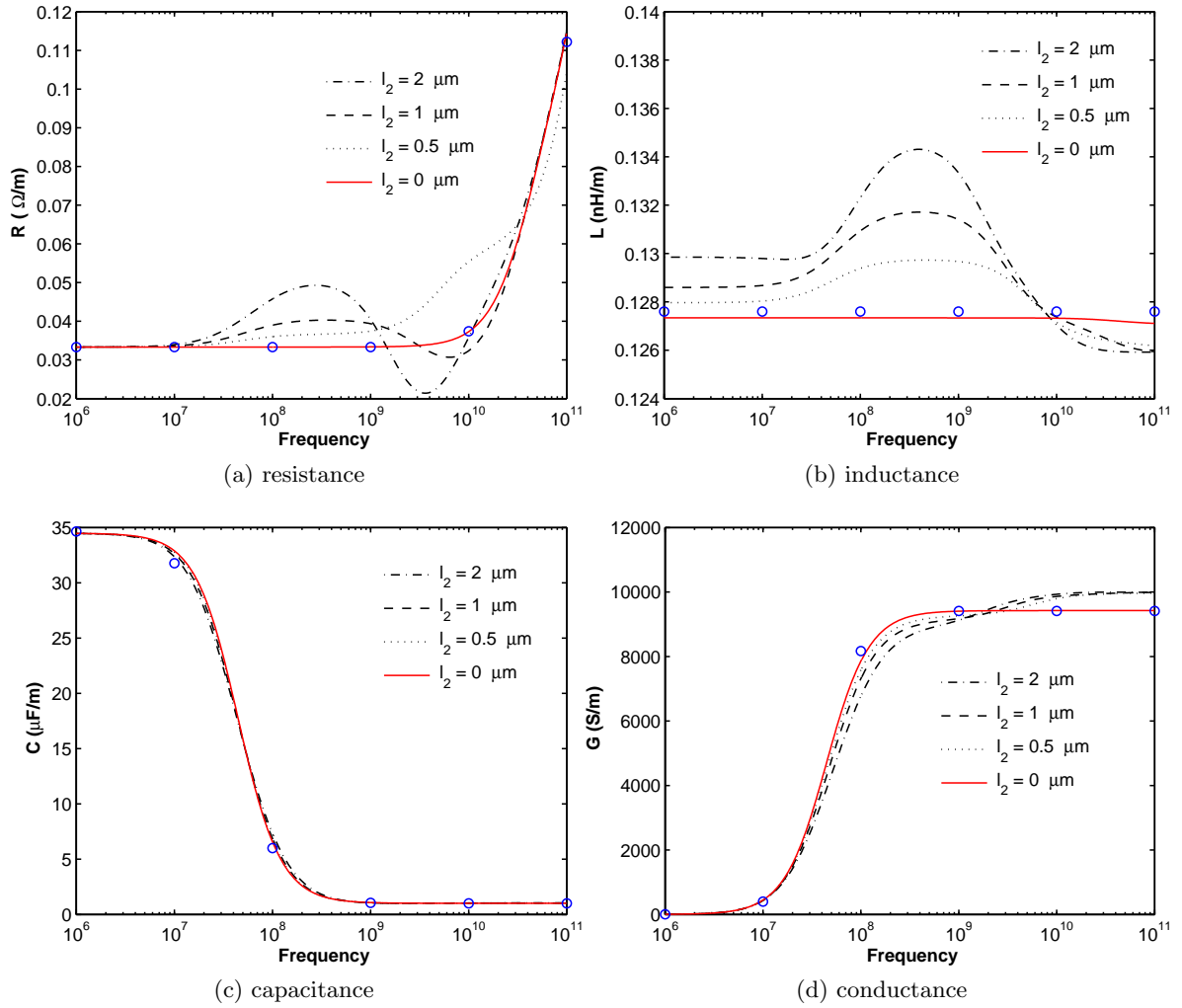
Figure 2.7: Frequency-dependent extracted R, L, C, and G per unit length versus l_2 for a 4-layered MIMS Transmission line in Fig. 2.1(b) with semiconductor: $\varepsilon_{r1} = 11.7$, $\sigma_1 = 1\,\text{S/m}$, $l_1 = 100\,\mu\text{m}$, insulator: $\varepsilon_{r3} = 3.9$, $l_3 = 1\,\mu\text{m}$, metallization: $l_4 = 1\,\mu\text{m}$, $\sigma_2 = \sigma_4 = 3 \times 10^7\,\text{S/m}$ (circles: data from [49]).

CHAPTER 3.   THE SPECTRAL DOMAIN APPROACH FOR GENERALIZED MULTILAYERED STRUCTURES

The SDA is one of the most popular numerical methods for analyzing planar multilayered microwave- and millimeter-wave passive structures. Its basic methodology is very straight-forward: introducing the Fourier transformation in the spatial domain. This transformation results in a wave equation with less dimension in the spectral domain, which simplifies the solving process and achieves some analytical formulations. According to [43], the SDA has several features:

- Easy formulation for dyadic Green's functions for multilayered structures

- Variational nature in the determination of propagation constant

- Identification of the physical natures from the solutions of basis functions

The SDA is applicable to the following structures: open and enclosed (shielded) planar multilayered transmission lines, slow-wave transmission lines with lossy dielectric materials, and resonators and antennas with planar configurations, etc. The numerical efficiency is the most prominent advantage. However, this feature imposes certain restrictions and limitations. First, the basis functions should have analytical forms after the Fourier transformation. Second, the thickness of signal strip conductor is normally treated as infinitesimally thin.[1] Third, no discontinuity and variation of material properties along lateral directions are allowed in the planar configures.

Because of its versatility of analyzing multilayered microwave components and patch antennas, the SDA has been intensively studied for decades. In 1971, Denlinger [20] used coupled

---

[1]The modified SDA models are introduced in Chapter 4.

integral equations in the spectral domain to solve single-layered open microstrip lines. In 1973, Itoh and Mittra [21] found a systematical way to derive the spectral-domain Green's functions for single-layered microstrip lines, simplified the coupled integral equations into linear algebraic ones, and solved them using the MoM. In 1977, a general spectral domain formulation for multilayered multiconductor microstrip lines was proposed by Davies and Mirshekar-Syahkal [22]. They applied the transfer matrices to match the boundary conditions on dielectric interfaces. Later, using the complex dielectric constant and perturbation method, the dielectric loss of multilayered structure was estimated by Mirshekar-Syahkal [24]. In 1980, Itoh [23] introduced a numerically more robust method: the immitance approach to account for multilayered structures. Das and Pozar [52], [53] developed the general spectral-domain Green's functions to analyze the conductor, dielectric and radiation loss for multilayered transmission lines.

In this chapter, the spectral domain techniques and the theoretical background are introduced. Section 3.1 briefly reviews the potential functions in electromagnetic theory and the Fourier transformation. The derivation of the spectral-domain Green's functions for the multilayered transmission lines is introduced in Section 3.2. In Sections 3.3 and 3.4, the propagation constants and currents are solved by the MoM as unknown eigenvalues and eigenvectors.

3.1 Electromagnetic Theory and Integral Equation Methods

The SDA is an integral-equation-based method that requires the relevant Green's functions for the structure under study. The Green's functions are the solutions of certain partial differential equation, which are obtained by using impulse sources as driving functions. The Dirac delta is an example for the impulse function. In engineering terminology, the Green's functions are named as the impulse responses or transfer functions for linear and time-invariant systems. Because of the superposition and time-invariant properties of linear systems, the output of an arbitrary source can be represented in the form of convolution integral with the impulse response [56]. In electromagnetic problems, the Green's functions describe the relationship between sources ($\mathbf{J}$, $\mathbf{M}$, q_e, q_m) and fields ($\mathbf{E}$, $\mathbf{H}$) under specific BCs.

The general technique for deriving multilayered Green's functions has shown a significant

reduction in algebraic complexity if vector and scalar potentials are used to expend the EM fields. The spectral domain technique definitely belongs to this category. According to the Maxwell's equations, the electromagnetic fields in a source-free region can be expressed by the electric and magnetic vector potentials $\mathbf{A}$ and $\mathbf{F}$ (or Hertzian potentials Π_e and Π_m) as [56]

$$\mathbf{E} = -j\omega\mathbf{A} - \nabla\Phi_e - \frac{1}{\varepsilon}\nabla \times \mathbf{F} \tag{3.1}$$

$$\mathbf{H} = \frac{1}{\mu}\nabla \times \mathbf{A} - j\omega\mathbf{F} - \nabla\Phi_m \tag{3.2}$$

and

$$\nabla \cdot \mathbf{A} = -j\omega\varepsilon\mu\Phi_e \tag{3.3}$$

$$\nabla \cdot \mathbf{F} = -j\omega\varepsilon\mu\Phi_m \tag{3.4}$$

where Φ_e and Φ_m are the electric and magnetic scalar potentials, respectively. ω is the angular frequency, while ε and μ are the permittivity and permeability of dielectric. Any EM field in source-free region can be decomposed as the linear combination of TE and TM modes that are also complete and orthogonal basis modes. Another combination is the longitudinal-section electric (LSE) modes and longitudinal-section magnetic (LSM) modes with respect to the interface [57]. For example, by assuming the z axis as the longitudinal direction, arbitrary fields in the medium (ε, μ) can be described as a superposition of the TM^z and TE^z modes as

$$\mathbf{A} = \hat{z}A_z e^{-j\gamma_z z}, \ \mathbf{F} = 0 \quad (\text{TM}^z) \tag{3.5}$$

$$\mathbf{A} = 0, \ \mathbf{F} = \hat{z}F_z e^{-j\gamma_z z} \quad (\text{TE}^z) \tag{3.6}$$

where γ_z is the propagation constant along the z axis. According to (3.3) and (3.4), the vector potentials can be written in the form of scalar potentials Ψ_e and Ψ_m, where $\Psi_{e,m} = -\Phi_{e,m}$.[2] For the 2-dimensional problem, the scalar potential functions are the solutions of the scalar Helmholtz equation in the spatial domain as

$$\nabla_t^2\Psi_{e,m}(x,y) + (k^2 - \gamma_z^2)\Psi_{e,m}(x,y) = 0 \tag{3.7}$$

---

[2]The minus sign helps to keep the formulations consistent with [21], [22].

where $k^2 = \omega^2 \varepsilon \mu$ and $\nabla_t = \frac{\partial}{\partial x}\hat{x} + \frac{\partial}{\partial y}\hat{y}$. Combining the TM^z and TE^z modes together, the field components in the dielectric are expressed as [21]

$$E_z(x,y) = j\frac{k^2 - \gamma_z^2}{\gamma_z}\Psi_e(x,y)e^{-j\gamma_z z} \tag{3.8}$$

$$\mathbf{E_t}(x,y) = \nabla_t \Psi_e(x,y)e^{-j\gamma_z z} - \frac{\omega\mu}{\gamma_z}\hat{z} \times \nabla_t \Psi_m(x,y)e^{-j\gamma_z z} \tag{3.9}$$

$$H_z(x,y) = j\frac{k^2 - \gamma_z^2}{\gamma_z}\Psi_m(x,y)e^{-j\gamma_z z} \tag{3.10}$$

$$\mathbf{H_t}(x,y) = \nabla_t \Psi_m(x,y)e^{-j\gamma_z z} + \frac{\omega\varepsilon}{\gamma_z}\hat{z} \times \nabla_t \Psi_e(x,y)e^{-j\gamma_z z} \tag{3.11}$$

where $\hat{z}$ is the unit vector of z axis. Next, if considering the Fourier transform along the x axis as the lateral direction, we have

$$\widetilde{\Psi}_{e,m}(\alpha,y) = \int_{-\infty}^{\infty} \Psi_{e,m}(x,y)e^{j\alpha x}dx \tag{3.12}$$

$$\Psi_{e,m}(x,y) = \frac{1}{2\pi}\int_{-\infty}^{\infty} \widetilde{\Psi}_{e,m}(\alpha,y)e^{-j\alpha x}d\alpha \tag{3.13}$$

where the tilde denotes all Fourier transform quantities in the spectral domain. After the Fourier transform, the 2-dimensional Helmholtz equation (3.7) degrades into a 1-dimensional wave equation in the spectral domain as

$$\frac{\partial^2}{\partial y^2}\widetilde{\Psi}_{e,m}(\alpha,y) - \gamma^2 \widetilde{\Psi}_{e,m}(\alpha,y) = 0 \tag{3.14}$$

where $\gamma^2 = \alpha^2 + \gamma_z^2 - \omega^2\varepsilon\mu$ is actually the simple showing of γ_y^2, the propagation constant along the y direction. Here the property of the Fourier transform on the first derivative of a function is applied. The general solution set for above Helmholtz equation is in the form of

$$\sinh(\gamma y), \cosh(\gamma y), \text{ or } e^{\pm\gamma y}. \tag{3.15}$$

Using these basic solutions with corresponding coefficients, all field components are explicitly expressed, which simplifies the problem into solving unknown coefficients of potentials. This method will be carried out in depth as follows to derive the multilayered Green's functions.

3.2 Full-Wave Multilayered Green's Functions in the Spectral Domain

In this section, two different methods, the transfer matrix method [22] and the spectral-domain immittance approach (SDIA) [23], are implemented to get the multilayered Green's

functions. Although these two methods are mathematically equivalent, they own different physical insights: the transfer matrix method focus more on the field components and BCs, while the SDIA is based intensively on the physical circuit and transmission line models.
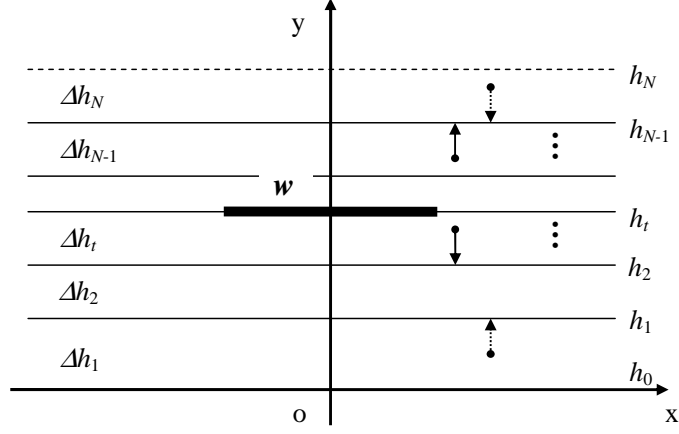
Figure 3.1: A general N-layered transmission line structure.

The configuration of a general 2-dimensional N-layered planar transmission line is illustrated in Fig. 3.1. The cross section is located on the xoy plane. All layers are uniform and infinite in both x and z directions. The absolute interface height of the interface between the ith and $(i+1)$th layers is defined as h_i. Likewise, Δh_i is the layer thickness. Dielectric parameters are the permittivity ε_i, permeability μ_i, and conductivity σ_i. The signal strip with a width w is mounted on the interface h_t and normally modeled as the infinitesimally thin PEC. For the uppermost and lowermost layers ($i = 1, N$), the most common BCs are the free space (open), PEC (shielded), and PMC. In this structure, guided waves are assumed to propagate along the z direction. Using the auxiliary electrical potential $\widetilde{\Psi}_e$ and magnetic potential $\widetilde{\Psi}_m$ in the spectral domain, the Green's functions are derived as follows.

3.2.1 Spectral-Domain Transfer Matrix Method

The procedures similar to [22], [25] are followed. The whole region is divided into two parts: layers above and below the signal strip. The recursive transfer matrices for these two parts can be deduced to match the BCs. There are two kinds of spatial BCs on dielectric interfaces:

the ones with and without the signal strips.

$$E_{z,i} = E_{z,i+1} \tag{3.16}$$

$$E_{x,i} = E_{x,i+1} \tag{3.17}$$

$$H_{z,i} - H_{z,i+1} = \begin{cases} 0 & (i \neq t) \\ -J_x e^{-j\gamma_z z} & (i = t) \end{cases} \tag{3.18}$$

$$H_{x,i} - H_{x,i+1} = \begin{cases} 0 & (i \neq t) \\ J_z e^{-j\gamma_z z} & (i = t) \end{cases} \tag{3.19}$$

The BCs in the spectral domain hold the similar formulation as above by applying the Fourier transform. In the following, the solutions for these two regions will be represented to derive the Green's functions on the interface h_t.

3.2.1.1 Layers below the signal strip

For each layer, the general potential solutions for the wave equation (3.14) are

$$\begin{aligned} \widetilde{\Psi}_{e,i} &= A_i e^{\gamma_i(y-h_{i-1})} + B_i e^{-\gamma_i(y-h_{i-1})} \\ \widetilde{\Psi}_{m,i} &= C_i e^{\gamma_i(y-h_{i-1})} + D_i e^{-\gamma_i(y-h_{i-1})} \end{aligned} \quad (i = 1, 2, 3, \ldots, t, \ h_{i-1} \leq y < h_i) \tag{3.20}$$

where $\gamma_i^2 = \alpha^2 + \gamma_z^2 - \omega^2 \varepsilon_i \mu_i$. A_i, B_i, C_i, and D_i are unknown coefficients and functions of α. Writing field components in the potential form, the BCs on the interface h_i are matched as

$$
\begin{bmatrix} -j\gamma_z \widetilde{E}_z(h_i) \\ -j\gamma_z \widetilde{H}_z(h_i) \\ \widetilde{E}_x(h_i) \\ \widetilde{H}_x(h_i) \end{bmatrix} =
\begin{bmatrix} k_i^2 - \gamma_z^2 & k_i^2 - \gamma_z^2 & 0 & 0 \\ 0 & 0 & k_i^2 - \gamma_z^2 & k_i^2 - \gamma_z^2 \\ -j\alpha & -j\alpha & \frac{\omega\mu_i\gamma_i}{\gamma_z} & -\frac{\omega\mu_i\gamma_i}{\gamma_z} \\ -\frac{\omega\varepsilon_i\gamma_i}{\gamma_z} & \frac{\omega\varepsilon_i\gamma_i}{\gamma_z} & -j\alpha & -j\alpha \end{bmatrix}
\begin{bmatrix} A_i e^{\gamma_i \Delta h_i} \\ B_i e^{-\gamma_i \Delta h_i} \\ C_i e^{\gamma_i \Delta h_i} \\ D_i e^{-\gamma_i \Delta h_i} \end{bmatrix}
$$

$$
=
\begin{bmatrix} k_{i+1}^2 - \gamma_z^2 & k_{i+1}^2 - \gamma_z^2 & 0 & 0 \\ 0 & 0 & k_{i+1}^2 - \gamma_z^2 & k_{i+1}^2 - \gamma_z^2 \\ -j\alpha & -j\alpha & \frac{\omega\mu_{i+1}\gamma_{i+1}}{\gamma_z} & -\frac{\omega\mu_{i+1}\gamma_{i+1}}{\gamma_z} \\ -\frac{\omega\varepsilon_{i+1}\gamma_{i+1}}{\gamma_z} & \frac{\omega\varepsilon_{i+1}\gamma_{i+1}}{\gamma_z} & -j\alpha & -j\alpha \end{bmatrix}
\begin{bmatrix} A_{i+1} \\ B_{i+1} \\ C_{i+1} \\ D_{i+1} \end{bmatrix} \tag{3.21}
$$

where $\Delta h_i = h_i - h_{i-1}$ $(i = 2, 3, \ldots, t-1)$, $h_0 = 0$, and $k_i^2 = \omega^2 \varepsilon_i \mu_i$. Thus it is straightforward to express the coefficients A_i, B_i, C_i and D_i in the form of $A_{i-1}, B_{i-1}, C_{i-1}$, and D_{i-1}

$$\begin{bmatrix} A_i \\ B_i \\ C_i \\ D_i \end{bmatrix} \equiv \begin{bmatrix} T_i \end{bmatrix}^{-1} \begin{bmatrix} T_{i-1} \end{bmatrix} \begin{bmatrix} D(\gamma_{i-1}\Delta h_{i-1}) \end{bmatrix} \begin{bmatrix} A_{i-1} \\ B_{i-1} \\ C_{i-1} \\ D_{i-1} \end{bmatrix} \equiv \begin{bmatrix} M_{i,i-1} \end{bmatrix} \begin{bmatrix} A_{i-1} \\ B_{i-1} \\ C_{i-1} \\ D_{i-1} \end{bmatrix} \tag{3.22}$$

where $i = 3, 4, \ldots, t$ (not including the first layer). The defined matrices $[T]$ and $[D]$ are

$$\begin{bmatrix} T_{i-1} \end{bmatrix} = \begin{bmatrix} k_{i-1}^2 - \gamma_z^2 & k_{i-1}^2 - \gamma_z^2 & 0 & 0 \\ 0 & 0 & k_{i-1}^2 - \gamma_z^2 & k_{i-1}^2 - \gamma_z^2 \\ -j\alpha & -j\alpha & \frac{\omega\mu_{i-1}\gamma_{i-1}}{\gamma_z} & -\frac{\omega\mu_{i-1}\gamma_{i-1}}{\gamma_z} \\ -\frac{\omega\varepsilon_{i-1}\gamma_{i-1}}{\gamma_z} & \frac{\omega\varepsilon_{i-1}\gamma_{i-1}}{\gamma_z} & -j\alpha & -j\alpha \end{bmatrix} \tag{3.23}$$

and

$$\begin{bmatrix} D(\gamma_{i-1}\Delta h_{i-1}) \end{bmatrix} = \begin{bmatrix} e^{\gamma_{i-1}\Delta h_{i-1}} & & & \\ & e^{-\gamma_{i-1}\Delta h_{i-1}} & & \\ & & e^{\gamma_{i-1}\Delta h_{i-1}} & \\ & & & e^{-\gamma_{i-1}\Delta h_{i-1}} \end{bmatrix}. \tag{3.24}$$

The inverse matrix of $[T_i]$ has an analytical form as

$$\begin{bmatrix} T_i \end{bmatrix}^{-1} = \frac{1}{2(k_i^2 - \gamma_z^2)} \begin{bmatrix} 1 & -j\frac{\alpha\gamma_z}{\omega\gamma_i\varepsilon_i} & 0 & -\frac{\gamma_z(k_i^2-\gamma_z^2)}{\omega\gamma_i\varepsilon_i} \\ 1 & j\frac{\alpha\gamma_z}{\omega\gamma_i\varepsilon_i} & 0 & \frac{\gamma_z(k_i^2-\gamma_z^2)}{\omega\gamma_i\varepsilon_i} \\ j\frac{\alpha\gamma_z}{\omega\gamma_i\mu_i} & 1 & \frac{\gamma_z(k_i^2-\gamma_z^2)}{\omega\gamma_i\mu_i} & 0 \\ -j\frac{\alpha\gamma_z}{\omega\gamma_i\mu_i} & 1 & -\frac{\gamma_z(k_i^2-\gamma_z^2)}{\omega\gamma_i\mu_i} & 0 \end{bmatrix}. \tag{3.25}$$

From above equation that links the coefficients between the ith and $(i-1)$th layers, we can write the chained backward transfer matrices starting from the layer t as

$$\begin{bmatrix} A_t \\ B_t \\ C_t \\ D_t \end{bmatrix} = \begin{bmatrix} M_{t,t-1} \end{bmatrix} \begin{bmatrix} M_{t-1,t-2} \end{bmatrix} \begin{bmatrix} M_{t-2,t-3} \end{bmatrix} \cdots \begin{bmatrix} \widetilde{A} \\ 0 \\ \widetilde{C} \\ 0 \end{bmatrix} \tag{3.26}$$

where $\widetilde{A}$ and $\widetilde{C}$ are unknown coefficients for the lowermost layer ($i = 1$). Basically, three different BCs are commonly used for this layer: the PEC and PMC on the interface h_0, and the open space on h_1 where material (ε_1, μ_1) fills all the half space below h_1. The corresponding matrices are formulated in Appendix B.

3.2.1.2 Layers above the signal strip

Similarly, if considering the symmetry, the general solutions for the wave equation in y direction are written as

$$
\begin{aligned}
\widetilde{\Psi}_{e,i} &= A_i e^{\gamma_i(y-h_i)} + B_i e^{-\gamma_i(y-h_i)} \\
\widetilde{\Psi}_{m,i} &= C_i e^{\gamma_i(y-h_i)} + D_i e^{-\gamma_i(y-h_i)}
\end{aligned}
\qquad (i = t+1, \ldots, N,\ h_{i-1} \le y < h_i). \qquad (3.27)
$$

On the interface h_i, the neighboring coefficients are matched with BCs in the matrix form as

$$
\begin{bmatrix} A_i \\ B_i \\ C_i \\ D_i \end{bmatrix} \equiv \left[T_i \right]^{-1} \left[T_{i+1} \right] \left[D(-\gamma_{i+1}\Delta h_{i+1}) \right] \begin{bmatrix} A_{i+1} \\ B_{i+1} \\ C_{i+1} \\ D_{i+1} \end{bmatrix} \equiv \left[M'_{i,i+1} \right] \begin{bmatrix} A_{i+1} \\ B_{i+1} \\ C_{i+1} \\ D_{i+1} \end{bmatrix} \qquad (3.28)
$$

where

$$
\left[D(-\gamma_{i+1}\Delta h_{i+1}) \right] = \begin{bmatrix} e^{-\gamma_{i+1}\Delta h_{i+1}} & & & \\ & e^{\gamma_{i+1}\Delta h_{i+1}} & & \\ & & e^{-\gamma_{i+1}\Delta h_{i+1}} & \\ & & & e^{\gamma_{i+1}\Delta h_{i+1}} \end{bmatrix} \qquad (3.29)
$$

$\Delta h_{i+1} = h_{i+1} - h_i$ and $i = t, t+1, \ldots, N-2$. The matrix $[T]$ keeps the same definition as before. Thus the chained forward transfer matrices for the layers above h_t are

$$
\begin{bmatrix} A_t \\ B_t \\ C_t \\ D_t \end{bmatrix} = \left[M'_{t,t+1} \right] \left[M'_{t+1,t+2} \right] \left[M'_{t+2,t+3} \right] \cdots \begin{bmatrix} 0 \\ \widetilde{B} \\ 0 \\ \widetilde{D} \end{bmatrix}. \qquad (3.30)
$$

Different BCs on the interface h_N relate to specific matrices that are listed in Appendix B.

3.2.1.3 Spectral-domain Green's functions on the interface h_t

On the interface h_t where the signal strip is located, there exist electric current sources as $\widetilde{J}_x$ and $\widetilde{J}_z$. According the BCs of (3.16)-(3.19), the relationship between coefficients of potentials and current sources can be written in the matrix form as

$$
\left[T_t \right] \left[D(\gamma_t \Delta h_t) \right] \left[M_{t,t-1} \right] \left[M_{t-2,t-3} \right] \cdots \begin{bmatrix} \widetilde{A} \\ 0 \\ \widetilde{C} \\ 0 \end{bmatrix}
$$
$$
- \left[T_{t+1} \right] \left[D(-\gamma_{t+1} \Delta h_{t+1}) \right] \left[M'_{t+1,t+2} \right] \left[M'_{t+2,t+3} \right] \cdots \begin{bmatrix} 0 \\ \widetilde{B} \\ 0 \\ \widetilde{D} \end{bmatrix} = \begin{bmatrix} 0 \\ j\gamma_z \widetilde{J}_x \\ 0 \\ \widetilde{J}_z \end{bmatrix} \tag{3.31}
$$

where $\widetilde{J}_x$ and $\widetilde{J}_z$ are surface current densities in the spectral domain. Coefficients $\widetilde{A}$, $\widetilde{B}$, $\widetilde{C}$, and $\widetilde{D}$ are dependent on the BCs on h_0 and h_N. For the diagonal matrix $[D]$, the common exponential entries can be extracted, then the matrices are reformed as

$$
\left[D(\gamma_i \Delta h_i) \right] = e^{\gamma_i \Delta h_i} \begin{bmatrix} 1 & & & \\ & e^{-2\gamma_i \Delta h_i} & & \\ & & 1 & \\ & & & e^{-2\gamma_i \Delta h_i} \end{bmatrix} \quad (i = 2, \dots, t) \tag{3.32}
$$

$$
\left[D(-\gamma_j \Delta h_j) \right] = e^{\gamma_j \Delta h_j} \begin{bmatrix} e^{-2\gamma_j \Delta h_j} & & & \\ & 1 & & \\ & & e^{-2\gamma_j \Delta h_j} & \\ & & & 1 \end{bmatrix} \quad (j = t+1, t+2, \dots, N-1). \tag{3.33}
$$

Such common factors can be extracted further from chained matrices and combined with the unknown coefficients $\widetilde{A}$, $\widetilde{B}$, $\widetilde{C}$, and $\widetilde{D}$. Now the remaining part of $[D]$ matrix only has finite-value entries. With this technique, a simplified form of (3.31) is achieved with new notations

of the cascaded matrices $[K]$ and $[L]$ as

$$
\begin{bmatrix} K \end{bmatrix} \begin{bmatrix} \widetilde{A}e^{\sum_{i=2}^{t}\gamma_i\Delta h_i} \\ 0 \\ \widetilde{C}e^{\sum_{i=2}^{t}\gamma_i\Delta h_i} \\ 0 \end{bmatrix} - \begin{bmatrix} L \end{bmatrix} \begin{bmatrix} 0 \\ \widetilde{B}e^{\sum_{j=t+1}^{N-1}\gamma_j\Delta h_j} \\ 0 \\ \widetilde{D}e^{\sum_{j=t+1}^{N-1}\gamma_j\Delta h_j} \end{bmatrix} = \begin{bmatrix} 0 \\ j\gamma_z\widetilde{J}_x \\ 0 \\ \widetilde{J}_z \end{bmatrix} \tag{3.34}
$$

where $[K]$ and $[L]$ matrices have no large exponential entries that can cause overflow problem when the argument α is large. Rearranging above (3.34), it yields

$$
\begin{bmatrix} \widetilde{A}e^{\sum_{i=2}^{t}\gamma_i\Delta h_i} \\ \widetilde{C}e^{\sum_{i=2}^{t}\gamma_i\Delta h_i} \\ \widetilde{B}e^{\sum_{j=t+1}^{N-1}\gamma_j\Delta h_j} \\ \widetilde{D}e^{\sum_{j=t+1}^{N-1}\gamma_j\Delta h_j} \end{bmatrix} = \begin{bmatrix} k_{1,1} & k_{1,3} & -l_{1,2} & -l_{1,4} \\ k_{2,1} & k_{2,3} & -l_{2,2} & -l_{2,4} \\ k_{3,1} & k_{3,3} & -l_{3,2} & -l_{3,4} \\ k_{4,1} & k_{4,3} & -l_{4,2} & -l_{4,4} \end{bmatrix}^{-1} \begin{bmatrix} 0 \\ j\gamma_z\widetilde{J}_x \\ 0 \\ \widetilde{J}_z \end{bmatrix} \equiv \begin{bmatrix} V \end{bmatrix} \begin{bmatrix} 0 \\ j\gamma_z\widetilde{J}_x \\ 0 \\ \widetilde{J}_z \end{bmatrix} \tag{3.35}
$$

where $k_{i,j}$ and $l_{i,j}$ are (i,j)th entries of the matrices $[K]$ and $[L]$, respectively. For particular current sources on the strip, above equation gives $\widetilde{A}$ and $\widetilde{C}$ or $\widetilde{B}$ and $\widetilde{D}$, as middle variables, to connect electric fields $\widetilde{E}_x$ and $\widetilde{E}_z$ with the current sources $\widetilde{J}_x$ and $\widetilde{J}_z$. Thus the corresponding Green's functions on the interface h_t are

$$
\begin{bmatrix} \widetilde{E}_x \\ \widetilde{E}_z \end{bmatrix} = \begin{bmatrix} \widetilde{G}_{xx}(\alpha,\gamma_z) & \widetilde{G}_{xz}(\alpha,\gamma_z) \\ \widetilde{G}_{zx}(\alpha,\gamma_z) & \widetilde{G}_{zz}(\alpha,\gamma_z) \end{bmatrix} \begin{bmatrix} \widetilde{J}_x \\ \widetilde{J}_z \end{bmatrix} \tag{3.36}
$$

where

$$
\widetilde{G}_{xx} = j\gamma_z(k_{3,1}v_{1,2} + k_{3,3}v_{2,2}) = j\gamma_z(l_{3,2}v_{3,2} + l_{3,4}v_{4,2}) \tag{3.37}
$$

$$
\widetilde{G}_{xz} = k_{3,1}v_{1,4} + k_{3,3}v_{2,4} = l_{3,2}v_{3,4} + l_{3,4}v_{4,4} \tag{3.38}
$$

$$
\widetilde{G}_{zx} = -(k_{1,1}v_{1,2} + k_{1,3}v_{2,2}) = -(l_{1,2}v_{3,2} + l_{1,4}v_{4,2}) = \widetilde{G}_{xz} \tag{3.39}
$$

$$
\widetilde{G}_{zz} = \frac{j}{\gamma_z}(k_{1,1}v_{1,4} + k_{1,3}v_{2,4}) = \frac{j}{\gamma_z}(l_{1,2}v_{4,2} + l_{1,4}v_{4,4}) \tag{3.40}
$$

and $v_{i,j}$ is the (i,j)th entry of the matrix $[V]$. The dimension of the Green's functions is Ohm (Ω) that is same as the surface impedance. After the Fourier transform, the convolution integral in the spatial domains becomes the algebraic multiplication in the spectral domain. Another important advantage of (3.36) is that the order of matrix is not dependent on the number of dielectric layers but on the representation of current sources.

3.2.2 Spectral-Domain Immitance Approach

In the transfer matrix method, the unknown coefficients of potentials act as the bridge between electric fields and current sources. However, the derived Green's functions are obscure to gain physical insights into the problem. In addition, the transfer matrix method is relatively slow due to the matrix inverse operation for $[V]$. The SDIA proposed by Itoh [23] overcomes these disadvantages, and has less complexity and higher numerical efficiency.
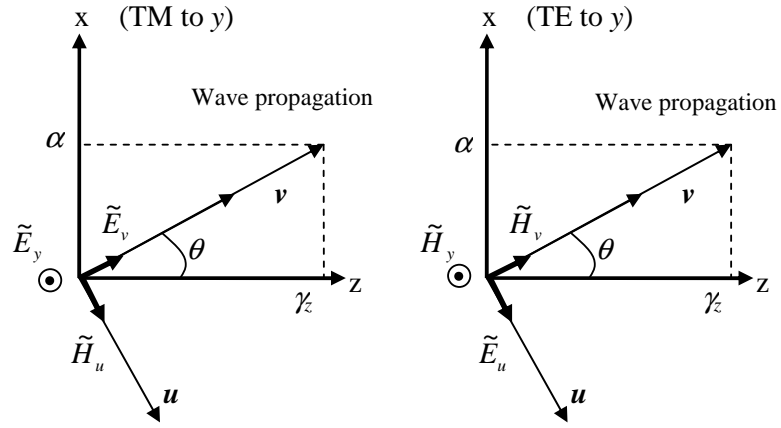
Figure 3.2: Transformation between the (u, v) and (x, y) coordinates as in [23].

The SDIA basically implements equivalent transverse transmission line models to sources and fields. Unlike the transfer matrix method, this approach divides hybrid fields into TM^y and TE^y modes. If all transverse components in the (x, z) coordinate are rotated into the new coordinate as the (u, v) shown in Fig. 3.2 as

$$
\begin{bmatrix} \hat{u} \\ \hat{v} \end{bmatrix} = \begin{bmatrix} -\cos\theta & \sin\theta \\ \sin\theta & \cos\theta \end{bmatrix} \begin{bmatrix} \hat{x} \\ \hat{z} \end{bmatrix}
\tag{3.41}
$$

where $\cos\theta = \gamma_z/\sqrt{\alpha^2 + \gamma_z^2}$, the original boundary-value problem is decomposed into two independent transmission line equations. For each θ, waves are decoupled into TM^y $(\widetilde{E}_y, \widetilde{E}_v, \widetilde{H}_u)$ and TE^y $(\widetilde{H}_y, \widetilde{H}_v, \widetilde{E}_u)$ modes in the (u, v) coordinate. Furthermore, the current $\widetilde{J}_v$, which relates to $\widetilde{H}_u$, excites the TM^y mode only. Likewise, $\widetilde{J}_u$ excites the TE^y modes only.

Fig. 3.3 shows two equivalent N-layered transmission lines for TE and TM modes separately. The current source is located on the interface h_t. The relationship between the transverse
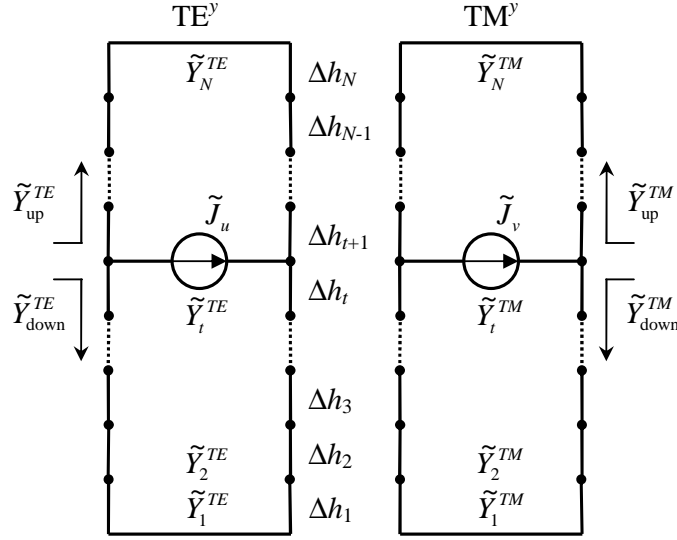
Figure 3.3: Equivalent transmission line models for TE- and TM-modes in multilayered structures [23].

electric fields ($\widetilde{E}_u$ and $\widetilde{E}_v$) and current sources ($\widetilde{J}_u$ and $\widetilde{J}_v$) on h_t can be written in a matrix notation as

$$\begin{bmatrix} \widetilde{E}_u \\ \widetilde{E}_v \end{bmatrix} = \begin{bmatrix} -1/\widetilde{Y}^{TE} & 0 \\ 0 & -1/\widetilde{Y}^{TM} \end{bmatrix} \begin{bmatrix} \widetilde{J}_u \\ \widetilde{J}_v \end{bmatrix} = \begin{bmatrix} -\widetilde{Z}^{TE} & 0 \\ 0 & -\widetilde{Z}^{TM} \end{bmatrix} \begin{bmatrix} \widetilde{J}_u \\ \widetilde{J}_v \end{bmatrix} \tag{3.42}$$

where $\widetilde{Y}^{TE}$ and $\widetilde{Y}^{TM}$ are the driving-point admittances for TE and TM modes, respectively. Equation (3.42) is also the Green's function in the (u, v) coordinate. The driving-point admittance can be calculated directly from two equivalent admittances as looking-up and looking-down from the interface h_t

$$Y^{TE/TM} = Y_{\text{up}}^{TE/TM} + Y_{\text{down}}^{TE/TM} \tag{3.43}$$

where $Y_{\text{up}}^{TE/TM}$ and $Y_{\text{down}}^{TE/TM}$ are in parallel. The equivalent admittances can be readily calculated from the impedance transformation of transmission lines recursively

$$Y^{TE/TM} = Y_0^{TE/TM} \frac{Y_L^{TE/TM} + Y_0^{TE/TM} \tanh(\gamma \Delta h)}{Y_0^{TE/TM} + Y_L^{TE/TM} \tanh(\gamma \Delta h)} \tag{3.44}$$

where γ and Δh are the propagation constant and layer thickness. $Y_L^{TE/TM}$ is the loaded admittance from previous interface. $Y_0^{TE/TM}$ is the wave characteristic admittance

$$Y_0^{TM} = \frac{j\omega\varepsilon}{\gamma} \text{ and } Y_0^{TE} = \frac{\gamma}{j\omega\mu}. \tag{3.45}$$

Using the coordinate rotation (3.41) back to the (x,z) coordinate, the Green's functions that are equivalent to (3.36) can be obtained as

$$\widetilde{G}_{xx} = -\left(\cos^2\theta Z^{TE} + \sin^2\theta Z^{TM}\right) = -\frac{\gamma_z^2 Z^{TE} + \alpha^2 Z^{TM}}{\alpha^2 + \gamma_z^2} \tag{3.46}$$

$$\widetilde{G}_{xz} = -\cos\theta\sin\theta\left(Z^{TM} - Z^{TE}\right) = -\frac{\alpha\gamma_z\left(Z^{TM} - Z^{TE}\right)}{\alpha^2 + \gamma_z^2} \tag{3.47}$$

$$\widetilde{G}_{zz} = -\left(\sin^2\theta Z^{TE} + \cos^2\theta Z^{TM}\right) = -\frac{\alpha^2 Z^{TE} + \gamma_z^2 Z^{TM}}{\alpha^2 + \gamma_z^2} \tag{3.48}$$

$$\widetilde{G}_{zx} = \widetilde{G}_{zx}. \tag{3.49}$$

For the uppermost or lowermost layer, the admittance formulation depends on the BCs as the transfer matrix method. From the discussion, the SDIA can be conveniently extended to the multilayered-multiconductor structures.

3.3 The Method of Moments and Eigenvalue Problems

In this section, the linear system of equations (3.36) is solved by the MoM [58]. Given in general forms, all equations that we are concerned can be expressed as

$$Lf = g \tag{3.50}$$

where L is a linear operator that represents the system. f is an unknown function that refers to the response, while g is a known function that defines the source. For EM problems, f is unique when the BCs and g are specified. The basic idea of MoM is to project the unknown function f onto some vector space bases $\{f_n\}$ in an inner product space as

$$f^* = \sum_{n=1}^{M} c_n f_n \tag{3.51}$$

where c_n are unknown coefficients; M is the total number of bases. The approximation f^* should approach f when M increases. With defined inner product $< \cdot, \cdot >$, the difference between the exact solution Lf and the projection Lf^* is orthogonal to a function set called testing function or weighting function t_m, which yields

$$\sum_{n=1}^{M} c_n < t_m, Lf_n > = < t_m, g >, \quad m = 1, 2, \ldots, M \tag{3.52}$$

where M is also the total number of testing functions. By using the basis function f_n and testing function t_m, the MoM reduces the problem into linear equations of unknown coefficients c_n. The solution accuracy and computation efficiency depend intensively on the choice of $\{f_n\}$ and $\{t_m\}$. There are two well-known techniques to choose the testing function. One is the point matching method that uses delta functions as testing functions. The other is the Galerkin's method where testing functions are the same as basis functions. The Galerkin's method with a real operator results in a variational quality and a same procedure as the Rayleigh-Ritz method [43]. As long as a good choice made for basis functions, the Galerkin's method can give reasonable and accurate solutions.

To solve the current equations in (3.36), the first step is to expand the unknown currents on the signal strip in terms of basis functions as follows [59]

$$\widetilde{J}_x(\alpha) = \sum_{m=1}^{M_x} a_m \widetilde{J}_{x,m}(\alpha), \quad \widetilde{J}_z(\alpha) = \sum_{n=1}^{M_z} b_n \widetilde{J}_{z,n}(\alpha) \tag{3.53}$$

where a_m and b_n are unknown coefficients. The BCs require currents to be nonzero only on the signal strip and zero in other regions. These basis functions should also be incorporated with the singular behavior of the magnetic fields near the conductor edges. For instance, if we choose only one basis function for J_x and J_z, respectively, the current components can have the forms as [20]

$$J_z(x) = \begin{cases} 1 + |2x/w|^3, & |x| < 0.5w \\ \\ 0, & \text{elsewhere} \end{cases} \tag{3.54}$$

$$J_x(x) = \begin{cases} \sin\left[\pi x/(0.8w)\right], & |x| < 0.4w \\ \\ \pm \cos\left[\pi x/(0.2w)\right], & 0.4w < |x| < 0.5w \\ \\ 0, & \text{elsewhere} \end{cases} \tag{3.55}$$

whose corresponding Fourier transforms are

$$\widetilde{J}_z(\alpha) = \frac{2}{\alpha(\alpha w)^3}\left\{24 + 3\left[(\alpha w)^2 - 8\right]\cos\left(\frac{\alpha w}{2}\right) + \alpha w\left[(\alpha w)^3 - 12\right]\sin\left(\frac{\alpha w}{2}\right)\right\} \tag{3.56}$$

$$\widetilde{J}_x(\alpha) = j2w\left[\frac{\alpha w \cos(0.4\alpha w)}{(1.25\pi)^2 - (\alpha w)^2} + \frac{5\pi \sin(0.5\alpha w) - \alpha w \cos(0.4\alpha w)}{(5\pi)^2 - (\alpha w)^2}\right]. \tag{3.57}$$

Another widely used current basis function set is the Chebyshev polynomial with edge singularity [57]

$$J_z(x) = \sum_{n=0}^{M_z} b_n \frac{T_{2n}(2x/w)}{\sqrt{1 - (2x/w)^2}} \tag{3.58}$$

$$J_x(x) = \sqrt{1 - (2x/w)^2} \sum_{m=1}^{M_x} j a_m U_{2m-1}(2x/w) \tag{3.59}$$

where T_{2n} and U_{2m-1} are Chebyshev polynomial and Chebyshev polynomial of the second kind, respectively. The Fourier transformations are

$$\widetilde{J}_z(\alpha) = \sum_{n=0}^{M_z} b_n \frac{\pi w}{2} (-1)^n J_{2n}(\alpha w/2) \tag{3.60}$$

$$\widetilde{J}_x(\alpha) = \sum_{m=1}^{M_x} j a_m (-1)^m \frac{2\pi m}{\alpha} J_{2m}(\alpha w/2). \tag{3.61}$$

where J_{2n} and J_{2m} are the Bessel functions of the first kind.

By substituting above current bases in (3.36) and defining the infinite integral over α as the inner-product, the Galerkin's method yields

$$\sum_{m=1}^{M_x} a_m K_{i,m}^{xx} + \sum_{n=1}^{M_z} b_n K_{i,n}^{xz} = \int_{-\infty}^{\infty} \widetilde{J}_{x,i}(\alpha) \widetilde{E}_x(\alpha) d\alpha, \quad i = 1, 2, \ldots, M_x$$
$$\sum_{m=1}^{M_x} a_m K_{j,m}^{zx} + \sum_{n=1}^{M_z} b_n K_{j,n}^{zz} = \int_{-\infty}^{\infty} \widetilde{J}_{z,j}(\alpha) \widetilde{E}_z(\alpha) d\alpha, \quad j = 1, 2, \ldots, M_z \tag{3.62}$$

where K_{kl}^{pq} is the integration related to the inner product of the Green's functions and current bases

$$K_{kl}^{pq} = \int_{-\infty}^{\infty} \widetilde{J}_{p,k}(\alpha) \widetilde{G}_{pq}(\alpha, \gamma_z) \widetilde{J}_{q,l}(\alpha) d\alpha, \quad p, q = x, z. \tag{3.63}$$

The right hand sides of (3.62) become zero because of the complementary spatial distribution of electric fields and currents on the interface h_t. The BCs require surface currents $J_{x,i}$ and $J_{z,j}$ to be nonzero only on signal strips, for example $|x| < w/2$, and to vanish otherwise. On the contrary, tangential electric fields E_x and E_z must be zero on the surfaces of PEC strips. According to the Parseval's theorem, above right hand sides equal to zero after being transformed into the spatial domain.

$$\int_{-\infty}^{\infty} \widetilde{E}_x(\alpha) \widetilde{J}_{x,i}(\alpha) d\alpha = 2\pi \int_{-\infty}^{\infty} E_x(x) J_{x,i}(-x) dx = 0$$
$$\int_{-\infty}^{\infty} \widetilde{E}_z(\alpha) \widetilde{J}_{z,j}(\alpha) d\alpha = 2\pi \int_{-\infty}^{\infty} E_z(x) J_{z,j}(-x) dx = 0 \tag{3.64}$$

Then the problem changes into a homogeneous system of $M_x + M_z$ linear equations with respect to the unknown coefficients a_m and b_n. It can be written into a matrix form as

$$\left[K(\gamma_z) \right] \left[a_1 \; a_2 \; \ldots \; a_M \; b_1 \; b_2 \; \ldots \; b_N \right]^T = 0 \qquad (3.65)$$

where $[K]$ is a matrix with a dimension of $M_x + M_z$; γ_z is the unknown propagation constant. Because of the existence of nonzero solutions for coefficients a_m and b_n, the determinant value of the matrix $[K]$ must be zero

$$\det \left[K(\gamma_z) \right] = 0. \qquad (3.66)$$

Note that above equation is a nonlinear eigenvalue problem. The propagation modes and eigenvalues of the system directly correspond to the zeros of determinant. Unknown current coefficients are found by the eigenvector that relates to the zero eigenvalue of $[K]$. Nonlinear root-finding algorithms need to be applied to search the appropriate γ_z and associated coefficients a_m and b_n. The propagation constant γ_z is an important parameter for transmission lines, from which the other electrical parameters can be further evaluated. These topics will be discussed in the following chapters.

Strictly speaking, for eigenvalue problems of EM structures, the feasible eigenvalues and modes are neither dependent on nor related to the outer sources. Eigenvalues are intrinsic properties determined by the material specifics and BCs. For example, the propagation modes of a waveguide and the resonant frequencies of a cavity can be calculated without considering the source. However, using the integral-equation approach to solve the eigenvalues for transmission lines has a slightly different physical aspect. The procedure is more like exciting certain modes with definite current bases. To achieve high computation efficiency and accuracy, the basis functions should be chosen as close as possible to the real current distribution of certain mode. Furthermore, more terms of current bases should be used to capture the high order modes.

CHAPTER 4.   THE MODELING OF REAL METAL COMPONENTS WITH FINITE THICKNESS

Discussed in the previous chapter, most researchers modeled the metal components as PECs with infinitesimal thickness and infinite conductivity. However, in real interconnect networks, all metallization parts are made of imperfect conductors with large but finite conductivities. The relevant frequency-dependant skin effect and current proximity effect cannot be accurately described by the PEC model. Furthermore, the zero-thickness PEC approximation is feasible only when the width-to-thickness (w/t) ratio of conductor is large enough. Jäger [46] reported that the dominating influence of imperfect conductors on the propagation constant and attenuation cannot be neglected. Thus, this chapter intends to analysis the effects from the imperfect metal components. The major influences from the thin-film metal ground are studied by comparing different models. Meanwhile, approximate models for the signal strips are studied.

In this chapter, Section 4.1 focuses on the modeling of thin metallization ground planes. Section 4.2 discusses the modeling of signal strips with finite thickness. Different models are compared using numerical simulation results. Conclusions are discussed in Section 4.3.

4.1   Modeling of the Thin Metal Ground Layer

As mentioned in Chapter 1, the thin ground layer sandwiched in multilayered structures is usually fabricated with a metallization thickness from several angstroms (Å) to several microns. However, this metallization thickness may be comparable to the skin depth at some low frequencies, which causes the EM field penetration. To study this penetrable conductor film, several approximate models are compared with the exact solution to test the validity.

4.1.1 Models for Thin-Film Conductors

Fig. 4.1 illustrates the geometry of a multilayered microstrip line. The signal strip is located on the interface h_{i+1} with a width w. A thin-film metal ground layer (gray region), with a thickness t,[1] is one layer below the strip. The signal strip and the lowest boundary are treated as zero-thickness PECs so that we can investigate the influence attributed only from the thin-metal ground layer.
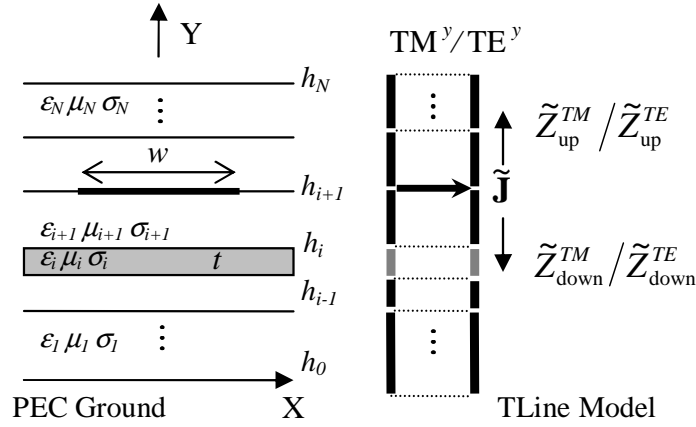
Figure 4.1: Geometry and equivalent transmission line models for a multilayered microstrip structure.

For such finite thin metallization layer, the PEC and IBC are not proper because they are impenetrable BCs and cannot describe the EM leakage phenomenon. In the literature, several approximate models were proposed such as the resistive sheet (R-card) [60], [61], TE/LSE- and TM/LSM-mode sheet impedance [62], etc. However, little comparison has been made among these models by far.

Using the SDIA, each layer is strictly modeled as the TE^y (LSE) and TM^y (LSM) mode admittances [63]. The highly conductive layer can be modeled by a complex relative permittivity $\dot{\varepsilon}_r$ as (2.1). Thus the equivalent cascaded impedance $Z_{\mathrm{down},i}$ seen downwards from h_i

---

[1]Here t is the metallization thickness, not the layer index used in the pervious chapter.

(in the negative y direction) is given as [23]

$$Z_{\text{down},i}^{TE/TM} = Z_m^{TE/TM} \frac{Z_{L,i-1}^{TE/TM} + Z_m^{TE/TM} \tanh(\gamma_c t)}{Z_m^{TE/TM} + Z_{L,i-1}^{TE/TM} \tanh(\gamma_c t)}$$
$$Z_m^{TE} = j\omega\mu/\gamma_c, \ Z_m^{TM} = \gamma_c/(j\omega\varepsilon_0\dot{\varepsilon}_r) \tag{4.1}$$
$$\gamma_c^2 = \alpha^2 + \gamma_z^2 - \omega^2\varepsilon_0\dot{\varepsilon}_r\mu$$

where $Z_{L,i-1}^{TE/TM}$ is the equivalent wave impedance seen downwards from h_{i-1}. γ_c is the wave number in conductor. In this section, this model is regarded as one exact solution to calibrate the other approximate models.

The IBC describes the relationship between the electric and magnetic fields on the boundary, which is defined as the surface impedance, when the metallization thickness is much thicker than the skin depth. This metallization layer attenuates transmitted waves and eventually becomes impenetrable [60]. The surface impedance can be approximated as

$$Z_S = \frac{1+j}{\sigma\delta}, \quad \delta = \sqrt{\frac{2}{\omega\mu\sigma}} \tag{4.2}$$

where Z_S is also called the intrinsic impedance for a good conductor. When the thickness t of the metal layer is much smaller than the skin depth δ, the IBC model becomes inappropriate. Thus, Konno [64] replaced the characteristic impedance Z_m by the surface impedance Z_S and used it in cascaded transmission line model (4.1) with $\gamma_c = (1+j)/\delta$.

Another widely used approximation is called the electrically resistive sheet (R-card) or thin dielectric sheet. For a good conductor, it has the formulation as [60], [65]

$$R_{SH} = \frac{1}{\sigma t}, \quad t << \delta. \tag{4.3}$$

For a thin film conductor with high conductivity and small t, this sheet resistance is equivalent to a shunt resistance in the cascaded of transmission line model [61], [65].

However, above IBC and sheet resistance models neglect the dependency of the surface impedance on the TE/TM modes of hybrid EM fields inside conductor. Considering this, Amari et $al.$ [62] represented a TE/TM-mode sheet impedance model

$$Z_{SH,i}^{TE/TM} = Z_S \frac{Z_{L,i-1}^{TE/TM} + Z_S \tanh(\gamma_c t)}{Z_{L,i-1}^{TE/TM} \tanh(\gamma_c t) + Z_S [1 - 1/\cosh(\gamma_c t)]} \tag{4.4}$$

where $Z_{L,i-1}^{TE/TM}$ and γ_c are defined as same as (4.1). $Z_{SH,i}^{TE/TM}$ is derived as the tangential electric field over current density ($E_{\tan}/J$). When t goes to zero, $Z_{SH}^{TE/TM}$ converges to the R_{SH} and becomes a shunt impedance. When t becomes very large, $Z_{SH}^{TE/TM}$ converges to the surface impedance Z_S [62].

4.1.2   Model Comparison for the Dispersion of multilayered Microstrip

In this section, previously mentioned models are first compared on the basis of a simple two-layered planar structure as shown in Fig. 4.2. The structure consists of a thin conductive slab with a thickness t. Its conductivity σ is equal to 5.88×10^7 S/m. The slab is backed by the infinite free space. The equivalent input impedances, Z_{in}, are calculated at 10 GHz by using the transmission line formula (4.1), IBC (4.2), R-card (4.3), and TE/TM-mode sheet impedance (4.4), respectively.

The characteristics of the input impedance versus the slab thickness are investigated. Figs. 4.2 and 4.3 show input impedances for both TE and TM modes as functions of thickness t. The real and imaginary parts of the impedance are plotted separately. The thickness of metal slab t is normalized by the skin depth as t/δ, while the impedance is normalized by the surface resistance $R_S (= 1/(\sigma\delta))$. A medium value of γ_c is adopted by setting $\alpha^2 + \gamma_z^2 = 10\omega^2\varepsilon_0\mu_0$ in (4.1). The surface resistance R_S is directly related to Z_S. Thus, in Figs. 4.2 and 4.3, the impedances of the exact immitance approach and the TE/TM-mode sheet impedance model converge to the IBC surface impedance Z_S when t becomes about 2δ to 3δ.

The R-card model only agrees with others when t is rather small. For the real part of impedance, the R-card model requires that t is at least less than one skin depth; for the imaginary part of impedance, it requests that t is less than one tenth of the skin depth. Otherwise the R-card model diverges significantly. When t increases, the input impedance Z_{in} of R-card model goes to zero, hence the thin conductive slab can be regarded as a PEC. This phenomenon is related to the fact that the resistive sheet is modeled as a shunt resistance with the free-space impedance. As the thickness t increases, $R_{SH} (= 1/(\sigma t))$ becomes small enough to be dominant for the equivalent Z_{in}. Thus, physically, the R-card model tends to
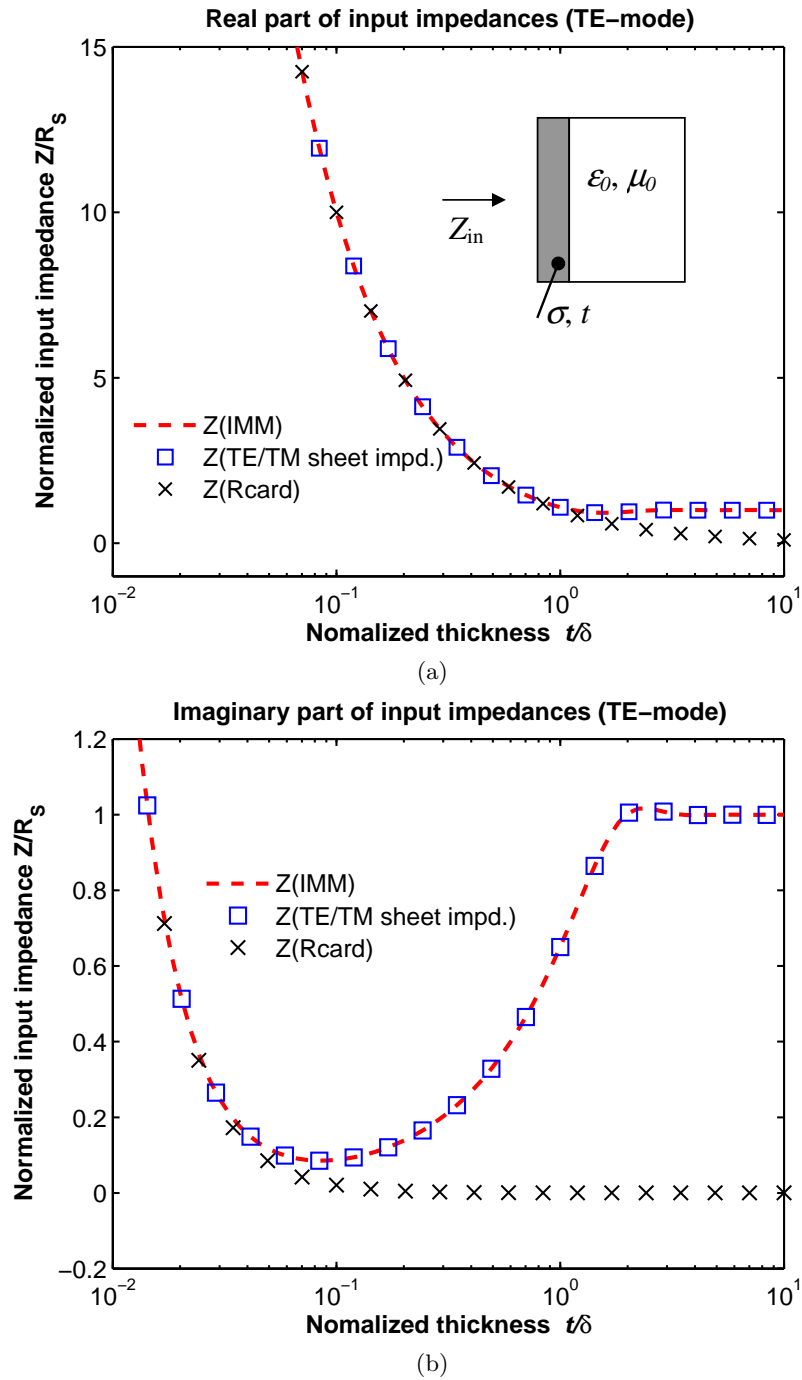
Figure 4.2: TE-mode equivalent input impedance Z_{in} as the function of t/δ (Z_{in} is normalized by the surface resistance $R_S = 1/(\sigma\delta)$.), models: $Z(\text{IMM})$ (exact immitance approach) (4.1), $Z(\text{R-card})$ (4.3), $Z(\text{TE-mode sheet impedance})$ (4.4), conductive slab σ: $5.88 \times 10^7\,\text{S/m}$, f: $10\,\text{GHz}$, $\alpha^2 + \gamma_z^2 = 10\omega^2\varepsilon_0\mu_0$: (a) real parts, (b) imaginary parts.
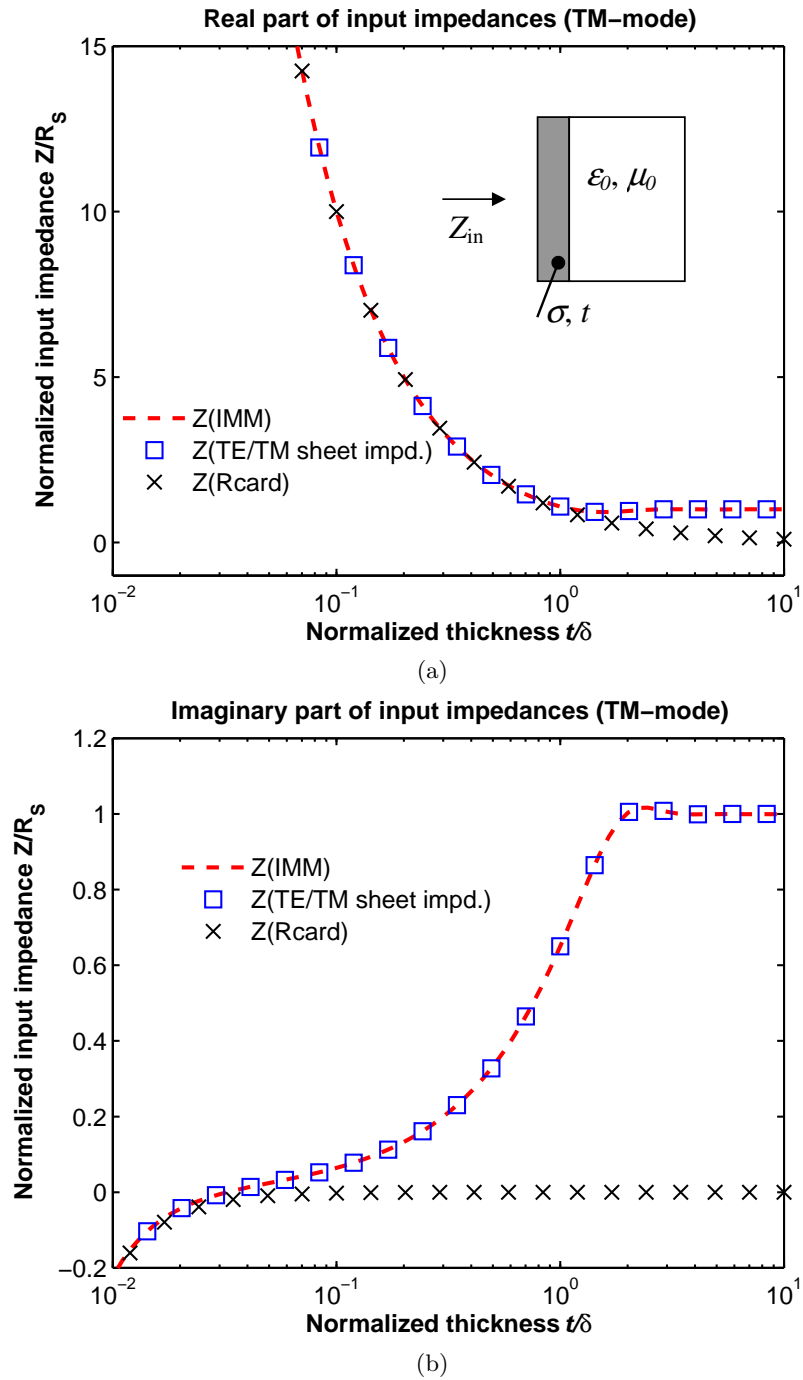
Figure 4.3: TM-mode equivalent input impedance Z_{in} normalized by R_S as function of t/δ with same parameters in Fig. 4.2, models: $Z(\text{IMM})$ (exact immitance approach) (4.1), $Z(\text{R-card})$ (4.3), $Z(\text{TM-mode sheet impedance})$ (4.4): (a) real parts, (b) imaginary parts.

make the equivalent impedance be a PEC when the thickness t is relatively large. But under this condition, the skin depth δ is on the same order with t, which violates the assumption that t is negligible. As a result, the R-card model will break down.

Next, previous models are implemented into a more complicated transmission line structure to study their validity on the overall electrical performance. This structure is actually a MIMI transmission line with a thin metallization ground inserted as illustrated in Fig. 4.4(b).

The effective permittivity $\varepsilon_{r\text{eff}}$ and attenuation constant as functions of frequency are plotted in Figs. 4.4(a) and 4.4(b). In Fig. 4.4(a), all models describe the slow-wave phenomena (high effective permittivity and small phase velocity) at low frequencies. At high frequencies the dominant mode is the quasi-TEM mode. The curves of immitance approach and TE/TM-mode sheet impedance model converge into the dashed line that represents the IBC or infinite-thickness metal BC. In these conditions, the metallization layer becomes completely opaque to block EM fields from reaching lower substrates. In addition, with frequency increasing, all curves approach the lowest dot line that stands for the situation when the thin metallization layer is modeled as a PEC ($\sigma = \infty$) and the microstrip line becomes lossless.

Moreover, when being compared with the exact immitance model, the IBC is appropriate for the $\varepsilon_{r\text{eff}}$ merely when the metal ground layer is much thicker than at least 2δ. Similarly, the TE/TM-mode sheet impedance is also more accurate at higher frequencies than lower ones. On the contrary, the R-card model behaves very close to the TE/TM-mode sheet impedance model at lower frequencies. But it differs from others in the high frequency region where the R-card converges to the lowest PEC boundary faster than others. This is due to the tendency of the R-card model to degrade the equivalent impedance into a PEC as discussed before in Figs. 4.2 and 4.3. Fig. 4.4(b) shows the attenuation changes as a function of frequency. When the thickness t is equal to the relevant skin depth δ, the curves of the IBC and immitance approach merge together. At the low frequency region, the attenuation is proportional to the square of the frequency, which is also predicted by the parallel-plate waveguide model in Chapter 2. In addition, if compared with the R-card model, the TE/TM-mode sheet impedance model shows a better agreement with the exact result at higher frequencies.
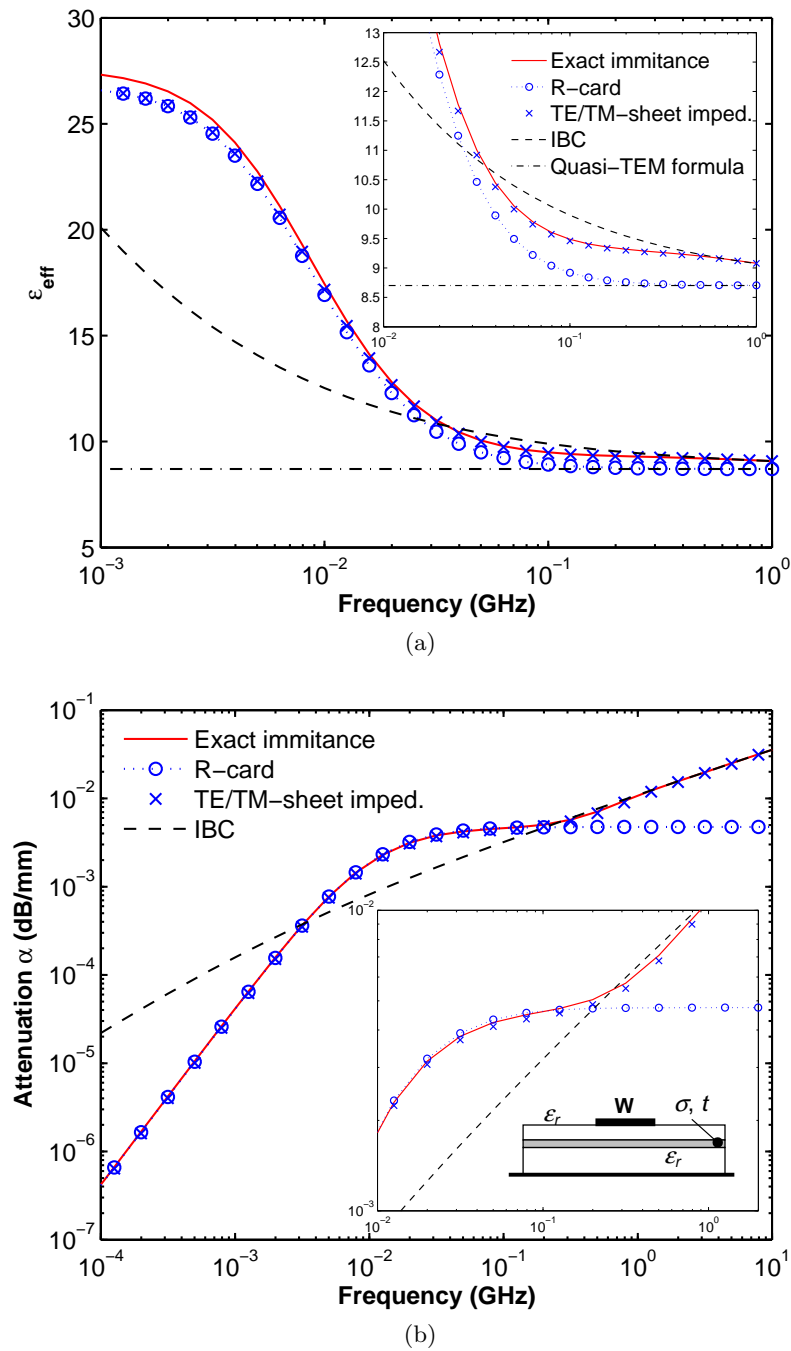
Figure 4.4: Dispersive characteristics for a MIMI microstrip using different models for finite metallization, lower dielectric: $80\,\mu$m, ε_r: 10.2, upper dielectric: 20 μm, ε_r: 10.2, w: $200\,\mu$m, metal layer thickness: $5\,\mu$m, σ: 5.8×10^7 S/m: (a) effective relative permittivity, (b) attenuation constant per unit length.
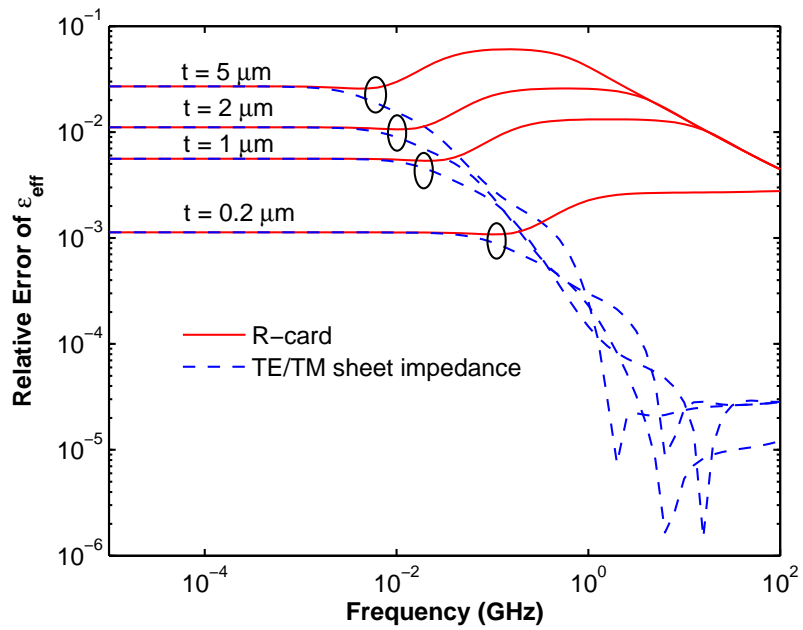
(a)
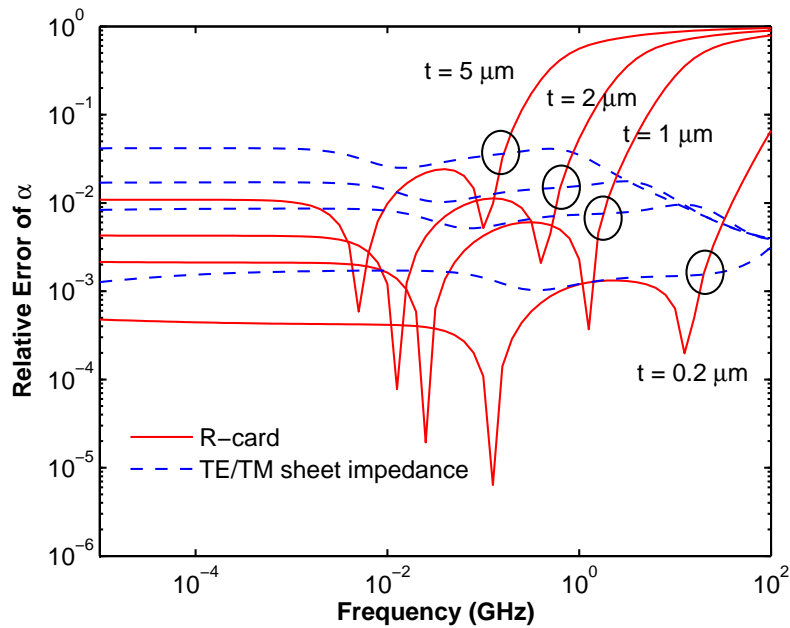
(b)

Figure 4.5: Relative errors for the R-card and TE/EM-mode sheet impedance as functions of frequency and thickness t for the same MIMI structure in Fig. 4.4: (a) errors of effective permittivity, (b) errors of attenuation constant.

Finally, the relative accuracy of the R-card model and TE/TM-mode sheet impedance model is compared. Fig. 4.5 illustrates how the relative errors of effective permittivity and attenuation vary with the frequency and thickness t. The result of the immitance approach is used as exact solution. Both Figs. 4.5(a) and 4.5(b) show that the thinner the ground layer, the better the accuracy. But one pronounced phenomenon is that, for a fixed thickness t, the relative errors of the permittivity and attenuation do not decrease but are almost constant as frequency drops. Furthermore, for the attenuation, the TE/TM-mode sheet impedance model shows better accuracy at higher frequencies, whereas the R-card model has less error at the lower frequencies. In the transition region, the error of the R-card model increases and becomes even worse. The reason is that the R-card model overdoes the equivalent PEC approximation. This means that the two models still have noticeable errors even when t is negligible compared to the skin depth. This invalidation comes from the violation of model assumptions. The R-card model was proposed originally to the EM scattering problems with thin conductive film when the tangential incident electric field is dominant. The TE/TM-mode sheet impedance, similarly, is derived as the definition of the tangential electric field over current density. So the normal component of polarization current is regarded to be insignificant inside of the sheet [66]. However, such assumptions are not very suitable for the multilayered microstrip lines. For the quasi-TEM approximation, the normal component of the electric field (E_y) is too dominant to be ignored. On the whole, Fig. 4.5 shows that the R-card cannot maintain a constant error over a broad frequency range, while the TE/TM-mode sheet impedance model poses a modestly improved accuracy with frequency increasing.

4.2 Modeling of the Metal Signal Strip With Finite Thickness

The effect of signal strips with finite thickness and conductivity is an important factor that affects the propagation characteristics of transmission lines. This topic has attracted intensive research efforts. The full-wave analysis has been carried out by several techniques like the mode matching method, FEM, and MoL, etc. The integral-equation-based approaches are also versatile for this purpose. Although the original SDA is limited to the infinitesimal

PEC BCs. Many following works have extended the SDA to analyze the lossy transmission lines with finite-thickness signal strips. In [67], a two-level model was used to approximate the moderately thick conductors on the top and bottom surfaces with two PEC BCs. A N-layer model was applied to evaluate the conductor loss [68]. With the concept of surface impedances, several modified SDAs were proposed for microstrip lines with finite metallization thickness and conductivity in [53], [69]-[73]. A complex resistive boundary condition was applied to solve for the thin superconducting strip lines [69]. Liou and Lau [72] found the surface impedance works as the internal impedance of the driving current element in the equivalent transmission line circuits. In [73], a two-plate quasi-TEM surface impedance model was used in the spectral domain. Similar two-port models were also widely used in [50], [53], [74], and [75]. In [76], all three components of strip currents were considered in the modified SDA. The rigorous integral-equation formulation with dyadic Green's function was proposed for the skin effect of conductor strips [77]. A generalized transverse-resonance-diffraction approach was developed for the modeling of planar structures with thick lossy conductors [78].

In the following sections, the basic concept of the modified spectral domain approach will be introduced with several approximate models for the surface impedances. Numerical tests for a MIS transmission line structure will be carried out in the end.

4.2.1 The Modified Green's Functions

As introduced in Chapter 3, the dyadic spectral-domain Green's functions describe the relationship between the interface field $\widetilde{\mathbf{E}}$ and surface current $\widetilde{\mathbf{J}}_{\mathbf{s}}$ as [70]

$$\widetilde{\mathbf{E}} = \widetilde{\bar{\bar{\mathbf{G}}}}\widetilde{\mathbf{J}}_{\mathbf{s}}. \tag{4.5}$$

where $\widetilde{\bar{\bar{\mathbf{G}}}}$ is the matrix form of dyadic spectral-domain Green's functions in (3.36). When the conductors in transmission lines are modeled as PECs, there exist no tangential electric fields on conductors, whereas the currents only have finite values instead. The homogenous equation (3.65) with a zero right hand side can be obtained by the Galerkin's method. However, for the imperfect conductors, tangential electric fields are nonzero on the conductor surfaces. Now the

electric field on the interface can be divided into two parts as a linear superposition

$$\widetilde{\mathbf{E}} = \widetilde{\mathbf{E}}_{\mathbf{c}} + \widetilde{\mathbf{E}}_{\mathbf{d}} \qquad (4.6)$$

where $\widetilde{\mathbf{E}}_{\mathbf{c}}$ is the Fourier transform of the interface field on conductor surfaces, while $\widetilde{\mathbf{E}}_{\mathbf{d}}$ is the Fourier transform of the field outside the conductors. Because the equivalent magnetic current is negligible for good conductors [79], the relationship between $\widetilde{\mathbf{E}}_{\mathbf{c}}$ and $\widetilde{\mathbf{J}}_{\mathbf{s}}$ on the isotropic imperfect conductors can be described by a surface-typed impedance $\widetilde{Z}_s$ (Ω)

$$\widetilde{\mathbf{E}}_{\mathbf{c}} = \widetilde{Z}_s \widetilde{\mathbf{J}}_{\mathbf{s}}. \qquad (4.7)$$

For perfect conductors, the $Z_s = 0$. By expressing $\widetilde{\mathbf{E}}_{\mathbf{c}}$ in the form of $\widetilde{\mathbf{J}}_{\mathbf{s}}$, the new Green's functions become

$$\widetilde{\mathbf{E}}_{\mathbf{d}} = \left(\bar{\bar{\widetilde{\mathbf{G}}}} - \widetilde{Z}_s \mathbf{I} \right) \widetilde{\mathbf{J}}_{\mathbf{s}} \qquad (4.8)$$

where $\mathbf{I}$ is an identity matrix. It is apparent that the currents $\widetilde{\mathbf{J}}_{\mathbf{s}}$ has a complementary distribution with the electric field $\widetilde{\mathbf{E}}_{\mathbf{d}}$ in the spatial domain. So by applying the Galerkin's method with the Parseval's theorem, above integral equation is changed into a homogeneous system like (3.65). Thus the modified Green's functions have diagonal terms that relate to the surface impedance as

$$\left(\bar{\bar{\widetilde{\mathbf{G}}}} - \widetilde{Z}_s \mathbf{I} \right) = \begin{bmatrix} \widetilde{G}_{xx}(\alpha, \gamma_z) - \widetilde{Z}_s & \widetilde{G}_{xz}(\alpha, \gamma_z) \\ \widetilde{G}_{zx}(\alpha, \gamma_z) & \widetilde{G}_{zz}(\alpha, \gamma_z) - \widetilde{Z}_s \end{bmatrix}. \qquad (4.9)$$

This modified Green's functions can be regarded as a perturbation from (3.36).

4.2.2 Models for the Surface-Typed Impedances

For the surface-typed impedance of finite metallization strips, the models for the thin metal ground in Section 4.1 are also applicable. For example, when strips are thick, the surface impedance (4.2) for IBC can be used, while the sheet resistance (R-card) model in (4.3) is suitable for very thin strips. The surface impedance using the transmission line model in (4.1) is appropriate too. In addition, Krowne [74] proposed another approximate surface impedance

by weighting the field components in the two-port models

$$\widetilde{Z}_s = \frac{1}{\sigma t} \frac{\frac{(1+j)t}{\delta}}{\tanh\left[\frac{(1+j)t}{\delta}\right]}. \tag{4.10}$$

4.2.3 Numerical Simulation Results

In this section, a MIS structure with finite metallization for signal strip is simulated using different models mentioned previously. The structure consists of a $250\,\mu$m silicon substrate with $\sigma = 5\,\text{S/m}$ and $\varepsilon_r = 12$. The thin silicon dioxide layer has a thickness of $1\,\mu$m and $\varepsilon_r = 4$. The signal strip is $160\,\mu$m wide and $1\,\mu$m thick. Its conductivity is equal to $5.88\times10^7\,\text{S/m}$. The models of the R-card, IBC, transmission line, and Krowne's formula (4.10) are implemented. The results are illustrated in Fig. 4.6. No big differences between the models of R-card, transmission line and Krowne's formula can be observed because the signal strip is very thin to make these models identical to each other. As the results of the parallel-plate waveguide model in Fig. 2.6, the effective permittivity becomes large when the frequency goes down. This is attributed to the highly lossy signal strips. Fig. 4.6 also shows there is no clear slow-wave regions when considering the loss from signal strips.

The influence of the strip metallization thickness is shown in Fig. 4.7. Only the transmission line model in (4.1) is adopted. The figure shows that, due to the series resistance, all nonzero-thickness losses are larger than the zero-thickness case. And the thinner the strip is, the higher the loss becomes. Compared with the effect of thin metallization ground in Fig. 2.5, finite thickness signal strips do not enhance slow-wave mode but have remarkable influence on the attenuation instead.

4.3 Conclusions

To study the metallization ground layer and signal strip in the multilayered structure, different models for the thin-film conductor are compared and implemented to analyze a MIMI structure and a MIS structure. The rigorous spectral domain approach is used. For the models of thin metallization ground, numerical results show that the IBC is applicable when the thickness t is larger than 2δ. At low frequencies and fixed thickness, the errors of the
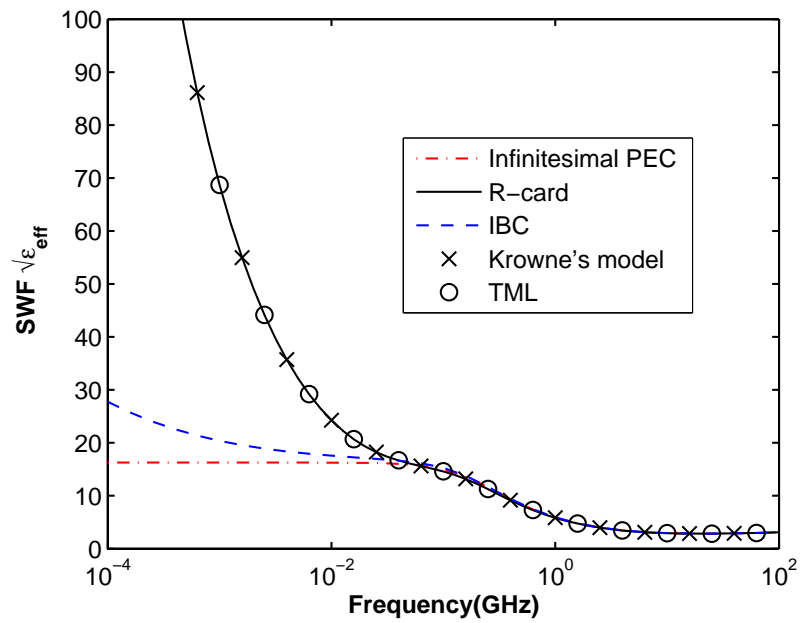
(a)
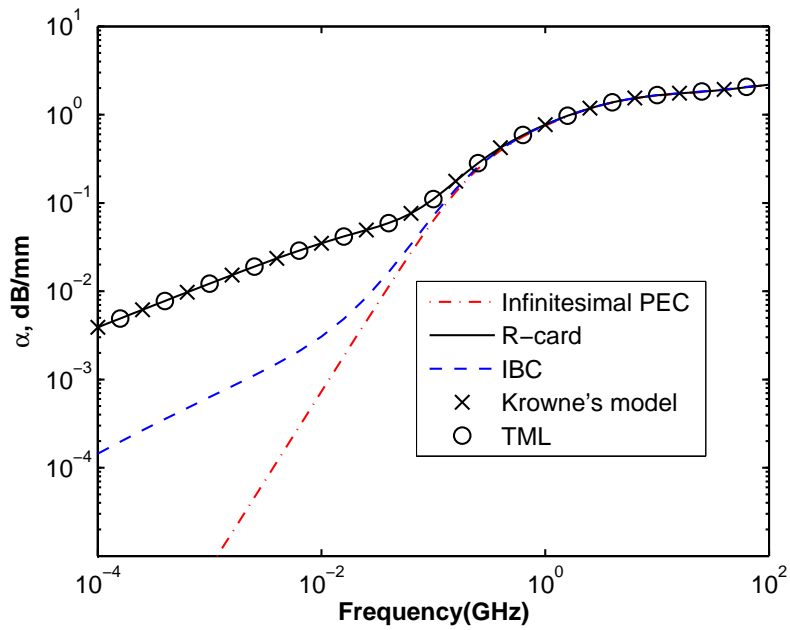
(b)

Figure 4.6: Dispersive characteristics for a MIS structure using different models for the signal strip, silicon: $250\,\mu$m, ε_r: 12, σ: $5\,$S/m, silicon dioxide: $1\,\mu$m, ε_r: 4, w: $160\,\mu$m, signal metallization: $1\,\mu$m, σ: $5.8{\times}10^7\,$S/m: (a) effective relative permittivity, (b) attenuation constant.
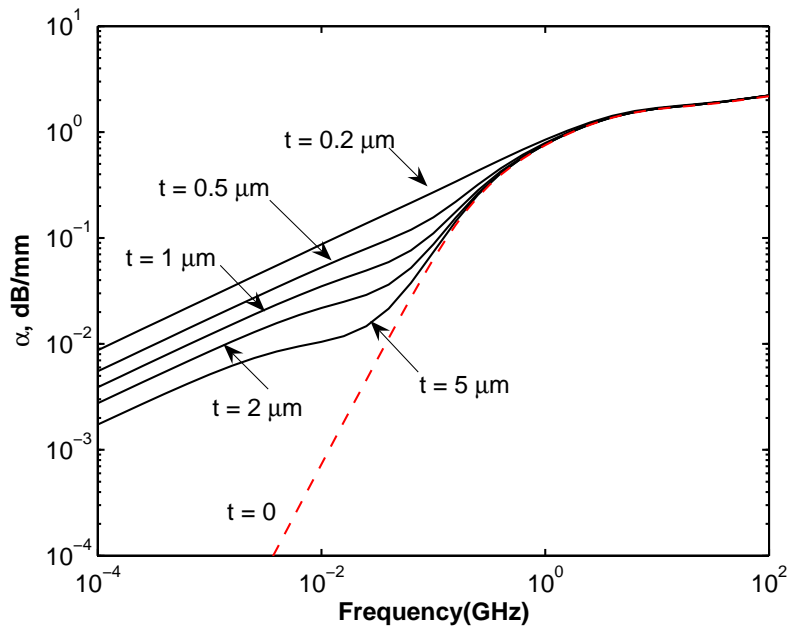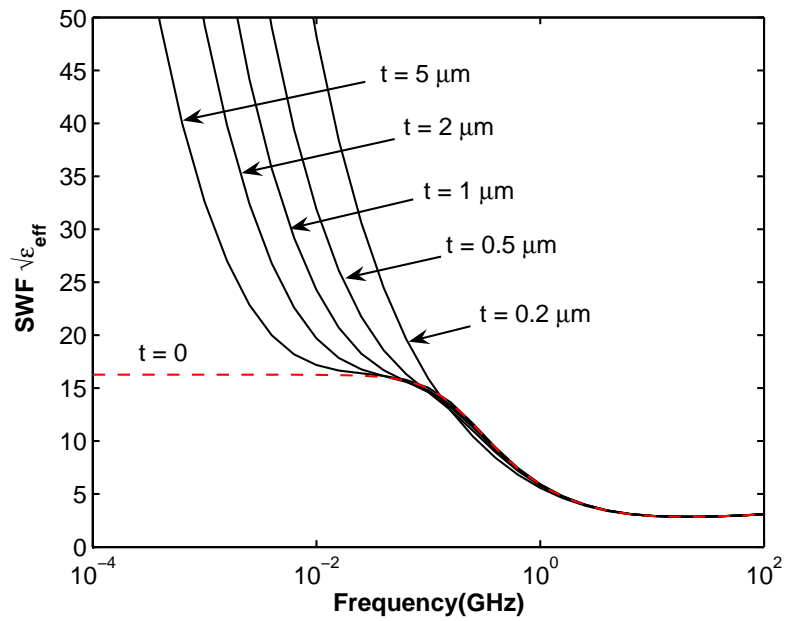
Figure 4.7: Dispersive characteristics for a MIS structure as functions of thickness using the transmission line model for the signal strip (basic parameters as in Fig. 4.6): (a) effective relative permittivity, (b) attenuation constant per unit length.

R-card and TE/TM-mode sheet impedance are almost constant due to ignoring the normal components of the electric field. The performance of the R-card at higher frequencies becomes rather unacceptable, which suggests it is not appropriate to implement the R-card to model the thin metal ground in multilayered microstrip transmission lines. For the models of signal strips, the results show that the influences from finite thin signal strips are different with the ones from the thin metal ground.

CHAPTER 5.   THE MODELING OF PLANAR TRANSMISSION LINES IN MULTILAYERED STRUCTURE

To analyze a transmission line or interconnect, one task is to evaluate its complete properties like the propagation constant, loss per unit length, field distribution, characteristic impedance, and transient response, etc. In Chapter 3, the electric-field integral equations are formulated based on the multilayered Green's functions. The propagation constant of transmission lines is solved by the MoM as the eigenvalue of system. With calculated complex propagation constants, the current distribution on conductors and other transmission line properties can be further computed.

This chapter exhibits a complete spectrum for analyzing the multilayered transmission lines. Section 5.1 shows the way to extract the effective relative permittivity and loss per unit length from the complex propagation constant. With these two parameters, the transient responds can be evaluated in the time domain in Section 5.2. Furthermore, in Sections 5.3 and 5.4, formulations for the spatial distribution of EM fields are derived explicitly, from which the characteristic impedance and RLCG circuit parameters can be extracted. Finally, Section 5.5 discusses the numerical issues such as finding complex roots and evaluating infinite integrals. The convergence of the Galerkin's method is also discussed.

5.1   Dispersion and Loss Analysis

As mentioned in Chapter 3, a lossy transmission line has a longitudinal propagation constant with the factor $e^{j\omega t}e^{-j\gamma_z z}$. Here γ_z is the eigenvalue or mode for the guided-wave system. For a lossy system, after finding the complex $\gamma_z(\omega)$, we can write it into the real and imaginary

parts as

$$j\gamma_z = \alpha + j\beta, \quad (\alpha, \beta > 0) \tag{5.1}$$

where α is called the attenuation constant and β is the phase constant.[1] Based on this definition, the corresponding real effective permittivity ($\varepsilon_{r\text{eff}}$), loss/attenuation per unit length (α), slow-wave factor (SWF), and normalized wavelength (λ_g/λ_0) can be calculate as

$$\varepsilon_{r\text{eff}} = \left(\frac{\beta}{k_0}\right)^2 = \left[\text{Re}\left(\frac{\gamma_z}{k_0}\right)\right]^2 \tag{5.2}$$

$$\alpha = -\text{Im}(\gamma_z) \quad (\text{Nepers/m})$$

$$= -8.686\,\text{Im}(\gamma_z) \quad (\text{dB/m}) \tag{5.3}$$

$$\text{SWF} = \sqrt{\varepsilon_{r\text{eff}}} \tag{5.4}$$

$$\frac{\lambda_g}{\lambda_0} = \frac{1}{\sqrt{\varepsilon_{r\text{eff}}}} \tag{5.5}$$

where $k_0^2 = \omega^2 \varepsilon_0 \mu_0$. λ_g ($= 2\pi/\beta$) and λ_0 ($= 2\pi/k_0$) are the propagation wavelengths in transmission line and free space, respectively. Because all parameters above are frequency dependent, the dispersive characteristics of transmission lines are directly related with $\gamma_z(\omega)$.

5.2 Transient Analysis

With the dispersive propagation constant γ_z, we can get the transient response of pulse signals by the Fourier transformation between the time domain and frequency domain. The time harmonic field is assumed to vary in time as $e^{j\omega t}$. First, the transient signals, e.g. the Gaussian or rectangular pulses, are decomposed into different harmonic components in the frequency domain. After γ_z is calculated at certain frequency point, which is also equivalent to the system frequency response to the corresponding harmonic, distorted output waveforms can be calculated. To obtain the output wave after traveling a distance L away along the z direction, the inverse Fourier transform is applied as [80]

$$v_{\text{out}}(t, z = L) = \frac{1}{2\pi} \int_{-\infty}^{\infty} \widetilde{V}_{\text{in}}(\omega, z = 0) e^{j\omega t - j\gamma_z L} d\omega \tag{5.6}$$

---

[1]Here α is not the spectral-domain variable as defined before.

where $\widetilde{V}_{\text{in}}$ is the input waveform in frequency domain at $z = 0$,

$$\widetilde{V}_{\text{in}}(\omega, z = 0) = \int_{-\infty}^{\infty} v_{\text{in}}(t, z = 0)e^{-j\omega t}dt \qquad (5.7)$$

and v_{in} is the input signal in time domain. v_{out} is the output signal after propagating along the transmission line. In the numerical computation, above inverse Fourier transform can be evaluated by the fast Fourier transform (FFT) algorithm efficiently. For the FFT, the sampling interval in time domain Δt decides the Nyquist critical frequency $f_N = 1/(2\Delta t)$, while the sampling interval in frequency domain Δf determines the duration of the total time series $T_0 = 1/\Delta f$. The most common choice of excitation waveform is a modulated Gaussian pulse

$$v_g(t) = \cos(2\pi f_c t)e^{-\frac{(t-t_p)^2}{2\tau^2}} \qquad (5.8)$$

where f_c is the center frequency. t_p is the pulse time offset, and τ is related to the pulse width. In addition, to simulate transient signals in digital systems, the rectangular pulse is widely used. A rectangular pulse is defined by the width of the pulse t_w, its rise time t_r, and fall time t_f as illustrated in Fig. 5.1.
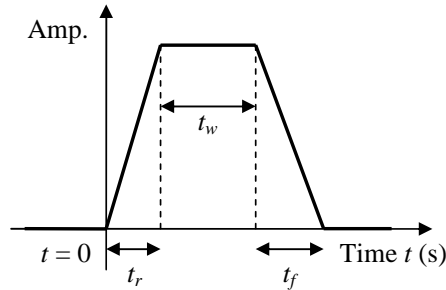
Figure 5.1: Parameters of a rectangular pulse in time domain.

5.3   The Electric and Magnetic Field Distributions

After finding the propagation constant γ_z and certain current bases, all field components can be evaluated systematically from the electric and magnetic potentials. The procedures are introduced in the following steps.

5.3.1 Coefficients of Current Basis Functions

By substituting the known γ_z into the matrix $[K(\gamma_z)]$ of (3.65), the coefficients of a_m and b_n are found as the eigenvector that is corresponding to the zero eigenvalue. Then the currents $\widetilde{J}_z$ and $\widetilde{J}_x$ are determined by (3.53). Then the coefficients $\widetilde{A}$, $\widetilde{B}$, $\widetilde{C}$, and $\widetilde{D}$ are found from (3.35) as

$$
\begin{bmatrix} \widetilde{A} \\ \widetilde{C} \\ \widetilde{B} \\ \widetilde{D} \end{bmatrix} = \begin{bmatrix} e^{-\sum\limits_{i=2}^{t} \gamma_i \Delta h_i} & & & \\ & e^{-\sum\limits_{i=2}^{t} \gamma_i \Delta h_i} & & \\ & & e^{-\sum\limits_{j=t+1}^{N-1} \gamma_j \Delta h_j} & \\ & & & e^{-\sum\limits_{j=t+1}^{N-1} \gamma_j \Delta h_j} \end{bmatrix} \begin{bmatrix} V \end{bmatrix} \begin{bmatrix} 0 \\ j\gamma_z \sum\limits_{m=1}^{M} a_m \widetilde{J}_{x,m} \\ 0 \\ \sum\limits_{n=1}^{N} b_n \widetilde{J}_{z,n} \end{bmatrix} \quad (5.9)
$$

where $\gamma_i^2 = \alpha^2 + \gamma_z^2 - \omega^2 \varepsilon_i \mu_i$. Therefore, coefficients and corresponding potentials in the first $(i = 1)$ and last $(i = N)$ layers are determined. Next, the A_i, B_i, C_i, and D_i coefficients of the ith layer can be obtained from the cascaded transfer matrices like (3.26) and (3.30) in the following procedures

$$
\begin{bmatrix} A_i \\ B_i \\ C_i \\ D_i \end{bmatrix} = \begin{bmatrix} M_{i,i-1} \end{bmatrix} \begin{bmatrix} M_{i-1,i-2} \end{bmatrix} \cdots \begin{bmatrix} \widetilde{A} \\ 0 \\ \widetilde{C} \\ 0 \end{bmatrix}, \quad 2 \le i \le t \quad (5.10)
$$

$$
\begin{bmatrix} A_i \\ B_i \\ C_i \\ D_i \end{bmatrix} = \begin{bmatrix} M'_{i,i+1} \end{bmatrix} \begin{bmatrix} M'_{i+1,i+2} \end{bmatrix} \cdots \begin{bmatrix} 0 \\ \widetilde{B} \\ 0 \\ \widetilde{D} \end{bmatrix}, \quad t+1 \le i \le N-1. \quad (5.11)
$$

5.3.2 Potential Functions in Each Layer

With the A_i, B_i, C_i, and D_i coefficients determined, according to (3.20) and (3.27), the electric and magnetic potentials of the ith layer can be expressed as the general forms

$$
\begin{aligned}
\widetilde{\Psi}_{e,i} &= A_i e^{\gamma_i(y-h_\square)} + B_i e^{-\gamma_i(y-h_\square)} \\
\widetilde{\Psi}_{m,i} &= C_i e^{\gamma_i(y-h_\square)} + D_i e^{-\gamma_i(y-h_\square)}
\end{aligned} \quad (5.12)
$$

where $h_\square = h_{i-1}$ for $2 \leq i \leq t$ and $h_\square = h_i$ for $t+1 \leq i \leq N-1$. Two special cases need to be considered: for the first layer, $h_\square = h_1$; for the last layer, $h_\square = h_N - 1$. The details can be referred to Appendix B.

5.3.3 Field Components in the Spectral Domain

Derived from the equations of (3.9)-(3.12), the spectral-domain electric and magnetic field components in the ith layer are given as follows

$$
\begin{aligned}
\widetilde{E}_{z,i} &= j\frac{k_i^2-\gamma_z^2}{\gamma_z}\left[A_i e^{\gamma_i(y-h_\square)} + B_i e^{-\gamma_i(y-h_\square)}\right] \\
\widetilde{E}_{x,i} &= -j\alpha\left[A_i e^{\gamma_i(y-h_\square)} + B_i e^{-\gamma_i(y-h_\square)}\right] + \frac{\omega\mu_i\gamma_i}{\gamma_z}\left[C_i e^{\gamma_i(y-h_\square)} - D_i e^{-\gamma_i(y-h_\square)}\right] \quad (5.13) \\
\widetilde{E}_{y,i} &= \gamma_i\left[A_i e^{\gamma_i(y-h_\square)} - B_i e^{-\gamma_i(y-h_\square)}\right] + j\frac{\omega\mu_i\alpha}{\gamma_z}\left[C_i e^{\gamma_i(y-h_\square)} + D_i e^{-\gamma_i(y-h_\square)}\right]
\end{aligned}
$$

and

$$
\begin{aligned}
\widetilde{H}_{z,i} &= j\frac{k_i^2-\gamma_z^2}{\gamma_z}\left[C_i e^{\gamma_i(y-h_\square)} + D_i e^{-\gamma_i(y-h_\square)}\right] \\
\widetilde{H}_{x,i} &= -j\alpha\left[C_i e^{\gamma_i(y-h_\square)} + D_i e^{-\gamma_i(y-h_\square)}\right] - \frac{\omega\varepsilon_i\gamma_i}{\gamma_z}\left[A_i e^{\gamma_i(y-h_\square)} - B_i e^{-\gamma_i(y-h_\square)}\right] \quad (5.14) \\
\widetilde{H}_{y,i} &= \gamma_i\left[C_i e^{\gamma_i(y-h_\square)} - D_i e^{-\gamma_i(y-h_\square)}\right] - j\frac{\omega\varepsilon_i\alpha}{\gamma_z}\left[A_i e^{\gamma_i(y-h_\square)} + B_i e^{-\gamma_i(y-h_\square)}\right]
\end{aligned}
$$

where all parameters follow the same definitions as before.

5.3.4 Field Components in the Spatial Domain

Finally, the corresponding spatial field distribution on the point (x_0, y_0, z_0) can be evaluated by the inverse Fourier transformation of (5.13) and (5.14)

$$
\mathbf{E}(x_0, y_0, z_0) = \frac{e^{-j\gamma_z z_0}}{2\pi}\int_{-\infty}^{\infty}\widetilde{\mathbf{E}}(\alpha, y_0)e^{-j\alpha x_0}d\alpha \tag{5.15}
$$

$$
\mathbf{H}(x_0, y_0, z_0) = \frac{e^{-j\gamma_z z_0}}{2\pi}\int_{-\infty}^{\infty}\widetilde{\mathbf{H}}(\alpha, y_0)e^{-j\alpha x_0}d\alpha \tag{5.16}
$$

where $\mathbf{E}$ and $\mathbf{H}$ are vector forms of the electric and magnetic fields, respectively.

5.4 The Characteristic Impedance

The characteristic impedances of microstrip lines can be estimated based on the field distribution over the whole cross section. Generally speaking, there are three definitions for the

impedance: the power-current impedance (Z_{PI}), the power-voltage impedance (Z_{PV}), and the voltage-current impedance (Z_{VI}) [48]. These three types of impedances are reviewed as follows.

5.4.1 Power-Current Definition

This definition is widely used in the literature with an expression as

$$Z_{PI} = \frac{2P}{|I_z|^2} \tag{5.17}$$

where P is the total power flowing through the cross section of transmission line; I_z is the total longitudinal current along the z axis. The power P is calculated by integrating the z component of the complex Poynting vector $\frac{1}{2}\mathbf{E} \times \mathbf{H}^*$ over the whole xoy plane. In addition, the spatial-domain integral for multilayered structures can be transferred to the spectral domain according to the Plancherel's theorem

$$P = \frac{1}{2} \int_0^\infty \int_{-\infty}^\infty \mathbf{E} \times \mathbf{H}^* \cdot \hat{z} dx dy = \frac{1}{4\pi} \int_{-\infty}^\infty \sum_{i=1}^N \int_{h_{i-1}}^{h_i} (\widetilde{E}_{x,i}\widetilde{H}_{y,i}^* - \widetilde{E}_{y,i}\widetilde{H}_{x,i}^*) dy d\alpha \tag{5.18}$$

where $*$ stands for the operator of complex conjugate. To fulfill the integral in the spectral domain, field distributions in (5.13) and (5.14) are expressed by new defined coefficients as follows

$$
\begin{aligned}
\widetilde{E}_{x,i} &= \left[-j\alpha A_i + \frac{\omega\mu_i\gamma_i}{\gamma_z}C_i\right]e^{\gamma_i(y-h_\square)} + \left[-j\alpha B_i - \frac{\omega\mu_i\gamma_i}{\gamma_z}D_i\right]e^{-\gamma_i(y-h_\square)} \\
&\equiv \bar{A}_{x,i}e^{\gamma_i(y-h_\square)} + \bar{B}_{x,i}e^{-\gamma_i(y-h_\square)}
\end{aligned} \tag{5.19}
$$

$$
\begin{aligned}
\widetilde{E}_{y,i} &= \left[\gamma_i A_i + j\frac{\omega\mu_i\alpha}{\gamma_z}C_i\right]e^{\gamma_i(y-h_\square)} + \left[-\gamma B_i + j\frac{\omega\mu_i\alpha}{\gamma_z}D_i\right]e^{-\gamma_i(y-h_\square)} \\
&\equiv \bar{A}_{y,i}e^{\gamma_i(y-h_\square)} + \bar{B}_{y,i}e^{-\gamma_i(y-h_\square)}
\end{aligned} \tag{5.20}
$$

$$
\begin{aligned}
\widetilde{H}_{x,i} &= \left[-j\alpha C_i - \frac{\omega\varepsilon_i\gamma_i}{\gamma_z}A_i\right]e^{\gamma_i(y-h_\square)} + \left[-j\alpha D_i + \frac{\omega\varepsilon_i\gamma_i}{\gamma_z}B_i\right]e^{-\gamma_i(y-h_\square)} \\
&\equiv \bar{C}_{x,i}e^{\gamma_i(y-h_\square)} + \bar{D}_{x,i}e^{-\gamma_i(y-h_\square)}
\end{aligned} \tag{5.21}
$$

$$
\begin{aligned}
\widetilde{H}_{y,i} &= \left[\gamma_i C_i - j\frac{\omega\varepsilon_i\alpha}{\gamma_z}A_i\right]e^{\gamma_i(y-h_\square)} + \left[-\gamma D_i - j\frac{\omega\varepsilon_i\alpha}{\gamma_z}B_i\right]e^{-\gamma_i(y-h_\square)} \\
&\equiv \bar{C}_{y,i}e^{\gamma_i(y-h_\square)} + \bar{D}_{y,i}e^{-\gamma_i(y-h_\square)}
\end{aligned} \tag{5.22}
$$

where suffix i is the layer index. Therefore, above subregion-integral over y (5.18) becomes

$$\int_{h_{i-1}}^{h_i} \left(\widetilde{E}_{x,i}\widetilde{H}_{y,i}^* - \widetilde{E}_{y,i}\widetilde{H}_{x,i}^* \right) dy = \int_{h_{i-1}}^{h_i} \left(\bar{A}_{x,i}\bar{C}_{y,i}^* - \bar{A}_{y,i}\bar{C}_{x,i}^* \right) e^{2\text{Re}[\gamma_i(y-h_\square)]} dy$$

$$+ \int_{h_{i-1}}^{h_i} \left(\bar{A}_{x,i}\bar{D}_{y,i}^* - \bar{A}_{y,i}\bar{D}_{x,i}^* \right) e^{2\text{Im}[\gamma_i(y-h_\square)]} dy$$

$$+ \int_{h_{i-1}}^{h_i} \left(\bar{B}_{x,i}\bar{C}_{y,i}^* - \bar{B}_{y,i}\bar{C}_{x,i}^* \right) e^{-2\text{Im}[\gamma_i(y-h_\square)]} dy$$

$$+ \int_{h_{i-1}}^{h_i} \left(\bar{B}_{x,i}\bar{D}_{y,i}^* - \bar{B}_{y,i}\bar{D}_{x,i}^* \right) e^{-2\text{Re}[\gamma_i(y-h_\square)]} dy. \quad (5.23)$$

Disregarding the complex coefficients, these subregion-integrals of exponential functions yield the analytical results

$$\int_{h_{i-1}}^{hi} e^{\pm 2\text{Re}[\gamma_i(y-h_\square)]} dy = \begin{cases} \frac{e^{\pm 2\text{Re}[\gamma_i(h_i-h_{i-1})]}-1}{\pm 2\text{Re}(\gamma_i)}, & \text{lower: } h_\square = h_{i-1}, \ \text{Re}(\gamma_i) \neq 0 \\ \frac{1-e^{\mp 2\text{Re}[\gamma_i(h_i-h_{i-1})]}}{\pm 2\text{Re}(\gamma_i)}, & \text{upper: } h_\square = h_i, \ \text{Re}(\gamma_i) \neq 0 \\ h_i - h_{i-1}, & \text{Re}(\gamma_i) = 0 \end{cases} \quad (5.24)$$

$$\int_{h_{i-1}}^{hi} e^{\pm 2\text{Im}[\gamma_i(y-h_\square)]} dy = \begin{cases} \frac{e^{\pm 2\text{Im}[\gamma_i(h_i-h_{i-1})]}-1}{\pm 2\text{Im}(\gamma_i)}, & \text{lower: } h_\square = h_{i-1}, \ \text{Im}(\gamma_i) \neq 0 \\ \frac{1-e^{\mp 2\text{Im}[\gamma_i(h_i-h_{i-1})]}}{\pm 2\text{Im}(\gamma_i)}, & \text{upper: } h_\square = h_i, \ \text{Im}(\gamma_i) \neq 0 \\ h_i - h_{i-1}, & \text{Im}(\gamma_i) = 0 \end{cases} \quad (5.25)$$

where the upper and lower regions are defined by their position with respect to the location of signal strip. Specifically because $h_\square = h_1$ and $h_\square = h_{N-1}$, it is equivalent to treat the first layer as one case of upper region, while the last layer as one case of lower region. If the first or last layer has open BCs, the integral has much simpler analytical form. For example, for the last layer with open BCs, we have $A_N = C_N = 0$, and the power integral has a result as

$$\int_{h_{N-1}}^{\infty} \left(\widetilde{E}_{x,N}\widetilde{H}_{y,N}^* - \widetilde{E}_{y,N}\widetilde{H}_{x,N}^* \right) dy$$

$$= (\bar{B}_{x,N}\bar{D}_{y,N}^* - \bar{B}_{y,N}\bar{D}_{x,N}^*) \int_{h_{N-1}}^{\infty} e^{-2\text{Re}[\gamma_N(y-h_{N-1})]} dy$$

$$= \frac{\bar{B}_{x,N}\bar{D}_{y,N}^* - \bar{B}_{y,N}\bar{D}_{x,N}^*}{2\text{Re}(\gamma_N)} \quad (5.26)$$

where $\mathrm{Re}(\gamma_N) \neq 0$. Similarly, for the first layer, the open BC yields

$$
\int_{-\infty}^{h_1} \left(\widetilde{E}_{x,1} \widetilde{H}_{y,1}^* - \widetilde{E}_{y,1} \widetilde{H}_{x,1}^* \right) dy
$$
$$
= (\bar{A}_{x,1} \bar{C}_{y,1}^* - \bar{A}_{y,1} \bar{C}_{x,1}^*) \int_{-\infty}^{h_1} e^{2\mathrm{Re}[\gamma_1(y-h_1)]} dy = \frac{\bar{A}_{x,1} \bar{C}_{y,1}^* - \bar{A}_{y,1} \bar{C}_{x,1}^*}{2\mathrm{Re}(\gamma_1)} \tag{5.27}
$$

where $\mathrm{Re}(\gamma_1) \neq 0$. The total current I_z is calculated from the integral of the current density J_z over the signal strip shown in Fig. 3.1

$$
I_z = \int_{-w/2}^{w/2} J_z(x) dx. \tag{5.28}
$$

Then, the characteristic impedance of Z_{PI} is calculated directly from the definition.

5.4.2 Voltage-Current Definition

The voltage V of a multilayered single microstrip line can be calculated by integrating the E_y components along the y axis, from the center of signal strip down to the PEC boundary h_0 as shown in Fig. 3.1. Its integral form is written, according to (5.20), as

$$
V = -\frac{1}{2\pi} \int_{-\infty}^{\infty} \sum_{i=1}^{t} \int_{h_{i-1}}^{h_i} \widetilde{E}_{y,i} dy d\alpha \tag{5.29}
$$

where

$$
\int_{h_{i-1}}^{h_i} \widetilde{E}_{y,i} dy = \bar{A}_{y,i} \int_{h_{i-1}}^{h_i} e^{\gamma_i(y-h_\square)} dy + \bar{B}_{y,i} \int_{h_{i-1}}^{h_i} e^{-\gamma_i(y-h_\square)} dy
$$
$$
= \frac{\bar{A}_{y,i}}{\gamma_i} \left[e^{\gamma_i(h_i - h_{i-1})} - 1 \right] - \frac{\bar{B}_{y,i}}{\gamma_i} \left[e^{-\gamma_i(h_i - h_{i-1})} - 1 \right],
$$
$$
h_\square = h_{i-1}, \ i > 1 \tag{5.30}
$$

and

$$
\int_{h_0}^{h_1} \widetilde{E}_{y,1} dy = \bar{A}_{y,1} \int_{h_0}^{h_1} e^{\gamma_1(y-h_1)} dy + \bar{B}_{y,1} \int_{h_0}^{h_1} e^{-\gamma_1(y-h_1)} dy
$$
$$
= \frac{\bar{A}_{y,1}}{\gamma_1} \left[1 - e^{-\gamma_1 h_1} \right] - \frac{\bar{B}_{y,1}}{\gamma_1} \left[1 - e^{\gamma_1 h_1} \right], \ h_\square = h_1, \ i = 1 \tag{5.31}
$$

when $x_0 = 0$ and $z_0 = 0$. Then the impedance defined by voltage and current is expressed as

$$
Z_{VI} = \frac{V}{I_z}. \tag{5.32}
$$

5.4.3 Power-Voltage Definition

With the power and voltage calculated, the characteristic impedance has the following form

$$Z_{PV} = \frac{|V|^2}{2P^*}. \tag{5.33}$$

However, there is no unique definition for the voltage, especially in the multilayered-multiconductor systems. So the ambiguousness of voltage calculation can cause deviations between the impedances using different definitions [48].

5.5   Numerical Issues

In this section, problems related to the numerical analysis are discussed. The accuracy of the final results strongly depends on the numerical stability and convergence. Thus, efficient and accurate algorithms are highly critical in the numerical simulations.

The existence of metallization layers brings numerical difficulties to evaluate the Green's function when using the original transfer matrix method [22]. Because the high conductivity makes $\dot{\varepsilon}_i$ a large negative imaginary number, the propagation constant $\gamma_i^2 = \alpha^2 + \gamma_z^2 - \omega^2 \dot{\varepsilon}_i \mu_i$ inside the metal may become rather large when the arguments α and ω increase. The original formulation in [22] chose the hyperbolic sine and cosine functions inside transfer matrices. However, both $\sinh x$ and $\cosh x$ increase exponentially with the variable x, which would generate large errors because of the loss of significant digits in floating-point arithmetic. Moreover, for γ_i with a large positive real part, the hyperbolic sine and cosine functions become identical numerically, which makes the transfer matrix become highly singular to operate calculation.

Another difficulty is the overflow problem that can halt the program. When γ_i increases, the exponential factor $e^{\gamma_i \Delta h_i}$ may exceed the largest number defined in floating-point system. Particularly, for the IEEE standard double precision, the data is in the approximate ranges of

$$-1.7977 \times 10^{308} < \text{negative number} < -2.2251 \times 10^{-308}$$

$$+2.2251 \times 10^{-308} < \text{positive number} < +1.7977 \times 10^{+308}.$$

Roughly, the real part of $\gamma_i \Delta h_i$ cannot be larger than about 709. Otherwise the overflow occurs. One solution is to redefine the data structure and arithmetic operations for complex

numbers by writing large numbers into two parts as mantissa and exponent. This can be accomplished by the overloading operations in Fortran90 or C++. However, the consequent program slowdown becomes inevitable.

This dissertation proposes a numerically friendly formulation for the transfer matrices. The normalization-based procedure is applied by using the exponential functions as the basic solution set. The large coefficients are extracted and absorbed by the unknown coefficients in (3.32)-(3.35) to avoid large entries in matrices.

How to find the roots (eigenvalues) of the characteristic equation $\det[K(\gamma_z)] = 0$ belongs to non-linear eigenvalue problems. When γ_z is complex, the search region is on the complex plane that needs special considerations. This research uses the Muller method, as a global root finding method [81]. The deflation technique can be applied for multiple roots finding when solving the high-order modes. Some references, such as the bordering deletion and substitution method, and the continuation method, can be applied too.

Moreover, the accuracy of final results strongly depends on the convergence of the infinite integral in the spectral domain. Efficient numerical integration algorithms are critical. The Green's functions and integral equations for multilayered structures are normally the Sommerfeld-typed integrals, whose high-oscillation and slow-convergence properties make this type of integral difficult to evaluate. Normally, an integration path is chosen slightly above the real axis to avoid the pole singularity. In the lossy transmission lines, the integral over the real axis is much easier than the lossless case because the poles are located off the real axis due to the loss. Some procedures, such as the method of average [82] and the extrapolation method [83], have been developed to handle the oscillation features of the integrand and overcome the slow convergence.

For the Galerkin's method, the singularity of the moment matrix may become severe when using more terms of basis functions to expand unknown currents. The reason is that the contribution from the high-order terms becomes negligible, which makes relevant matrix rows become linearly dependent. Because of this linear dependence, the Gaussian elimination and LU decomposition algorithms are not accurate anymore for the matrix inverse and determinant

calculation. In this case, the singular value decomposition algorithm should be implemented to calculate the inverse matrix, determinant, and eigenvectors.

In addition, Table 5.1 shows one example of the convergence test with different numbers of current bases. The Chebyshev polynomials in (3.58) and (3.59) are used to calculate the effective permittivity of a one-layered open microstrip line [84]. The dielectric has a height of $1.27\,\mathrm{mm}$ and a relative permittivity of 9.7. The width of signal strip is $1.219\,\mathrm{mm}$. The effective permittivity is calculated at $1\,\mathrm{GHz}$ using the SDA. The results using both J_z and J_x currents and using J_z only are compared with the reference, respectively. A good agreement and self convergence are shown from the table.

Table 5.1: Convergence Test of $\varepsilon_{r\mathrm{eff}}$ With Different Terms of Basis Functions

J_x and J_z		J_z only	
$M_x \times M_z$	$\varepsilon_{r\mathrm{eff}}$	M_z	$\varepsilon_{r\mathrm{eff}}$
8×8	6.51902559926726	8	6.51980828497660
6×6	6.51902559785295	6	6.51980828426080
4×4	6.51902559665970	4	6.51980828376461
2×2	6.51902563911439	2	6.51980808456485
1×1	6.51953647475041	1	6.51809326432949
The result in [84]	6.51941	The result in [84]	6.51914

CHAPTER 6.   NUMERICAL STUDY OF THE EFFECTS FROM THE FINITE THIN METALLIZATION

Previous chapters discuss the SDA techniques in studying the propagation characteristics of multilayered planar transmission lines. In this chapter, all these techniques are implemented into the real application. Corresponding transmission line properties are evaluated numerically and compared with the reference data. The influence of finite thin imperfect conductors over a broad frequency range is the central topics. Based on numerical results, empirical criteria and rules are concluded to help the design of interconnects and transmission lines.

The MIMS and MIMI structures are evaluated in Section 6.1. The slow-wave effects induced by the thin metallization ground are examined in Section 6.2. The final conclusions are presented in Section 6.3.

6.1   Case Study

In this section, the MIMS and MIMI structures are mainly studied. Fig. 6.1 shows the configuration of two multilayered open transmission lines with thin-film metallization. All layers are assumed to be uniform and infinite in lateral and longitudinal directions. w is the signal-strip width, while t and σ_c are the metal thickness and conductivity. The following subsections are arranged to investigate these two transmission lines separately. The effects from the thin-film metal ground are the main focus in this section.

6.1.1   Metal-Insulator-Metal-Semiconductor Structures

The MIMS structure is similar to the TFMSL structure [85]. The signal strip is assumed to be a PEC, while the ground layer is modeled by a complex permittivity as shown in (2.1).

First, to validate the numerical program, one MIS structure in [47] is considered. Fig. 6.2 shows the normalized guiding wavelength and attenuation per unit length as functions of frequency. Different conductivities of silicon substrates are considered. The reference data are marked with dot, cross, and rectangular markers. Our results show a good agreement. Fig. 6.2 exhibits that the slow-wave phenomenon is dominant as the frequency decreases [45].
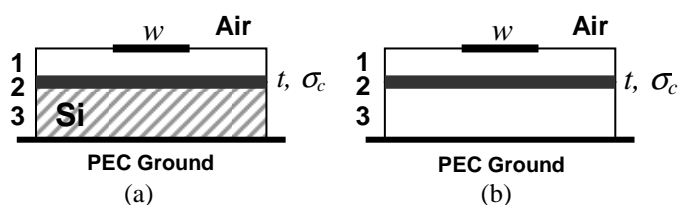
Figure 6.1: Multilayered planar transmission lines with the embedded thin-film metallization: (a) MIMS, (b) MIMI.

For a 3-layered MIMS structure, the frequency-dependant curves of SWF ($= \sqrt{\varepsilon_{eff}}$) and attenuation versus thickness t are plotted in Fig. 6.3. The MIMS structure is similar with the MIS case in Fig. 6.2 except for a copper metallization layer. The silicon substrate has a height of $250\,\mu$m with $\varepsilon_r = 12$ and $\sigma = 5\,$S/m. The silicon dioxide thickness is $1\,\mu$m with $\varepsilon_r = 4$. Between them is the thin copper ground layer with σ_c as $5.8 \times 10^7\,$S/m. w is $160\,\mu$m.

There are several boundary curves in Fig. 6.3. When t is zero, the microstrip degrades to a conventional MIS structure. The curves agree well with the results (circles) of Cano *et al.* [48]. When t becomes a PEC, the results agree with the quasi-TEM formula [86]. When t becomes infinite (IBC model), the whole metallization layer becomes opaque and attenuates all fields. Other curves representing nonzero-t values converge sequentially to this infinite-t curve. This shows that, at very high frequencies, the skin depth is much smaller than the metal thickness to make the thin-film metal work as a very thick conductor. And EM fields are mainly confined within the silicon dioxide layer, which is also called the skin-effect mode. This mode follows the quasi-TEM field theory so that all the nonzero-t curves exhibit agreement with the PEC model at high frequencies. At low frequencies, similar large effective permittivities caused by slow-wave mode were also observed in [87]. However, both PEC and IBC models fail to describe such slow-wave phenomenon. It is evident that this thin-film ground can isolate the
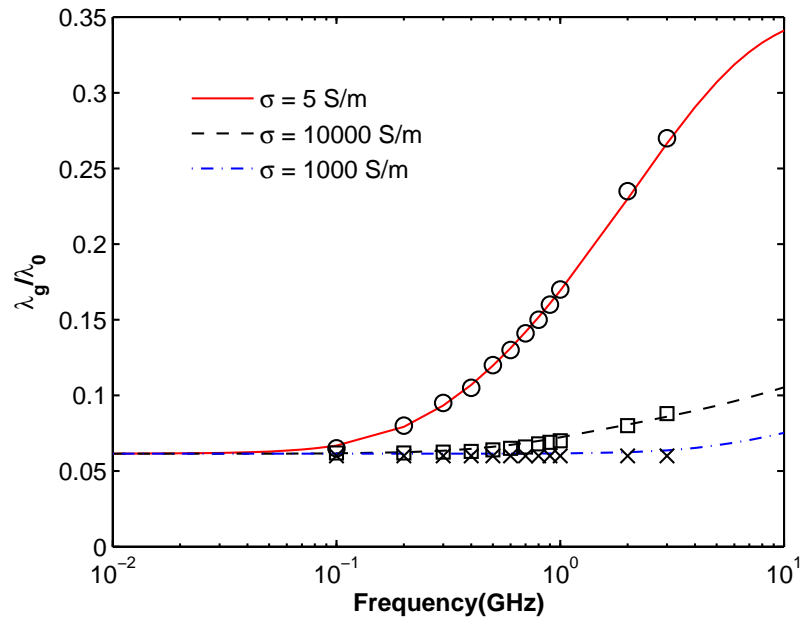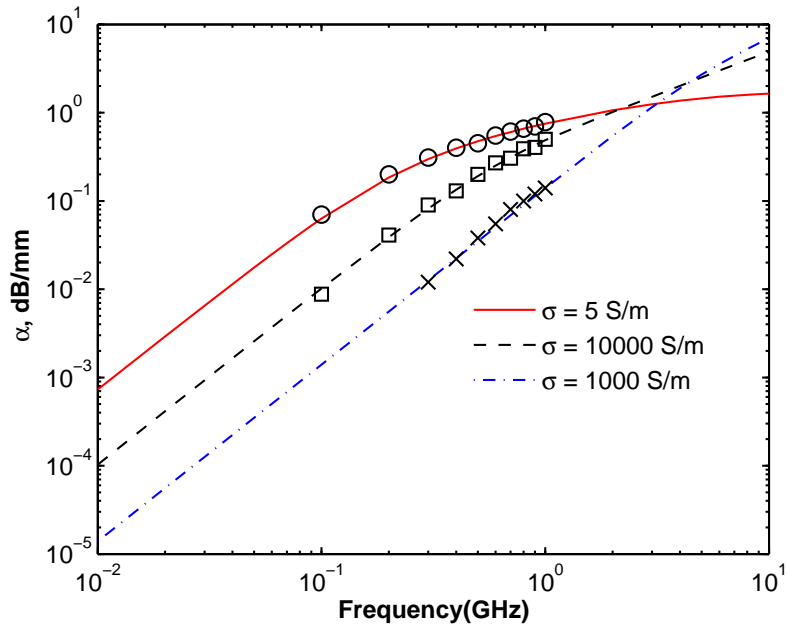
Figure 6.2: Propagation characteristics of a MIS structure versus frequency and substrate conductivity, silicon: $250\,\mu$m, ε_r: 12, silicon dioxide: $1\,\mu$m, ε_r: 4, w: $160\,\mu$m: (a) normalized guiding wavelength, (b) attenuation constant (dots: results from [47]).

lossy silicon substrate.

Fig. 6.3(b) shows that the attenuation is proportional to the square root of frequency in high-frequency range. The reason is the model only considers the loss from the thin-film ground instead of the signal strip. Thus, at high frequencies where the skin effect is dominant, the model attenuation is mainly determined by the real part of the surface impedance from the metallization layer. At low frequencies, the metal ground thickness is sufficiently smaller than the skin depth and the propagation mode tends to be quasi-static. The whole thin metallization layer and substrate can be modeled as shunt conductances that cause the attenuation to increase with the square of frequency.

Moreover, in Fig. 6.3(b), the low frequency attenuation shows a minimal respect to the film thickness t. The attenuation at t equals $0.05\,\mu$m is found to be less than the zero-t case. One physical explanation is that the thin metal ground isolates the lossy substrate and diminishes the total loss by blocking the electric field, especially the fringing field, from reaching the lossy substrate. But when t increases to some extent, the ohmic loss increases from the metallization layer overcomes the loss reduction from the ground-shielding effect. Then the total attenuation becomes higher again. So an optimal thickness may exist to attain a minimum attenuation. Similar optimal thickness was also found in [64].

The contour plots of the SWF and attenuation constant as functions of frequency and thickness are shown in Fig. 6.4. The dash lines in figures stand for the different skin depths with factors from 1 to 4 separately. With large t, say $100\,\mu$m, nearly all lines become parallel to each other and unchangeable with frequency. This behavior reveals the convergence to the infinite-t case. Actually, when the thickness is between 2δ and 3δ, almost all contour lines converge to the parallel lines. In other words, the criteria of the thick-enough metallization is to be at least thicker than 2δ. Moreover, another point to note is that when thickness t reaches some critical points around $3\,n$m, the attenuation constants are at a minimum. This minimal-loss phenomenon is similar to the ones in [44], [63], where the minimum attenuation is related to the critical substrate conductivity instead.

The relevant field distributions are plotted in Figs. 6.5. Three points at $10\,$MHz, $1\,$GHz, and
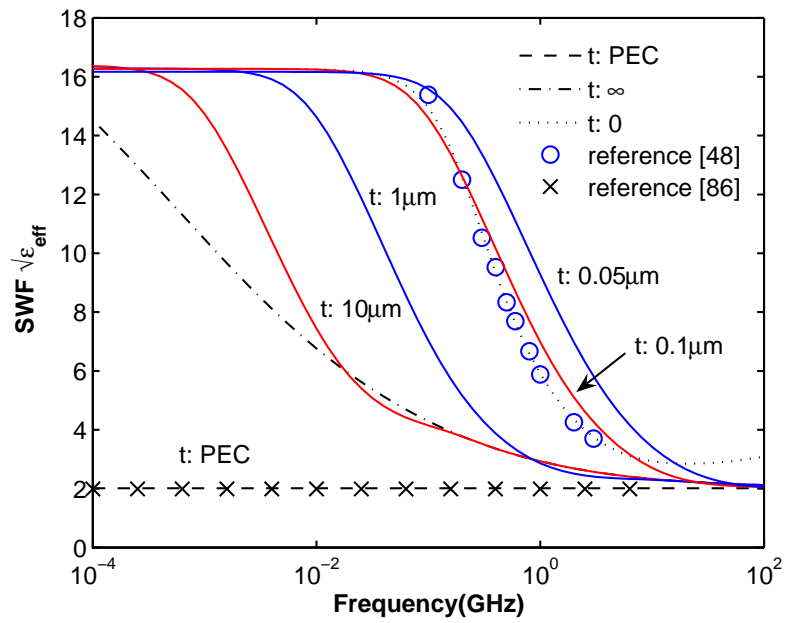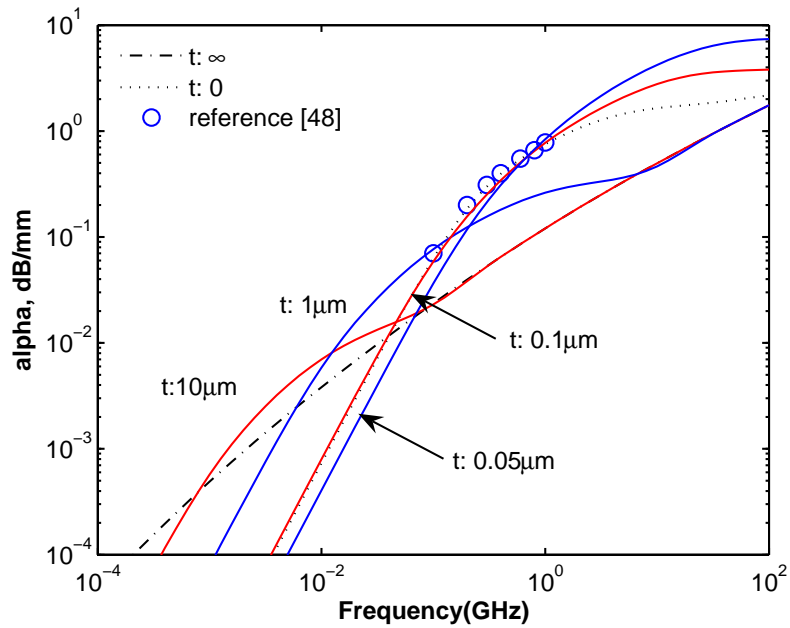
Figure 6.3: Propagation characteristics of a MIMS structure as functions of frequency and metallization thickness, semiconductor: $\varepsilon_r = 12$, $\sigma = 5\,\mathrm{S/m}$, $250\,\mu\mathrm{m}$, metallization: $\sigma_c = 5.8 \times 10^7\,\mathrm{S/m}$, insulator: $\varepsilon_r = 4$, $1\,\mu\mathrm{m}$, $w = 160\,\mu\mathrm{m}$: (a) slow wave factor ($\sqrt{\varepsilon_{eff}}$), (b) attenuation per unit length.
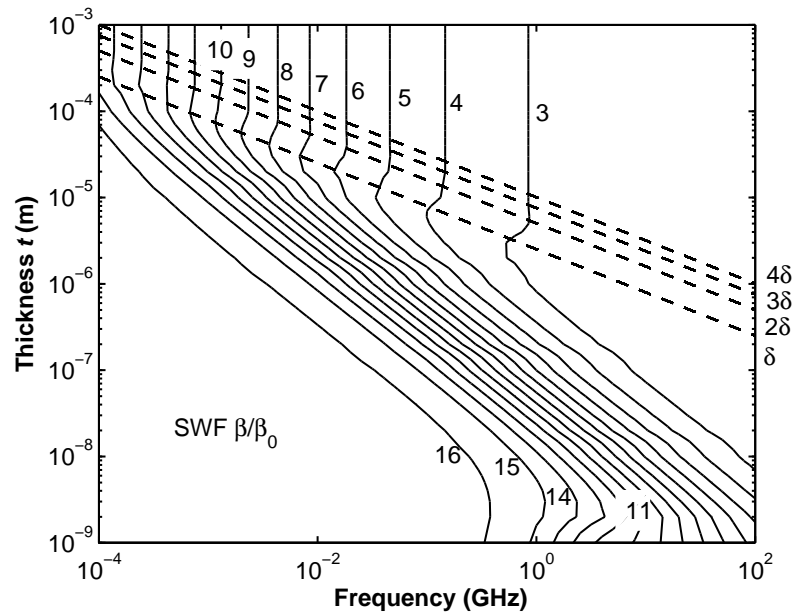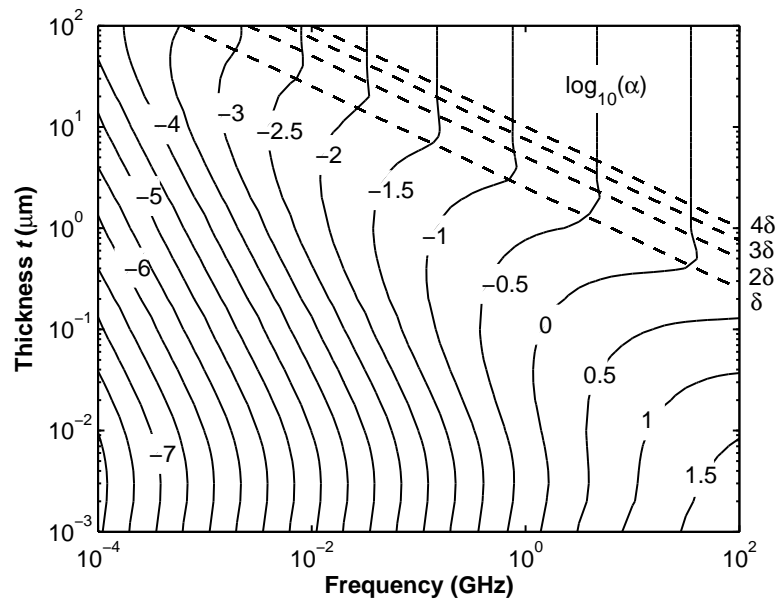
Figure 6.4: Contour plot for electrical characteristics of the MIMS structure (Other data as in Fig. 6.3): (a) slow wave factor, (b) attenuation $\log_{10}(\alpha)$.
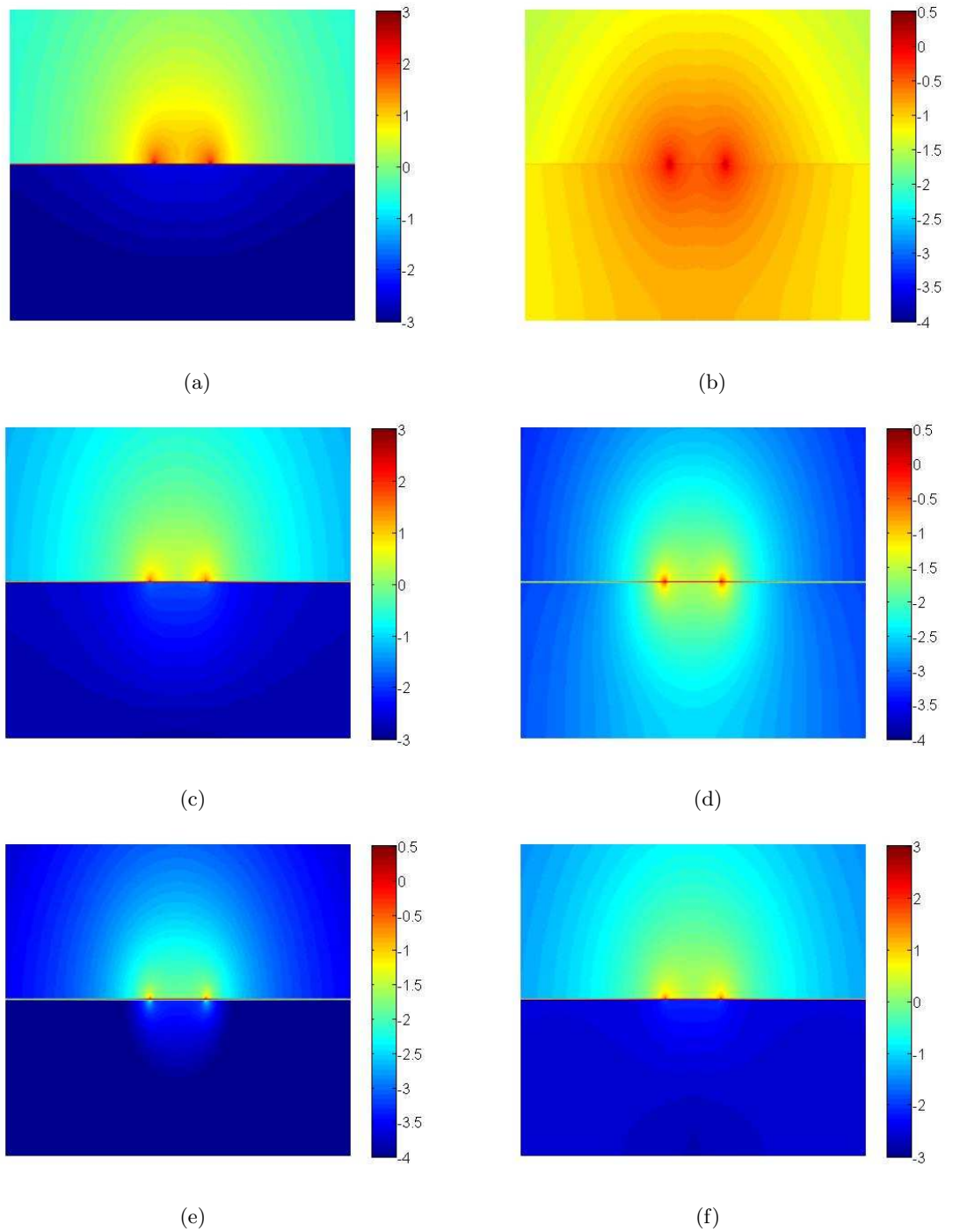
Figure 6.5: Total field amplitude distribution of the MIMS structure as Fig. 6.3 with $t = 1\,\mu$m (left column: total electric fields, right column: total magnetic fields, both in $\log_{10}$ scale): (a, b) 10 MHz slow-wave mode, (c, d) 1 GHz transition region, (e, f) 30 GHz skin-effect mode.

30 GHz on the $t = 1\,\mu$m curve are chosen separately from Fig. 6.3(a). For the slow-wave mode in Figs. 6.5(a) and 6.5(b), at 10 MHz, the magnetic field penetrates into the silicon substrate, whereas the electric field is shielded. Such spatial discrepancy of electric and magnetic fields slows down the wave propagation velocity. On the contrary, in Figs. 6.5(e) and 6.5(f), the skin-effect mode shows that both electric and magnetic fields are strongly coupled, shielded by the thin metal ground, and confined within the SiO$_2$ layer where the velocity is high. In the transition region as Fig. 6.5(c) and 6.5(d), the magnetic field shows modest penetration.

Fig. 6.6 plots the characteristic impedances of the MIMS versus frequency and metallization thicknesses. When t becomes zero, the real part of Z_0 increases rapidly with frequency due to the decreased equivalent shunt capacitance during the transition from the slow-wave mode to the dielectric quasi-TEM mode. The imaginary part shows the total reactive power is influenced mainly by the shunt capacitance. As t becomes nonzero, however, the real parts of Z_0 decrease and converge to the PEC limit at high frequencies. This is attributed to the transition from the slow-wave mode to the skin-effect mode where the quasi-TEM approximation still holds well since the line dimensions remind small compared to the wavelength. In the skin-effect mode, the real impedance is reduced by the metallization layer because this layer also diminishes the magnetic fields in silicon substrate to reduce the equivalent series inductance. The imaginary parts show that the reactive power is influenced by the series inductance. Thus the characteristic impedance has a marked dependence on the metallization thickness of the ground plane.

Moreover, another practical MIMS structure is studied to compare the three definitions of impedance. The silicon dioxide ε_r is 4 and its thickness is $4\,\mu$m. The width of strip w is $10\,\mu$m. The bulk silicon substrate is $500\,\mu$m thick with $\varepsilon_r = 12$ and conductivity $\sigma = 10\,$S/m. The metallization layer has a conductivity $\sigma_c = 5.88 \times 10^7\,$S/m.

In Fig. 6.7, the relation between characteristic impedance and frequency are plotted under different impedance definitions and different thickness t of the ground substrate. Compared with the reference's results [88], it shows the power-current defined impedance is the most accurate results among all three impedances. The difference is due to the voltage definition as
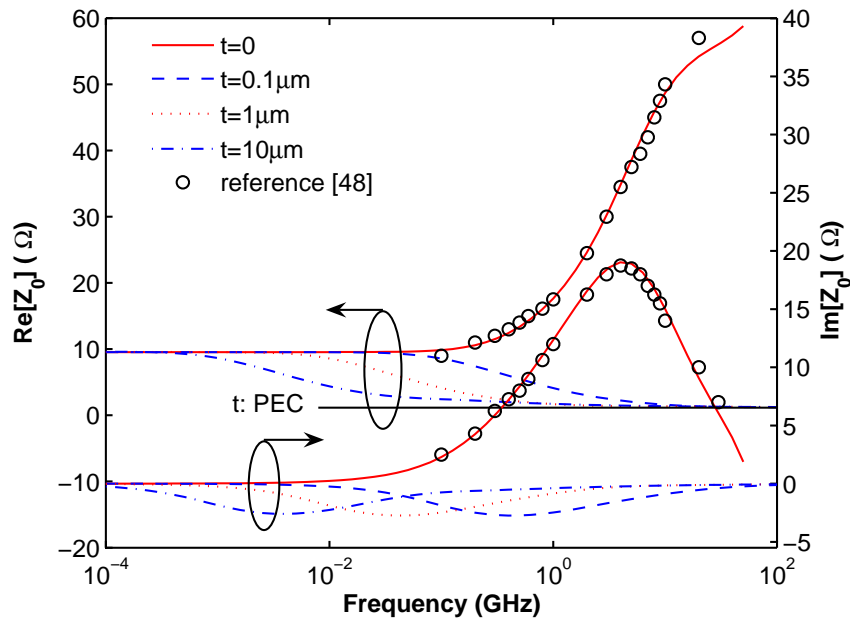
Figure 6.6: Real and imaginary parts of the characteristic impedance of the MIMS structure in Fig. 6.3 as functions of frequency (circle dots: results from [48]).
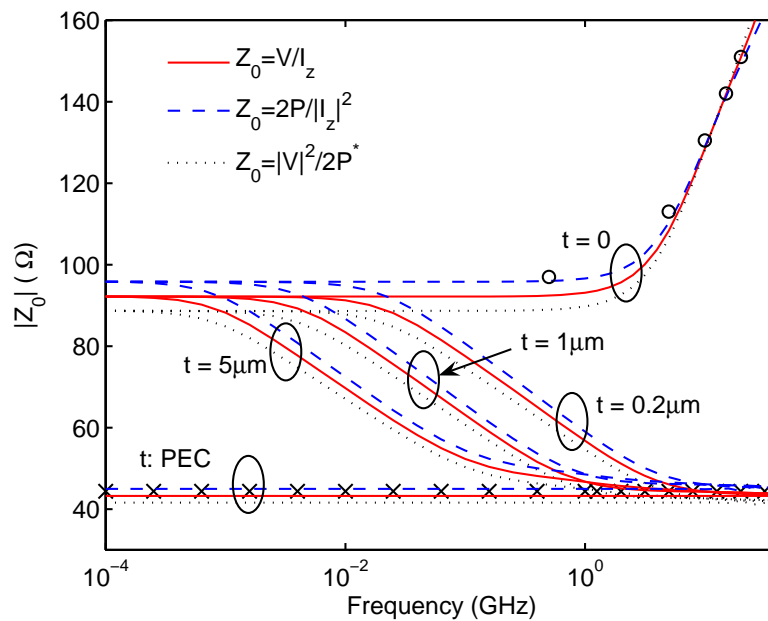
Figure 6.7: Frequency behavior of absolute values of characteristic impedances of a practical MIMS structure versus metallization thickness t, silicon substrate: $\varepsilon_r = 12$, $\sigma = 10\,\mathrm{S/m}$, $500\,\mu\mathrm{m}$, metallization: $\sigma_c = 5.88 \times 10^7\,\mathrm{S/m}$, silicon dioxide: $\varepsilon_r = 4$, $4\,\mu\mathrm{m}$, $w = 10\,\mu\mathrm{m}$ (circle dots: results from [88], cross dots: empirical formula [56]).

a path integral is not unique and cannot guarantee the fundamental relation between power, current, and voltage. When the thickness t becomes zero, the structure becomes a pure MIS microstrip. When the frequency goes up beyond about $2\,\mathrm{GHz}$, the $|Z_0|$ increases rapidly. This is due to the mode transition from the slow-wave mode to the quasi-TEM mode. However, when the thickness t is nonzero, the impedances decrease when frequencies increase, and finally converge to the limit where the thin metallization layer works as a PEC. This behavior is due to the reason that the operation mode transits from the slow-wave to skin-effect mode and the magnetic fields in silicon are diminished to reduce the series inductance consequently.

Figs. 6.8(a) and 6.8(b) demonstrate the extracted resistance and inductance vary with the frequency. The thin metallization layer leads to larger resistance. At low frequency region, for all cases, the resistances are proportional to the square of the frequency. This is due to the ohmic loss caused by electric currents flowing through the whole metallization layer and silicon substrate. At high frequencies, the resistances with thin metallization layers are proportional to the square root of frequency. This is due to the fact that the current of the skin-effect mode flows mainly through a region that is proportional to the skin depth. For the inductance, when $t = 0$ and frequency changes, the magnetic fields still distribute over the whole cross section as quasi-TEM mode, which keeps the series inductance almost unchanged. However, the thin metallization layer prevents magnetic fields from coupling into the substrate. As a result, the equivalent inductance decreases remarkably when the operation mode transfers from the slow-wave to skin-effect modes.

The equivalent shunt capacitance and conductance are illustrated in Figs. 6.9(a) and 6.9(b). With the thin metallization layer, for both slow-wave and skin-effect modes, almost all electric fields are constrained in the dioxide layer, so the capacitance from the silicon dioxide is dominant. And the capacitance remains almost flat with frequency. Without the metallization layer, the capacitance of silicon dioxide is connected in series with the equivalent capacitance of silicon substrate, so the total capacitance becomes smaller. This is shown explicitly in Fig. 6.9(a). In Fig. 6.9(b), the shunt conductance with the metallization layer is almost zero because the thin metallization layer tends to work as a PEC and screen the effect of silicon
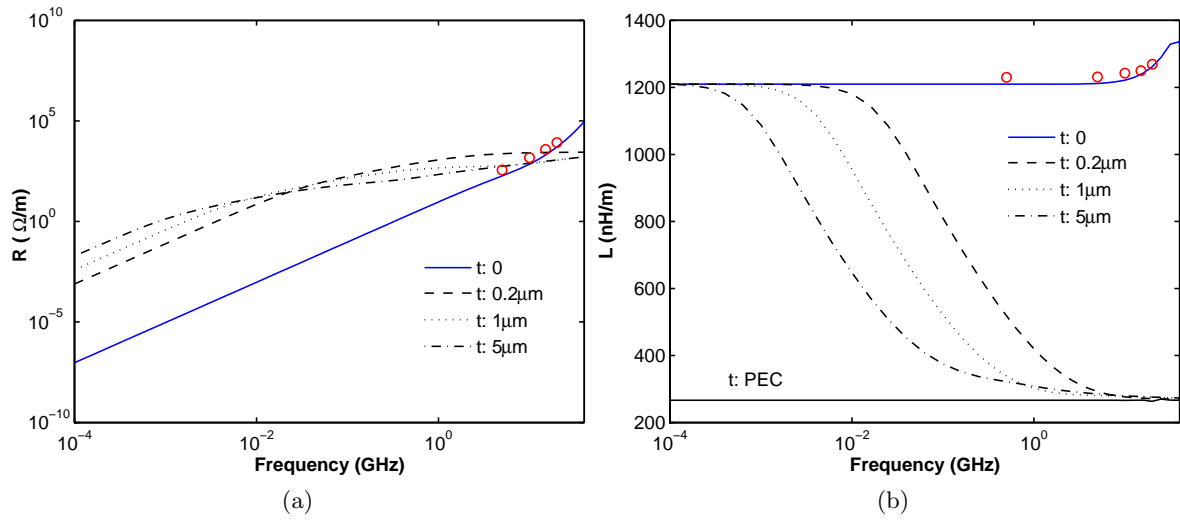
Figure 6.8: Frequency behavior of (a) series resistance and (b) inductance per unit line for the MIMS structure in Fig. 6.7 (circle dots: results from [88]).
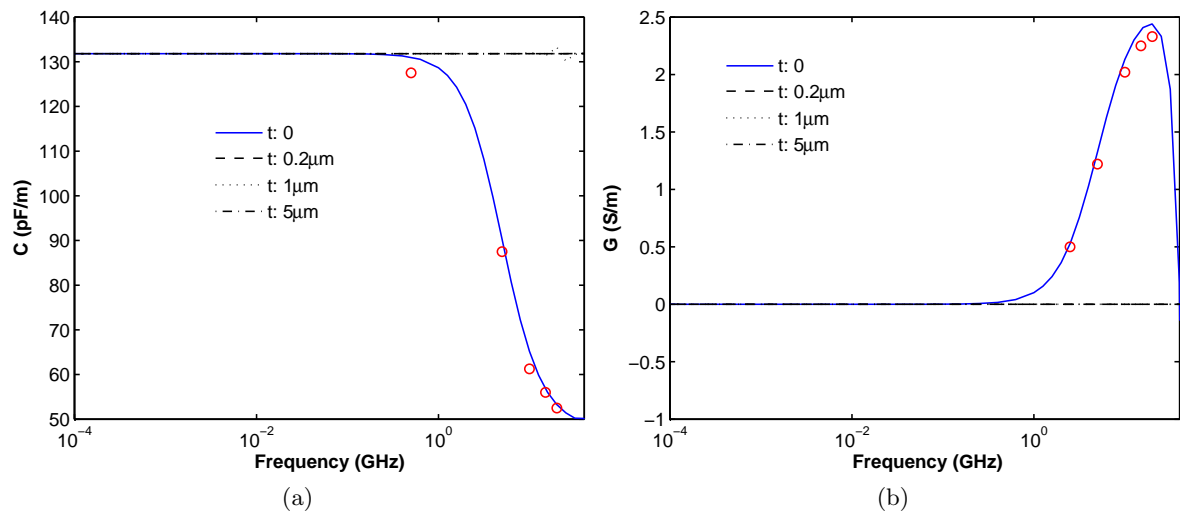
Figure 6.9: Frequency behavior of (a) shunt capacitance and (b) conductance per unit line for the MIMS structure in Fig. 6.7 (circle dots: results from [88]).

substrate.

6.1.2 Metal-Insulator-Metal-Insulator Structures

As demonstrated before, the slow-wave is a comprehensive effect due to the influence coming from the lower lossy silicon substrate and thin metallization layer. To identify the influence of this metallization layer only, a thin metal layer is inserted into a lossless microstrip line as shown in Fig. 6.1(b). This metal layer is made of copper. The lossless dielectric material ($\varepsilon_r = 10.2$) is divided into two parts as $20\,\mu$m and $80\,\mu$m. The width of the metal strip line is $200\,\mu$m. The corresponding dispersion characteristics are shown in Figs. 6.10 and 6.11. The similar convergence patterns reoccur and accord with the previous discussions. This illustrates that the thin metallization layer can introduce the slow wave phenomenon in a lossless substrate. In addition, the noticeable difference between the PEC and real metal shows that the slow wave exists even when the metallization thickness is only small fraction of the skin depth, which is a phenomenon that the PEC cannot describe appropriately. Therefore, the thin metallization layer has a great impact on the dispersion characteristics of microstrip lines.

In Fig. 6.12, the real and imaginary parts of the impedance are also plotted. when t equals to zero, our result agrees with the Pramanick's [86]. The imaginary parts of the impedance is relatively small compared with the real parts. At the same time, when the metallization layer becomes thicker, the impedance converges to the PEC curve faster when frequency increase. This is because the reduction of the skin depth with increasing frequencies makes the thin metallization layer act as a very thick good conductor.

Fig. 6.13 plots the field distributions of the MIMI structure in different modes. The similar EM penetration phenomena like Fig. 6.5 appear again. It is also clear the thin metallization ground layer cannot shield the magnetic fields at low frequencies.

Moreover, a practical 50-Ω MIMI line is studied, where the carrier substrate (alumina) and thin dielectric layer (Hibridas photoimageable dielectric) are both lossless [89]. The alumina substrate is $635\,\mu$m thick with a relative permittivity $\varepsilon_r = 9.8$. The Hibridas dielectric layer has a thickness of $18\,\mu$m and its relative permittivity ε_r is 8. The signal strip w is $22.78\,\mu$m.
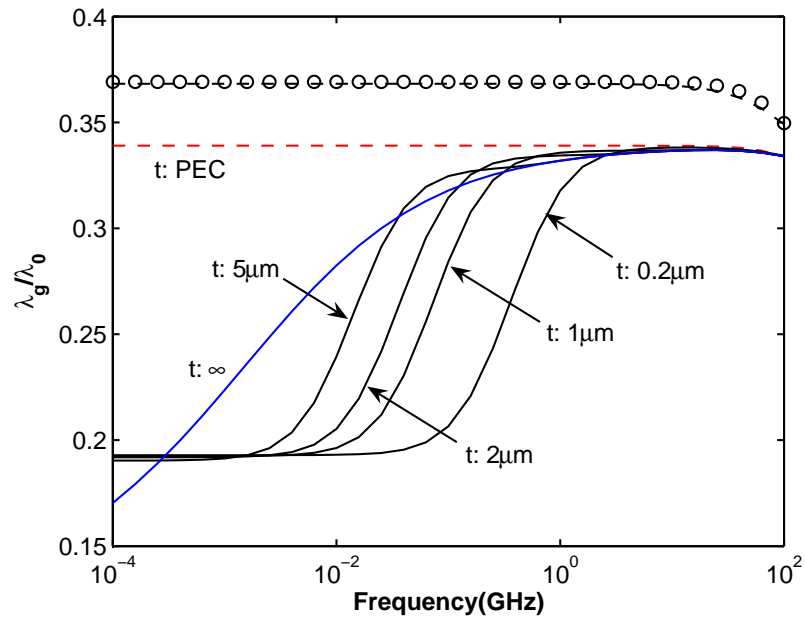
Figure 6.10: Normalized wavelength of a 3-layered MIMI open microstrip under different thicknesses t of thin metallization layer, lower dielectric substrate: $80\,\mu$m, ε_r: 10.2, thin metal σ: $5.8 \times 10^7\,$S/m, upper dielectric substrate: $20\,\mu$m, ε_r: 10.2, w: $200\,\mu$m, (circle dots: results from [86]).
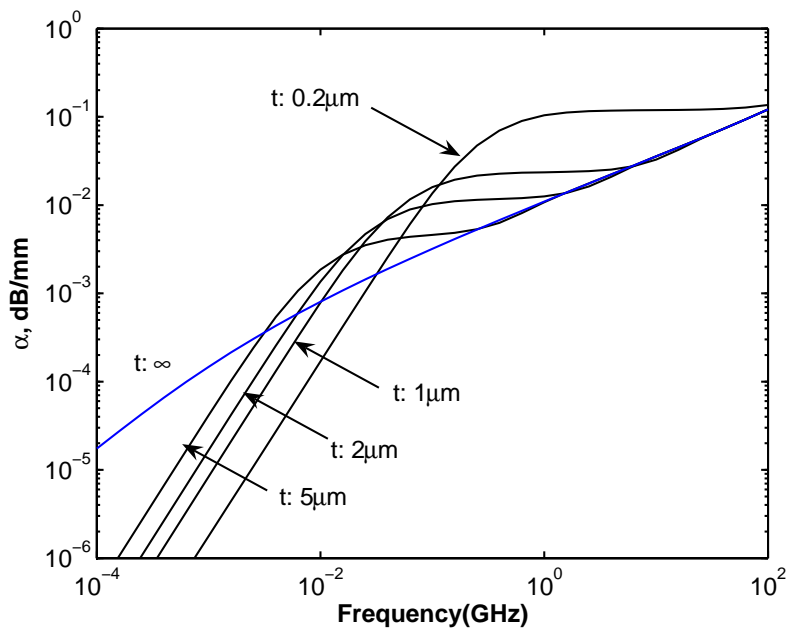
Figure 6.11: Attenuation constant of the 3-layered MIMI in Fig. 6.10.
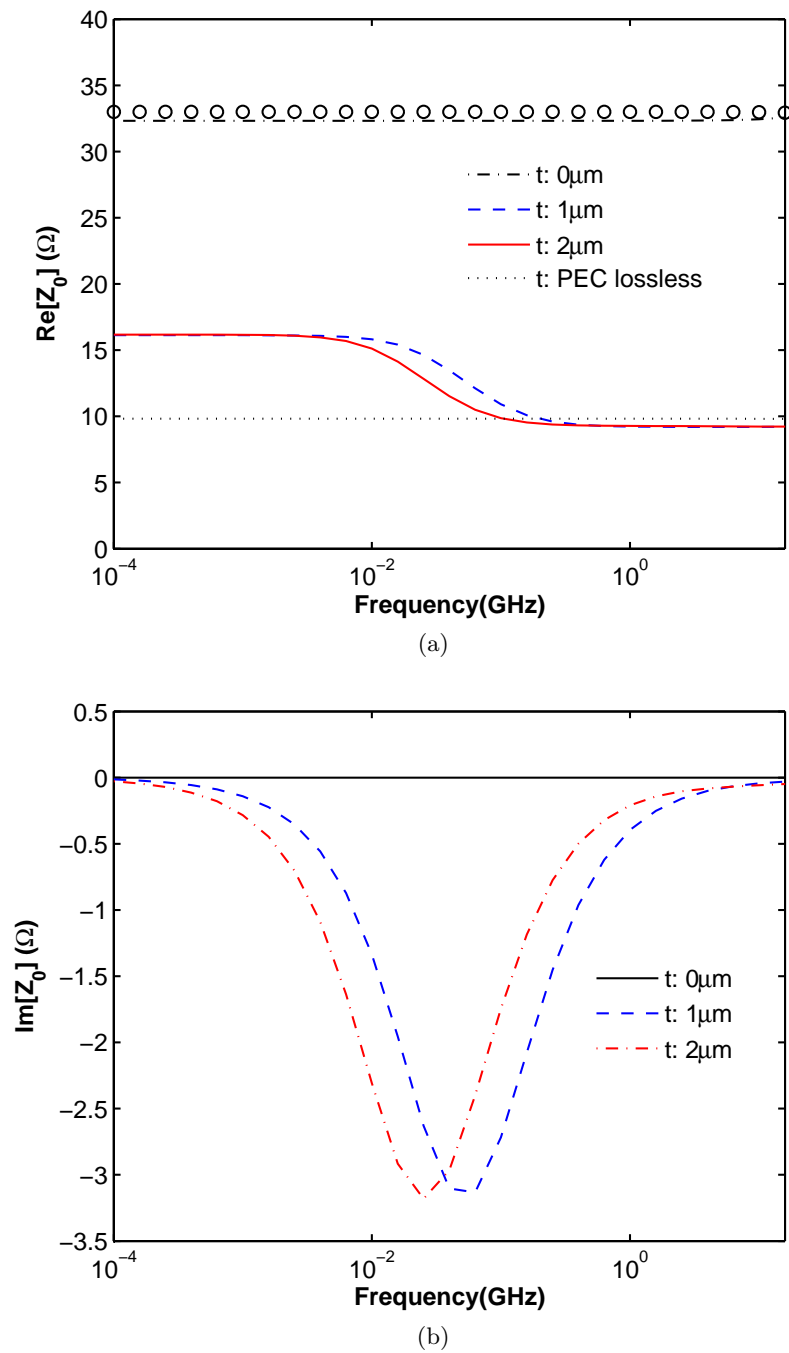
Figure 6.12: Frequency behavior of the (a) real and (b) imaginary parts of the characteristic impedance for the MIMI structure in Fig. 6.10 ($Z_0 = V/I$ definition, circle and diamond dots: Pramanick and Bhartia's results [86]).

83

(a)

(b)

(c)

(d)

(e)

(f)
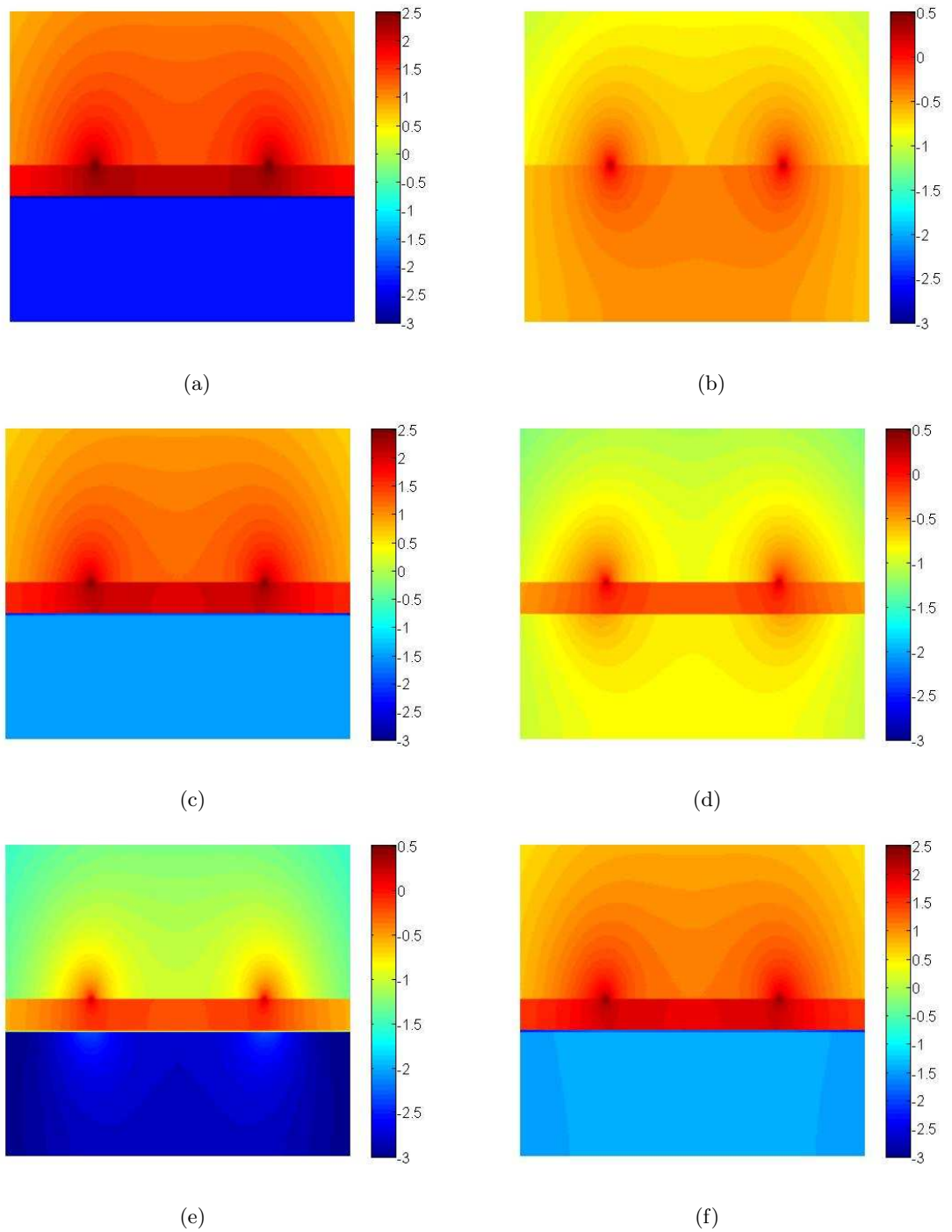
Figure 6.13: Total field amplitude distribution of the MIMI structure in Fig. 6.10 with $t = 1\,\mu$m (left column: total electric fields, right column: total magnetic fields, both in $\log_{10}$ scale): (a, b) 1 MHz slow-wave mode, (c, d) 100 MHz transition region, (e, f) 10 GHz skin-effect mode.
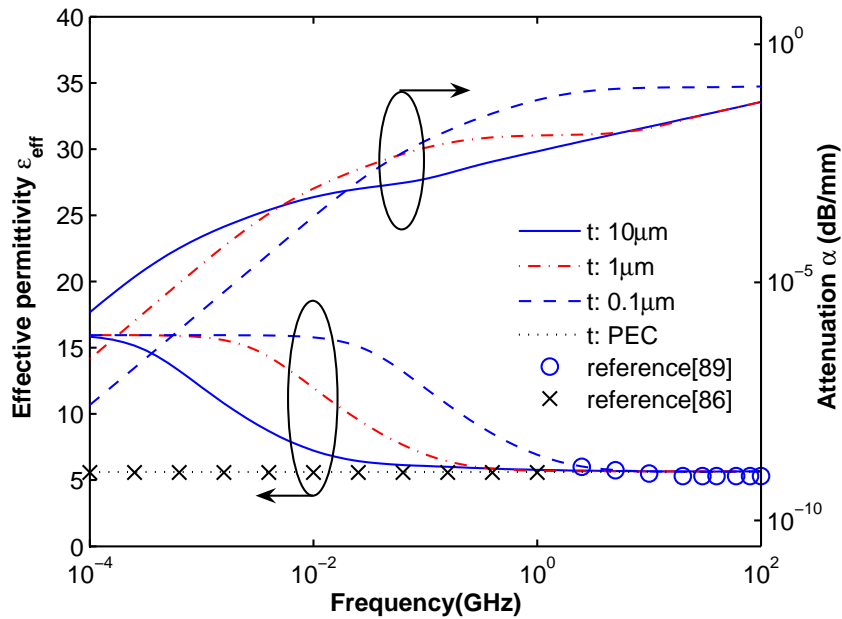
Figure 6.14: Effective relative permittivity $\varepsilon_{r\text{eff}}$ and attenuation constant α of a 50-Ω MIMI as functions of frequency and metallization thickness, alumina substrate: $\varepsilon_r = 9.8$, $635\,\mu\text{m}$, metallization: $\sigma_c = 5.8 \times 10^7\,\text{S/m}$, Hibridas dielectric: $\varepsilon_r = 8$, $18\,\mu\text{m}$, $w = 22.78\,\mu\text{m}$.
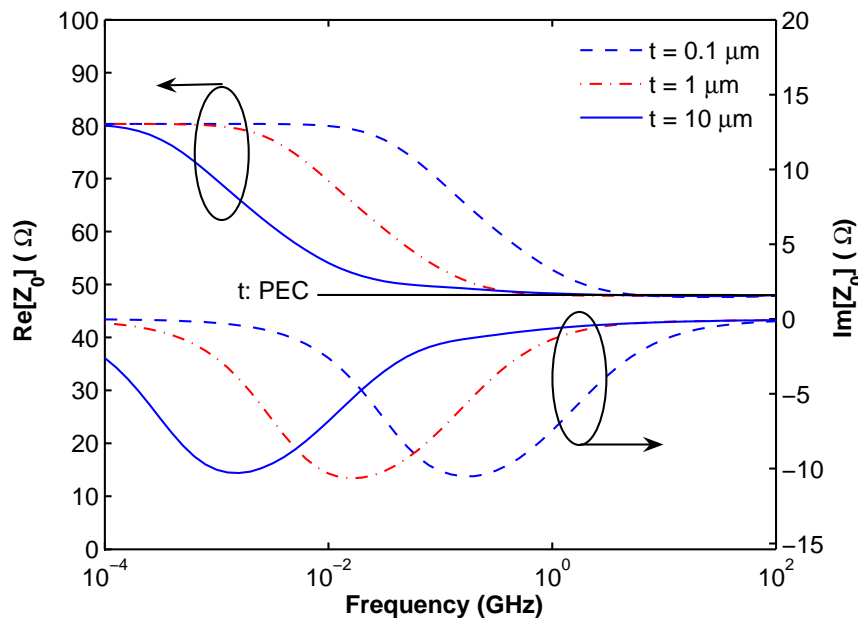
Figure 6.15: Real and imaginary parts of the 50-Ω MIMI characteristic impedance (other data as in Fig. 6.14).

The metallization has a conductivity of 5.8×10^7 S/m. t is the metal layer thickness. Fig. 6.14 shows the dispersive curves of the effective permittivity and attenuation. Similar slow-wave modes and stepwise convergence under different metallization thicknesses reoccur and accord with pervious explanation. Fig. 6.15 plots the corresponding impedances that reveal the similar behavior as Fig. 6.12. Therefore, the thickness factor of metallization layer is significant for the dispersion and slow-wave effect. Its existence introduces the lossy mechanism into the whole system.

6.2   Slow-Wave Effects in Transient Analysis

The transient characterization of electric interconnect and metallization structures has become an essential issue in the design of high-speed digital ICs. Unlike conventional lossless microstrip transmission lines, in which the higher harmonics (compared to the inflection frequency) travel at a lower velocity than the lower ones, typical IC interconnects are fabricated on lossy silicon substrates and have three signal propagation modes: the slow-wave mode, the skin-effect mode, and the quasi-TEM mode [45]. For low frequency harmonics, the slow-wave mode becomes dominant. In this section, the thickness effect of the thin metallization layer on the transient signal propagation is studied by the SDA and FFT technique. The TFMSL-typed interconnection, as shown in 6.1(a), is used to show that the transient pulse propagation is influenced by the presence of the thin-film metal ground layer and lossy silicon substrate. The waveform distortion under different metallization thicknesses is simulated. It shows such thin-film metallization can shield the lossy substrates and enhance slow-wave mode propagation.

In order to illustrate the impact of metallization thickness on the attenuation and distortion of the transient signal, a Gaussian pulse defined as (5.9) and a rectangular pulse are input into a 20 mm MIMS interconnection line in Fig. 6.3. Their transient responses are plotted in Figs. 6.16 and 6.17. The undistorted input pulses are included for comparison. The figures depict the signal suffers severe attenuation in the conventional MIS structure ($t = 0$), which is due to its large attenuation constant for high-frequency harmonics. With the embedded
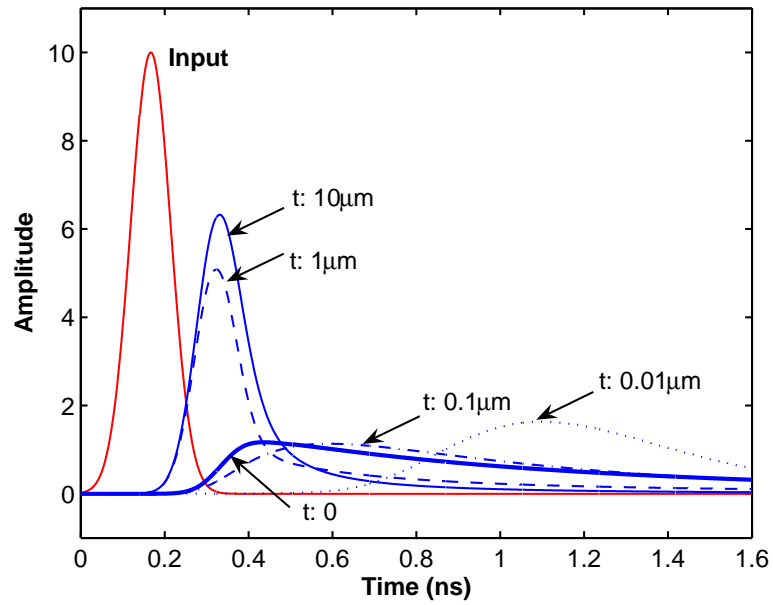
Figure 6.16: Transient responds of the MIMS structure in Fig. 6.3 at a distance $L = 20\,\text{mm}$ with different metallization thicknesses t, Gaussian pulse (f_c: $0\,\text{Hz}$, τ: $47.75\,ps$, t_p: $0.167\,ns$).
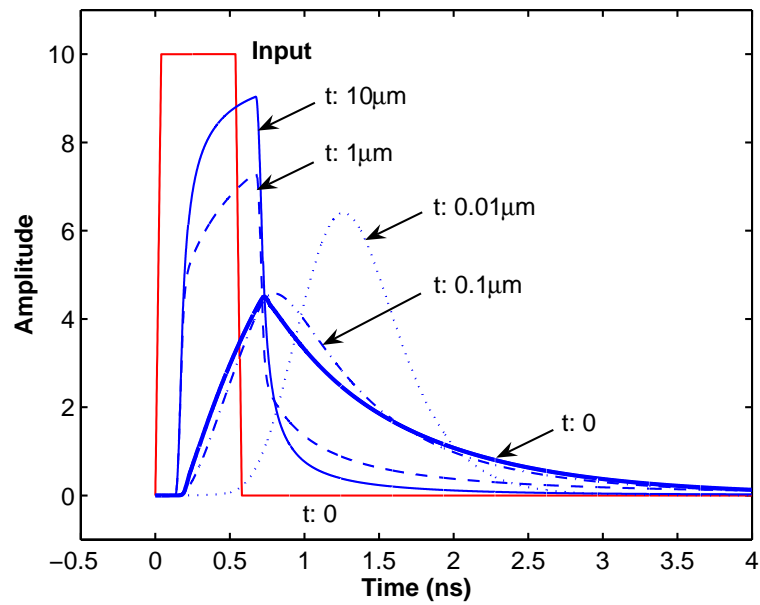
Figure 6.17: Transient responds of the MIMS structure in Fig. 6.3 at a distance $L = 20\,\text{mm}$ with different metallization thicknesses t, Rectangular pulse (t_r: $40\,ps$, t_f: $40\,ps$, t_w: $500\,ps$).

metallization ground plane, the overall attenuation is reduced. This indicates the advantage of the TFMSL as that the ground metallization screens the lossy substrate effect [85]. In addition, the latency in the communication through the interconnection is shown. When t equals $0.01\,\mu$m, the transmission system has a slow-wave mode up to about $1\,$GHz, so the corresponding pulse delays are the maximal among all the curves. For large t, e.g. $10\,\mu$m, the metallization layer tends to work as a metal ground and makes the interconnect become a single-layer SiO_2 microstrip line to reduce the time delay and overall attenuation.

Table 6.1: Effective Transmission Parameters from the Transient Analysis

Thickness t	Velocity v_g	Attenuation α
$0\,\mu$m	$7.442 \times 10^7\,$m/s	$0.9309\,$dB/mm
$0.01\,\mu$m	$2.146 \times 10^7\,$m/s	$0.7860\,$dB/mm
$0.1\,\mu$m	$4.707 \times 10^7\,$m/s	$0.9449\,$dB/mm
$1\,\mu$m	$1.280 \times 10^8\,$m/s	$0.2936\,$dB/mm
$10\,\mu$m	$1.217 \times 10^8\,$m/s	$0.1990\,$dB/mm

Table 6.1 shows the estimated group velocity and overall attenuation constant for structures under different metallization thicknesses. These parameters are calculated by finding the peak values and delays of distorted Gaussian pulses in Fig. 6.16 and comparing them with the original input signal. Table 6.1 points out, when t equals $0.1\,\mu$m and $0.01\,\mu$m, the interconnect has lower group velocities than the conventional MIS structure. In addition, with thick metallization, the signal transmission in the interconnect is speeded up by about factor 2 and has much less transmission loss.

Fig. 6.18 illustrates the transient response of a Gaussian pulse modulated in three different work regions: the slow-wave region (A), the transition region (B), and skin-effect region (C). Different center frequencies and frequency bandwidths are selected to fit the Gaussian pulse exactly within these three regions. Using the numerical data in Fig. 6.18(c)-(d), the values for the effective group velocity and attenuation are estimated. For slow-wave region (A), the velocity is about $1.309 \times 10^7\,$m/s with a small attenuation $7.541 \times 10^{-8}\,$dB/mm. The waveform distortion is almost undetectable. In transition region (B), the velocity is $4.366 \times 10^7\,$m/s but with a higher attenuation as $0.07708\,$dB/mm. For the skin-effect region (C), the highest speed
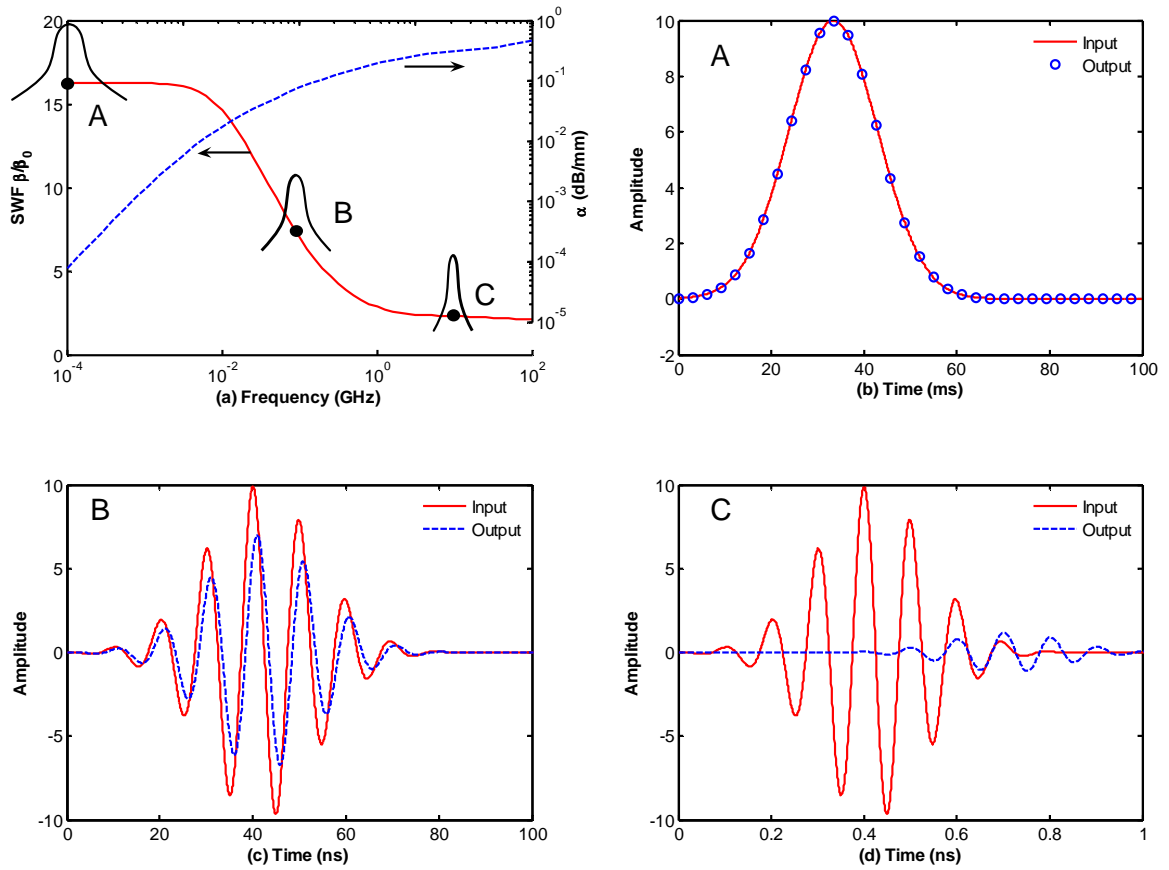
Figure 6.18: Transient responds with the Gaussian pulse in different working regions, $t = 1\ \mu$m, MIMS structure in Fig. 6.3 with $L = 40$ mm: (point A) slow-wave region (f_c: 0 Hz, τ: 9.549 ns , t_p: 33.4 ms), (point B) transition region (f_c: 100 MHz, τ: 11.94 ns, t_p: 41.8 ns), (point C) skin-effect region (f_c: 10 GHz, τ: 0.1194 ns, t_p: 0.418 ns).

of 1.326×10^8 m/s is achieved but also with the largest attenuation 0.4613 dB/mm, which causes severe amplitude distortion.

6.3   Conclusions

The effects of a thin-film metal ground have been studied by the SDA. Two transmission line structures, the MIMS and MIMI, are analyzed. The numerical results show that the EM fields can penetrate the metallization and couple with layers underneath. The corresponding EM leakage, especially of the magnetic field, can excite or even enhance the slow-wave mode into higher frequency regions. The propagation characteristics are influenced significantly by the backside thin-film metallization if its relative thickness is comparable to the skin depth. If being about 2δ to 3δ thick, the metallization ground is thick enough to behave as an infinitely-thick metal substrate. In addition, an optimal thickness is observed to obtain the minimal attenuation.

The thin metallization ground layer influences the characteristic impedances. From the analysis of the extracted RLCG parameters, it shows that the thin metallization layers have significant impacts on the series resistance and inductance. On the contrary, this layer works as ground to shield the influence from the bulk silicon to make shunt capacitance and conductance unchanged with frequency.

At last, the numerical results indicate the thickness factor of the thin metal ground has a great impact on the transient response. With very small thickness, this metallization layer can actually slow down the pulse propagation in interconnects. In conclusion, all these effects are of importance in the performance analysis of IC interconnects and packaging.

CHAPTER 7.   CONCLUSIONS AND FUTURE WORK

This research investigates the accurate modeling of semiconductor-based transmission lines with thin metallization components. The SDA is used to study the propagation characteristics. The spectral-domain Green's functions for the lossy multilayered structure are derived by the transfer matrix method and SDIA. In this research, a new formulation for the transfer matrix method is proposed to solve the potential overflow problems caused by metallization layers. The Green's functions yield complex integral equations for the unknown currents on conductors. These equations are solved by the MoM and Muller method to get the complex propagation constant and current distribution.

With the calculated complex propagation constant and current distribution, the electrical properties of multilayered transmission lines are investigated. This dissertation presents a complete picture to study the EM properties of transmission lines, such as the effective permittivity, propagation attenuation, transient response, spatial field distribution, characteristic impedance, and extracted RLCG parameters of the circuit model. Computer codes are developed to study the effects from the thin metallization components.

Besides the SDA, the parallel-plate waveguide model is also implemented to study the imperfect metallization effects. The fundamental TM mode is investigated by the exact eigenvalue equations and the low-frequency approximations. The first- and second-order low-frequency approximations of the propagation constant are derived. These approximations are compared with the exact solutions to access the validity. Moreover, corresponding equivalent circuits are modeled based on the approximate formulation.

All numerical results show that the EM properties of transmission lines can be influenced significantly by the backside thin-film metallization layer. This influence also depends on the

nature and configuration of the metallization like the thickness, position, and metal conductivity. The field distribution shows that the EM fields, especially the magnetic field, can penetrate the metallization if its relative thickness is comparable to the skin depth. This EM leakage can excite or even enhance the slow-wave mode into higher frequency regions. The metallization layer can shield the influence from the lossy semiconductor substrate only if being about 2δ to 3δ thick. In addition, the wide-used models such as the PEC, IBC, and resistance sheet are not appropriate to describe such properties. More rigorous EM modeling should be implemented for accurate interconnect design and analysis.

Based on the concept and techniques of current work, some possible areas can be developed for future study as follows.

The high-order modes for the 2-dimensional multilayered structure are important to understand the overall propagation properties, which also needs robust complex root-finding algorithms.

For current on-chip interconnect such as high-speed digital ICs, the width-to-thickness ratio is very close to one. For this structure, effects from the vertical current distribution and from current proximity on vertical sidewalls could become too significant to be neglected. Thus, the volume and surface integral equations should be used for accurate modeling.

The 3-dimensional multilayered structures, such as the discontinuities, vias, patterned or perforated ground, also have more practical significance to investigate. The general integral-equation-based approaches are more appropriate for this problem. The spectral-domain multilayered Green's function can be combined with other approaches like the spatial domain approach and mode matching method to achieve more modeling flexibility.

For the general equation-based approach, accurate evaluation of the Sommerfeld integral is always a critical task. In addition, the geometric complexity of 3-dimensional interconnect structures could bring significant computational loads to the MoM. The fast computation techniques like the fast multipole method and adaptive integral method can be applied to speedup the computation.

APPENDIX A.   The Field Distributions and Characteristic Impedance of Parallel-Plate Waveguides

This appendix introduces the formulation and procedure to evaluate the field components and characteristic impedance for the parallel-plate waveguide model. To make an explicit comparison and verification with the reference, the definition and notation are adopted as same as the ones in Williams' paper [49]. For the multilayered structure in Fig. 2.1, the TM^z mode can be defined as the A_z component from the vector magnetic potential $\mathbf{A}$.

$$E_x = -j\frac{1}{\omega\varepsilon\mu}\frac{\partial^2 A_z}{\partial x \partial z} \tag{A.1}$$

$$E_y = -j\frac{1}{\omega\varepsilon\mu}\frac{\partial^2 A_z}{\partial y \partial z} \tag{A.2}$$

$$E_z = -j\frac{1}{\omega\varepsilon\mu}\left(\frac{\partial^2}{\partial z^2} + \omega^2\varepsilon\mu\right) A_z \tag{A.3}$$

and

$$H_x = \frac{1}{\mu}\frac{\partial A_z}{\partial y} \tag{A.4}$$

$$H_y = -\frac{1}{\mu}\frac{\partial A_z}{\partial x} \tag{A.5}$$

$$H_z = 0 \tag{A.6}$$

where A_z satisfies the wave equation as

$$\nabla^2 A_z + \omega^2\varepsilon\mu A_z = 0. \tag{A.7}$$

By assuming the wave propagates in the z direction with a $e^{j\omega t}e^{-\gamma z}$ factor,[1] above wave equation becomes

$$\frac{\partial^2 A_z}{\partial y^2} + k^2 A_z = 0, \quad k^2 = \gamma^2 + \omega^2\varepsilon\mu \tag{A.8}$$

---

[1] γ is equivalent to $j\gamma_z$ that is used in Chapters 2 and 3.

where k is actually the propagation constant on y direction. This equation has the basic solution set as $\{\sin(ky), \cos(ky), \text{ or } e^{\pm jky}\}$. Moreover, the electric field and magnetic field have the following relationship

$$E_y = -\frac{\gamma}{k^2}\frac{\partial E_z}{\partial y} = -\frac{\gamma}{j\omega\varepsilon}H_x \tag{A.9}$$

$$H_x = \frac{j\omega\varepsilon}{k^2}E_z \tag{A.10}$$

while $E_x = H_y = H_z = 0$ for TM^z modes.

Using the basic solution set, the fields inside a N-layered parallel plate waveguide can be written as [49]

$$E_{z,N} = \begin{cases} \cos\left[k_N(h_N - y)\right] & (\text{PMC}) \\ \\ \sin\left[k_N(h_N - y)\right] & (\text{PEC}) \end{cases} \quad (h_{N-1} \leq y \leq h_N) \tag{A.11}$$

$$E_{z,i} = B_i \sin\left[k_i(h_i - y)\right] + C_i \cos\left[k_i(h_i - y)\right] \quad (h_{i-1} \leq y \leq h_i) \tag{A.12}$$

$$E_{z,1} = D\sin(k_1 y) \quad (\text{PEC}, h_0 \leq y \leq h_1) \tag{A.13}$$

and

$$H_{x,N} = \begin{cases} \frac{j\omega\varepsilon_N}{k_N}\sin\left[k_N(h_N - y)\right] & (\text{PMC}) \\ \\ -\frac{j\omega\varepsilon_N}{k_N}\cos\left[k_N(h_N - y)\right] & (\text{PEC}) \end{cases} \quad (h_{N-1} \leq y \leq h_N) \tag{A.14}$$

$$H_{x,i} = \frac{j\omega\varepsilon_i}{k_i}\left\{-B_i \cos\left[k_i(h_i - y)\right] + C_i \sin\left[k_i(h_i - y)\right]\right\} \quad (h_{i-1} \leq y \leq h_i) \tag{A.15}$$

$$H_{x,1} = \frac{j\omega\varepsilon_1}{k_1}D\cos(k_1 y) \quad (\text{PEC}, h_0 \leq y \leq h_1) \tag{A.16}$$

$$E_{y,N} = \begin{cases} -\frac{\gamma}{k_N}\sin\left[k_N(h_N - y)\right] & (\text{PMC}) \\ \\ \frac{\gamma}{k_N}\cos\left[k_N(h_N - y)\right] & (\text{PEC}) \end{cases} \quad (h_{N-1} \leq y \leq h_N) \tag{A.17}$$

$$E_{y,i} = \frac{\gamma}{k_i}\left\{B_i \cos\left[k_i(h_i - y)\right] - C_i \sin\left[k_i(h_i - y)\right]\right\} \quad (h_{i-1} \leq y \leq h_i) \tag{A.18}$$

$$E_{y,1} = -\frac{\gamma}{k_1}D\cos(k_1 y) \quad (\text{PEC}, h_0 \leq y \leq h_1) \tag{A.19}$$

where the maximum amplitude of E_z is normalized to unite in Nth layer. i is the layer index. B_i, C_i, and D are unknown coefficients for fields. ε_i and μ_i are the permittivity and permeability of ith layer, respectively. The continuity of E_z and H_x on interfaces gives the

solutions as

$$C_{N-1}=\begin{cases}\cos(k_N\Delta h_N) & \text{(PMC)}\\[2ex]\sin(k_N\Delta h_N) & \text{(PEC)}\end{cases} \tag{A.20}$$

$$B_{N-1}=\begin{cases}-\dfrac{k_{N-1}}{k_N}\dfrac{\varepsilon_N}{\varepsilon_{N-1}}\sin(k_N\Delta h_N) & \text{(PMC)}\\[2ex]\dfrac{k_{N-1}}{k_N}\dfrac{\varepsilon_N}{\varepsilon_{N-1}}\cos(k_N\Delta h_N) & \text{(PEC)}\end{cases} \tag{A.21}$$

$$C_i=B_{i+1}\sin(k_{i+1}\Delta h_{i+1})+C_{i+1}\cos(k_{i+1}\Delta h_{i+1}) \tag{A.22}$$

$$B_i=-\frac{k_i}{k_{i+1}}\frac{\varepsilon_{i+1}}{\varepsilon_i}\left[-B_{i+1}\cos(k_{i+1}\Delta h_{i+1})+C_{i+1}\sin(k_{i+1}\Delta h_{i+1})\right] \tag{A.23}$$

$$D=\frac{B_2\sin(k_2\Delta h_2)+C_2\cos(k_2\Delta h_2)}{\sin(k_1\Delta h_1)},\ \text{or}$$
$$=\frac{k_1}{k_2}\frac{\varepsilon_2}{\varepsilon_1}\frac{C_2\sin(k_2\Delta h_2)-B_2\cos(k_2\Delta h_2)}{\cos(k_1\Delta h_1)} \tag{A.24}$$

where $\Delta h_i = h_i - h_{i-1}$ and $2 \leq i \leq N-1$.

The characteristic impedance can also be estimated in the same way used in Chapter 5. The model voltage can be defined as following integral

$$V=-\int_{h_0}^{h_1}E_y dy-\sum_{i=2}^{N-1}\int_{h_{i-1}}^{h_i}E_y dy-\int_{h_{N-1}}^{h_N}E_y dy$$
$$=\frac{\gamma}{k_1^2}D\sin(k_1\Delta h_1)+\sum_{i=2}^{N-1}\frac{\gamma}{k_i^2}\left[B_i\sin(k_i\Delta h_i)+C_i-C_i\cos(k_i\Delta h_i)\right]$$
$$+\begin{cases}\frac{\gamma}{k_N^2}\left[1-\cos(k_N\Delta h_N)\right], & \text{(PMC)}\\[2ex]-\frac{\gamma}{k_N^2}\sin(k_N\Delta h_N), & \text{(PEC)}\end{cases} \tag{A.25}$$

The power per unit width is calculated by the integral of the Poynting vector over y as

$$P=-\int_{h_0}^{h_1}E_yH_x^* dy-\sum_{i=2}^{N-1}\int_{h_{i-1}}^{h_i}E_yH_x^* dy-\int_{h_{N-1}}^{h_N}E_yH_x^* dy$$
$$\equiv I_1+\sum_{i=2}^{N-1}I_i+I_N \tag{A.26}$$

where

$$I_1 = -\frac{j\omega\gamma\varepsilon_1^*|D|^2}{4|k_1|^2}\left\{\frac{\sin\left[2\mathrm{Re}(k_1)\Delta h_1\right]}{\mathrm{Re}(k_1)} + \frac{\sin\left[2\mathrm{Im}(k_1)\Delta h_1\right]}{\mathrm{Im}(k_1)}\right\}$$

$$I_i = -\frac{j\omega\gamma\varepsilon_i^*}{4|k_i|^2}\left\{|B|^2\frac{\sin\left[2\mathrm{Re}(k_i)\Delta h_i\right]}{\mathrm{Re}(k_i)} + |B|^2\frac{\sin\left[2\mathrm{Im}(k_i)\Delta h_i\right]}{\mathrm{Im}(k_i)}\right.$$

$$-2\mathrm{Re}(BC^*)\frac{1-\cos\left[2\mathrm{Re}(k_i)\Delta h_i\right]}{\mathrm{Re}(k_i)} + 2\mathrm{Im}(BC^*)\frac{1-\cos\left[2\mathrm{Im}(k_i)\Delta h_i\right]}{\mathrm{Im}(k_i)}$$

$$\left.-|C|^2\frac{\sin\left[2\mathrm{Re}(k_i)\Delta h_i\right]}{\mathrm{Re}(k_i)} + |C|^2\frac{\sin\left[2\mathrm{Im}(k_i)\Delta h_i\right]}{\mathrm{Im}(k_i)}\right\}$$

$$I_N = \begin{cases} \frac{j\omega\gamma\varepsilon_N^*}{4|k_N|^2}\frac{\sin[2\mathrm{Re}(k_N)\Delta h_N]}{\mathrm{Re}(k_N)} - \frac{j\omega\gamma\varepsilon_N^*}{4|k_N|^2}\frac{\sin[2\mathrm{Im}(k_N 1)\Delta h_N]}{\mathrm{Im}(k_N)} & \text{(PMC)} \\ -\frac{j\omega\gamma\varepsilon_N^*}{4|k_N|^2}\frac{\sin[2\mathrm{Re}(k_N 1)\Delta h_N]}{\mathrm{Re}(k_N)} - \frac{j\omega\gamma\varepsilon_N^*}{4|k_N|^2}\frac{\sin[2\mathrm{Im}(k_N)\Delta h_N]}{\mathrm{Im}(k_N)} & \text{(PEC)} \end{cases} \quad \text{(A.27)}$$

and the denominators are assumed to be none-zero.

The characteristic impedance Z_0 is calculated using the voltage-power definition as

$$Z_0 = \frac{|V|^2}{P^*}. \tag{A.28}$$

With the γ and Z_0 founded, the inductance L, capacitance C, conductance G, and resistance R per unit length in the transmission line model can be extracted from

$$R = \mathrm{Re}\left(\gamma Z_0\right) \tag{A.29}$$

$$L = \mathrm{Im}\left(\gamma Z_0\right)/\omega \tag{A.30}$$

$$G = \mathrm{Re}\left(\gamma/Z_0\right) \tag{A.31}$$

$$C = \mathrm{Im}\left(\gamma/Z_0\right)/\omega. \tag{A.32}$$

APPENDIX B.   The Transfer Matrices With Different Boundary Conditions

In Chapter 3, the transfer matrix method implements the chained matrices to calculate the Green's functions for multilayered structures. Up to now, the specific BCs of the lowermost h_0 and uppermost h_N layers should be taken into account. Basically, only three conditions are commonly used: the PEC (shielded), the PMC, and the open space. The open-space condition is defined as that a medium fills all the half space above or below the interface h_N or h_1. For different BCs, the matrices and unknown coefficients of potentials have different formulations.

B.1   Different Boundary Conditions on the Interface h_0

This case studies the first layer that is below the signal strip. There exist different formulations for the electric and magnetic potentials.

B.1.1   The Perfect-Electric-Conductor Boundary Condition

When the interface h_0 has the PEC BC, the general solutions for the electric and magnetic potentials are

$$
\begin{aligned}
\widetilde{\Psi}_{e,1} &= 2A_1 \sinh\left[\gamma_i(y - h_0)\right] = A_1 e^{\gamma_1 y} - A_1 e^{-\gamma_1 y} \\
\widetilde{\Psi}_{m,1} &= 2C_1 \cosh\left[\gamma_i(y - h_0)\right] = C_1 e^{\gamma_1 y} + C_1 e^{-\gamma_1 y}
\end{aligned}
\qquad (h_0 \le y \le h_1) \qquad (\text{B.1})
$$

where $B_1 = -A_1$, $D_1 = C_1$, and $h_0 = 0$. Thus the relation between the coefficients of the first and second layers on the interface $y = h_1$ can be expressed in a matrix form as

$$\begin{bmatrix} A_2 \\ B_2 \\ C_2 \\ D_2 \end{bmatrix} = \begin{bmatrix} T_2 \end{bmatrix}^{-1} \begin{bmatrix} T_1 \end{bmatrix} \begin{bmatrix} 1 & 0 & 0 & 0 \\ -e^{-2\gamma_1 \Delta h_1} & 0 & 0 & 0 \\ 0 & 0 & 1 & 0 \\ 0 & 0 & e^{-2\gamma_1 \Delta h_1} & 0 \end{bmatrix} \begin{bmatrix} A_1 e^{\gamma_1 \Delta h_1} \\ 0 \\ C_1 e^{\gamma_1 \Delta h_1} \\ 0 \end{bmatrix} \tag{B.2}$$

where $\Delta h_1 = h_1 - h_0$. Then the cascaded transfer matrices can be written as

$$\begin{bmatrix} A_t \\ B_t \\ C_t \\ D_t \end{bmatrix} = \begin{bmatrix} M_{t,t-1} \end{bmatrix} \cdots \begin{bmatrix} M_{3,2} \end{bmatrix} \begin{bmatrix} T_2 \end{bmatrix}^{-1} \begin{bmatrix} T_1 \end{bmatrix} \begin{bmatrix} 1 & 0 & 0 & 0 \\ -e^{-2\gamma_1 \Delta h_1} & 0 & 0 & 0 \\ 0 & 0 & 1 & 0 \\ 0 & 0 & e^{-2\gamma_1 \Delta h_1} & 0 \end{bmatrix} \begin{bmatrix} A_1 e^{\gamma_1 \Delta h_1} \\ 0 \\ C_1 e^{\gamma_1 \Delta h_1} \\ 0 \end{bmatrix}. \tag{B.3}$$

And the corresponding $\widetilde{A}$ and $\widetilde{C}$ are defined as

$$\begin{bmatrix} \widetilde{A} \\ 0 \\ \widetilde{C} \\ 0 \end{bmatrix} = \begin{bmatrix} A_1 e^{\gamma_1 \Delta h_1} \\ 0 \\ C_1 e^{\gamma_1 \Delta h_1} \\ 0 \end{bmatrix}. \tag{B.4}$$

B.1.2   The Perfect-Magnetic-Conductor Boundary Condition

The general solutions for the potential are

$$\begin{aligned} \widetilde{\Psi}_{e,1} &= 2A_1 \cosh\left[\gamma_i(y - h_0)\right] = A_1 e^{\gamma_1 y} + A_1 e^{-\gamma_1 y} \\ \widetilde{\Psi}_{m,1} &= 2C_1 \sinh\left[\gamma_i(y - h_0)\right] = C_1 e^{\gamma_1 y} - C_1 e^{-\gamma_1 y} \end{aligned} \quad (0 \le y \le h_1) \tag{B.5}$$

where $B_1 = A_1$, $D_1 = -C_1$. Thus the relation between the coefficients of the first and second layers on the interface $y = h_1$ can be expressed in a matrix form as

$$\begin{bmatrix} A_2 \\ B_2 \\ C_2 \\ D_2 \end{bmatrix} = \begin{bmatrix} T_2 \end{bmatrix}^{-1} \begin{bmatrix} T_1 \end{bmatrix} \begin{bmatrix} 1 & 0 & 0 & 0 \\ e^{-2\gamma_1 \Delta h_1} & 0 & 0 & 0 \\ 0 & 0 & 1 & 0 \\ 0 & 0 & -e^{-2\gamma_1 \Delta h_1} & 0 \end{bmatrix} \begin{bmatrix} A_1 e^{\gamma_1 \Delta h_1} \\ 0 \\ C_1 e^{\gamma_1 \Delta h_1} \\ 0 \end{bmatrix}. \tag{B.6}$$

The relation of (B.4) still holds for the PMC BC.

B.1.3   The Open-Space Boundary Condition

When the interface h_0 becomes open, the general solutions for the electrical and magnetic potentials become

$$
\begin{aligned}
\widetilde{\Psi}_{e,1} &= A_1 e^{\gamma_1(y-h_1)} \\
\widetilde{\Psi}_{m,1} &= C_1 e^{\gamma_1(y-h_1)}
\end{aligned}
\quad (y \leq h_1)
\tag{B.7}
$$

where $B_1 = D_1 = 0$. The transfer matrices has the form

$$
\begin{bmatrix} A_t \\ B_t \\ C_t \\ D_t \end{bmatrix}
= \begin{bmatrix} M_{t,t-1} \end{bmatrix} \begin{bmatrix} M_{t-1,t-2} \end{bmatrix} \cdots \begin{bmatrix} M_{3,2} \end{bmatrix} \begin{bmatrix} T_2 \end{bmatrix}^{-1} \begin{bmatrix} T_1 \end{bmatrix}
\begin{bmatrix} 1 & \\ & 0 \\ & 1 \\ & 0 \end{bmatrix}
\begin{bmatrix} A_1 \\ 0 \\ C_1 \\ 0 \end{bmatrix}
\tag{B.8}
$$

The $\widetilde{A}$ and $\widetilde{C}$ become

$$
\begin{bmatrix} \widetilde{A} \\ 0 \\ \widetilde{C} \\ 0 \end{bmatrix}
= \begin{bmatrix} A_1 \\ 0 \\ C_1 \\ 0 \end{bmatrix}.
\tag{B.9}
$$

B.2   Different Boundary Conditions on the Interface h_N

The last layer is above the signal strip. Similarly, the BCs are discussed as follows.

B.2.1   The Perfect-Electric-Conductor Boundary Condition

When the interface h_N has the PEC BC, the general solutions for the potentials are

$$
\begin{aligned}
\widetilde{\Psi}_{e,N} &= -2B_N \sinh\left[\gamma_N(y-h_N)\right] = -B_N e^{\gamma_N(y-h_N)} + B_N e^{-\gamma_N(y-h_N)} \\
\widetilde{\Psi}_{m,N} &= 2D_N \cosh\left[\gamma_N(y-h_N)\right] = D_N e^{\gamma_N(y-h_N)} + D_N e^{-\gamma_N(y-h_N)}
\end{aligned}
\tag{B.10}
$$

or

$$
\begin{aligned}
\widetilde{\Psi}_{e,N} &= -B_N e^{-\gamma_N(h_N-y)} + B_N e^{\gamma_N(h_N-y)} \\
\widetilde{\Psi}_{m,N} &= D_N e^{-\gamma_N(h_N-y)} + D_N e^{\gamma_N(h_N-y)}
\end{aligned}
\tag{B.11}
$$

where $A_N = -B_N$, $C_N = D_N$, and $h_{N-1} \le y < h_N$. The relation between the coefficients of the Nth and $(N-1)$th layers can be expressed in a matrix form on the interface h_{N-1} as

$$
\begin{bmatrix} A_{N-1} \\ B_{N-1} \\ C_{N-1} \\ D_{N-1} \end{bmatrix} = \begin{bmatrix} T_{N-1} \end{bmatrix}^{-1} \begin{bmatrix} T_N \end{bmatrix} \begin{bmatrix} 0 & -e^{-2\gamma_N \Delta h_N} & 0 & 0 \\ 0 & 1 & 0 & 0 \\ 0 & 0 & 0 & e^{-2\gamma_N \Delta h_N} \\ 0 & 0 & 0 & 1 \end{bmatrix} \begin{bmatrix} 0 \\ B_N e^{\gamma_N \Delta h_N} \\ 0 \\ D_N e^{\gamma_N \Delta h_N} \end{bmatrix}. \tag{B.12}
$$

Thus the cascaded transfer matrices can be written as

$$
\begin{bmatrix} A_{t+1} \\ B_{t+1} \\ C_{t+1} \\ D_{t+1} \end{bmatrix} = \begin{bmatrix} M'_{t+1,t+2} \end{bmatrix} \begin{bmatrix} M'_{t+2,t+3} \end{bmatrix} \cdots \begin{bmatrix} M'_{N-2,N-1} \end{bmatrix} \begin{bmatrix} T_{N-1} \end{bmatrix}^{-1} \begin{bmatrix} T_N \end{bmatrix}
$$
$$
\begin{bmatrix} 0 & -e^{-2\gamma_N \Delta h_N} & 0 & 0 \\ 0 & 1 & 0 & 0 \\ 0 & 0 & 0 & e^{-2\gamma_N \Delta h_N} \\ 0 & 0 & 0 & 1 \end{bmatrix} \begin{bmatrix} 0 \\ B_N e^{\gamma_N \Delta h_N} \\ 0 \\ D_N e^{\gamma_N \Delta h_N} \end{bmatrix} \tag{B.13}
$$

where $\Delta h_N = h_N - h_{N-1}$. And $\widetilde{B}$ and $\widetilde{D}$ are defined as

$$
\begin{bmatrix} 0 \\ \widetilde{B} \\ 0 \\ \widetilde{D} \end{bmatrix} = \begin{bmatrix} 0 \\ B_N e^{\gamma_N \Delta h_N} \\ 0 \\ D_N e^{\gamma_N \Delta h_N} \\ 0 \end{bmatrix}. \tag{B.14}
$$

B.2.2   The Perfect-Magnetic-Conductor Boundary Condition

When the interface h_N has the PMC BC, the general solutions for the potentials are

$$
\begin{aligned}
\widetilde{\Psi}_{e,N} &= 2B_N \cos\left[\gamma_N(y - h_N)\right] = B_N e^{-\gamma_N(h_N - y)} + B_N e^{\gamma_N(h_N - y)} \\
\widetilde{\Psi}_{m,N} &= -2D_N \sinh\left[\gamma_N(y - h_N)\right] = -D_N e^{-\gamma_N(h_N - y)} + D_N e^{\gamma_N(h_N - y)}
\end{aligned} \tag{B.15}
$$

where $A_N = B_N$, $C_N = -D_N$, and $h_{N-1} \leq y < h_N$. The relation same as (B.12) is expressed in matrix form on the interface $y = h_{N-1}$ as

$$
\begin{bmatrix} A_{N-1} \\ B_{N-1} \\ C_{N-1} \\ D_{N-1} \end{bmatrix} = \begin{bmatrix} T_{N-1} \end{bmatrix}^{-1} \begin{bmatrix} T_N \end{bmatrix} \begin{bmatrix} 0 & e^{-2\gamma_N \Delta h_N} & 0 & 0 \\ 0 & 1 & 0 & 0 \\ 0 & 0 & 0 & -e^{-2\gamma_N \Delta h_N} \\ 0 & 0 & 0 & 1 \end{bmatrix} \begin{bmatrix} 0 \\ B_N e^{\gamma_N \Delta h_N} \\ 0 \\ D_N e^{\gamma_N \Delta h_N} \end{bmatrix} \tag{B.16}
$$

The relation (B.14) is also correct for the PMC BC.

B.2.3 The Open-Space Boundary Condition

When the interface h_N becomes open, the general solutions for the electrical and magnetic potentials become

$$
\begin{aligned}
\widetilde{\Psi}_{e,N} &= B_N e^{-\gamma_N(y-h_{N-1})} \\
\widetilde{\Psi}_{m,N} &= D_N e^{-\gamma_N(y-h_{N-1})}
\end{aligned} \qquad (h_{N-1} \leq y) \tag{B.17}
$$

where $A_N = C_N = 0$, and . The transfer matrices become

$$
\begin{bmatrix} A_{t+1} \\ B_{t+1} \\ C_{t+1} \\ D_{t+1} \end{bmatrix} = \begin{bmatrix} M'_{t+1,t+2} \end{bmatrix} \cdots \begin{bmatrix} M'_{N-2,N-1} \end{bmatrix} \begin{bmatrix} T_{N-1} \end{bmatrix}^{-1} \begin{bmatrix} T_N \end{bmatrix} \begin{bmatrix} 0 & & & \\ & 1 & & \\ & & 0 & \\ & & & 1 \end{bmatrix} \begin{bmatrix} 0 \\ B_N \\ 0 \\ D_N \end{bmatrix}. \tag{B.18}
$$

Now the $\widetilde{B}$ and $\widetilde{D}$ are defined as

$$
\begin{bmatrix} 0 \\ \widetilde{B} \\ 0 \\ \widetilde{D} \end{bmatrix} = \begin{bmatrix} 0 \\ B_N \\ 0 \\ D_N \\ 0 \end{bmatrix}. \tag{B.19}
$$

To this point, all the coefficients $\widetilde{A}$, $\widetilde{B}$, $\widetilde{C}$, and $\widetilde{D}$ are explicitly defined based on different BCs.

APPENDIX C.   List of Abbreviations

BCs	boundary conditions
CAD	computer-aided design
dc	direct current
EM	electromagnetic
EMI	electromagnetic interference
FD	finite difference
FDTD	finite difference in time domain
FEM	finite element method
FFT	fast Fourier transform
IBC	impedance boundary condition
ICs	integrated circuits
IEM	inverted embedded microstrip
ITRS	International Technology Roadmap for Semiconductors
LSE	longitudinal-section electric
LSM	longitudinal-section magnetic
MIMI	metal-insulator-metal-insulator
MIMS	metal-insulator-metal-semiconductor
MIS	metal-insulator-semiconductor
MoL	method of lines
MoM	method of moments
PEC	perfect electric conductor
PMC	perfect magnetic conductor
R-card	resistive sheet
RFICs	radio-frequency integrated circuits
RLCG	resistance, inductance, capacitance, and conductance
SDA	spectral domain approach
SDIA	spectral-domain immitance approach
SWF	slow-wave factor
TE	transverse electric
TEM	transverse electromagnetic
TFMSL	thin-film microstrip line
TLM	transmission line matrix
TM	transverse magnetic
VLSI	very-large-scale integration

BIBLIOGRAPHY

[1] International Technology Roadmap for Semiconductors. (2006). ITRS Reports, 2006 Update. [Online]. Available: http://www.itrs.net/reports.html (Last accessed date: Nov. 2007)

[2] A. E. Ruehli and A. C. Cangellaris, "Progress in the methodologies for the electrical modeling of interconnects and electronic packaging," *Proc. IEEE*, vol. 89, no. 5, pp. 740-771, May 2001.

[3] T. C. Edwards and M. B. Steer, *Foundations of Interconnect and Microstrip Design*, 3rd ed., New York: John Wiley & Sons, Ltd., 2000.

[4] D. D. Grieg and H. F. Englemann, "Microstrip-a new transmission technique for the kilomegacycle range," *Proc. IRE*, vol. 40, no. 12, pp. 1644-1650, Dec. 1952.

[5] J. A. Wait, *Electromagnetic Waves in Stratified Media*, Oxford: Pergamon Press, 1996.

[6] A. Bhattacharyya, *Electromagnetic Fields in Multilayered Structures: Theory and Application*, Boston: Artech House, 1994.

[7] W. C. Chew, *Waves and Fields in Inhomogeneous Media*, New York: IEEE press, Inc., 1995.

[8] R. K. Hoffmann, *Handbook of Microwave Integrated Circuits*, Norwood: Artech House, Inc., 1987.

[9] C. Nguyen, *Analysis Methods for RF, Microwave, and Millimeter-Wave Planar Transmission Line Structures*, New York: John Wiley & Sons, Inc., 2000.

[10] H. A. Wheeler, "Transmission-line properties of parallel wide strips by conformal mapping approximation," *IEEE Trans. Microw. Theory Tech.*, vol. 12, no. 3, pp. 280-289, May 1964.

[11] H. A. Wheeler, "Transmission-line properties of parallel wide strips separated by a dielectric sheet," *IEEE Trans. Microw. Theory Tech.*, vol. 13, no. 2, pp. 172-185, Mar. 1965.

[12] E. Yamashita and R. Mittra, "Variational method for the analysis of microstrip lines," *IEEE Trans. Microw. Theory Tech.*, vol. 16, no. 4, pp. 251-256, Apr. 1968.

[13] F. Medina and M. Horno, "Determination of Green's function matrix for multiconductor and anisotropic multidielectric planar transmission lines: a variational approach," *IEEE Trans. Microw. Theory Tech.*, vol.33, no. 10, pp. 933-940, Oct. 1985

[14] C. Wei, R. F. Harrington, J. R. Mautz, and T. K. Sarkar, "Multiconductor transmission lines in multilayered dielectric media, " *IEEE Trans. Microw. Theory Tech.*, vol. 32, no. 4, pp. 439-450, Apr. 1984.

[15] T. Itoh, "Generalized spectral domain method for multiconductor printed lines and its application toturnable suspended microstrips," *IEEE Trans. Microw. Theory Tech.*, vol. 26, no. 12, pp. 983-987, Dec. 1978.

[16] H. E. Green, "The numerical solution of some important transmission-line problems," *IEEE Trans. Microw. Theory Tech.*, vol. 13, no. 5, pp. 676-692, Sep. 1965.

[17] M. I. Aksun and G. Dural, "Clarification of issues on the closed-form Green's functions in stratified media," *IEEE Trans. Antennas Propag.*, vol. 53, no. 11, pp. 3644-3653, Nov. 2005.

[18] K. A. Michalski and J. R. Mosig, "Multilayered media Green's functions in integral equation formulations," *IEEE Trans. Antennas and Propag.*, vol. 45, no. 3, pp. 508-519, Mar. 1997.

[19] J. R. Mosig, "Arbitrarily shaped microstrip structures and their analysis with amixed potential integral equation," *IEEE Trans. Microw. Theory Tech.*, vol. 36, no. 2, pp. 314-323, Feb. 1988.

[20] E. J. Denlinger, "A frequency dependent solution for microstrip transmission lines," *IEEE Trans. Microw. Theory Tech.*, vol. 19, no. 1, pp. 30-39, Jan. 1971.

[21] T. Itoh and R. Mittra, "Spectral-domain approach for calculating the dispersion characteristics of microstrip lines," *IEEE Trans. Microw. Theory Tech.*, vol. 21, no. 7, pp. 496-499, Jul. 1973.

[22] J. B. Davies and D. Mirshekar-Syahkal, "Spectral-domain solution of arbitrary coplanar transmission line with multilayer substrate," *IEEE Trans. Microw. Theory Tech.*, vol. 25, no. 2, pp. 143-146, Feb. 1977.

[23] T. Itoh, "Spectral domain immitance approach for dispersion characteristics of generalized printed transmission lines," *IEEE Trans. Microw. Theory Tech.*, vol. 28, no. 7, pp. 733-736, Jul. 1980.

[24] D. Mirshekar-Syahkal, "An accurate determination of dielectric loss effect in monolithic microwave integrated circuits including microstrip and coupled microstrip lines," *IEEE Trans. Microw. Theory Tech.*, vol. 31, no. 11, pp. 950-954, Nov. 1983.

[25] D. Mirshekar-Syahkal, *Spectral Domain Method for Microwave Integrated Circuits*, New York: John Wiley & Sons, Ltd., 1990.

[26] R. H. Jansen, "The spectral-domain approach for microwave integrated circuits," *IEEE Trans. Microw. Theory Tech.*, vol. 33, no. 10, pp. 1043-1056, Oct. 1985

[27] T. Itoh and W. Menzel, "A full-wave analysis method for open microstrip structures," *IEEE Trans. Antennas Propag.*, vol. 29, no. 1, pp. 63-67, Jan. 1981.

[28] T. Livernois and P. Katehi, "A generalized method for deriving the space-domain Green's function in a shielded, multilayer substrate structure with application to MIS slow-wave transmission lines," *IEEE Trans. Microw. Theory Tech.*, vol. 34, no. 12, pp. 1483-1489, Dec. 1986.

[29] Y. L. Chow, J. J. Yang, D. G. Fang, and G. E. Howard, "A closed-form spatial Green's function for the thick microstripsubstrate," *IEEE Trans. Microw. Theory Tech.*, vol. 39, no. 3, pp. 588-592, Mar. 1991.

[30] J. S. Hornsby and A. G. Gopinath, "Numerical analysis of a dielectric-loaded waveguide with a microstrip line-finite difference methods," *IEEE Trans. Microw. Theory Tech.*, vol. 17, no. 9, pp. 684-690, Sep. 1969.

[31] D. G. Corr and J. B. Davies, "Computer analysis of the fundamental and high order modes in single and coupled microstrip," *IEEE Trans. Microw. Theory Tech.*, vol. 20, no. 10, pp.669-678, Oct. 1972.

[32] P. Daly, " Hybrid mode analysis of microstrip by finite-element method," *IEEE Trans. Microw. Theory Tech.*, vol. 19, no.1, pp.19-25, Jan. 1971.

[33] B. M. A. Rahman, F. A. Fernandez, and J. B. Davies, "Review of finite element methods for microwave and opticalwaveguides," *Proc. IEEE*, vol. 79, no. 10, pp1442-1448, Oct.1991.

[34] K. M. Rahman and C. Nguyen, "Full-wave analysis of coplanar strips considering the finite metallization thickness," *IEEE Trans. Microw. Theory Tech.*, vol. 42, no. 11, pp. 2177-2179, Nov. 1994.

[35] A. C. Polycarpou, P. A. Tirkas, and C. A. Balanis, "The finite-element method for modeling circuits and interconnects for electronic packaging," *IEEE Trans. Microw. Theory Tech.*, vol. 45, no. 2, pp. 1868 -1874, Oct. 1997.

[36] F. J. Schmuckle and R. Pregla, "The method of lines for the analysis of planar waveguides withfinite metallization thickness," *IEEE Trans. Microw. Theory Tech.*, vol. 39, no. 1, pp. 107-111, Jan. 1991

[37] W. Heofer, "The transmission line matrix method-theory and applications," *IEEE Trans. Microw. Theory Tech.*, vol. 33, no. 10, pp.882-893, Oct. 1985.

[38] Y. J. Zhao, K. L. Wu, and K. M. Chen, "A compact 2-D full-wave finite-difference frequency-domain method for general guided wave structures," *IEEE Trans. Microw. Theory Tech.*, vol. 50, no. 7, pp. 1844-1848, Jul. 2002.

[39] T. Shibata and E. Sano, "Characterization of MIS structure coplanar transmission lines for investigation of signal propagation in integrated circuits," *IEEE Trans. Microw. Theory Tech.*, vol. 38, no. 7, pp. 881-890, Jul. 1990.

[40] J. G. Yook, N. I. Dib, and L. P. B. Katehi, "Characterization of high frequency interconnects using finite difference time domain and finite element methods, " IEEE Transactions on Microwave Theory and Techniques, vol. 42, no. 9, pp. 1727-1736, Sep. 1994.

[41] Y. Fukuoka, Y. C. Shih, and T. Itoh, "Analysis of slow-wave coplanar waveguide for monolithic integrated circuits," *IEEE Trans. Microw. Theory Tech.*, vol. 31, no. 7, pp. 567-573, Jul. 1983.

[42] W. Heinrich, "Full-wave analysis of conductor losses on MMIC transmission lines," *IEEE Trans. Microw. Theory Tech.*, vol. 38, no. 10, pp. 1468-1472, Oct. 1990.

[43] T. Itoh, *Numerical Techniques for Microwave and Millimeter-Wave Passive Structure*, New York: John Wiley & Songs Inc., 1989.

[44] H. Guckel, P. A. Brennan, and I. Palócz, "A parallel-plate waveguide approach to micro-miniaturized, planar transmission lines for integrated circuits," *IEEE Trans. Microw. Theory Tech.*, vol. 15, no. 8, pp. 468-476, Aug. 1967.

[45] H. Hasegawa, M. Furukawa, and H. Yanai, "Properties of microstrip line on Si-SiO$_2$ system," *IEEE Trans. Microw. Theory Tech.*, vol. 19, no. 11, pp. 869-881, Nov. 1971.

[46] D. Jäger, "Slow-wave propagation along variable Schottky-contact microstrip line," *IEEE Trans. Microw. Theory Tech.*, vol. 24, no. 9, pp. 566-573, Sep. 1976.

[47] P. Kennis and L. Faucon, "Rigorous analysis of planar MIS transmission lines," *Electr. Lett.*, vol. 17, no. 13, pp. 454-456, Jun. 1981.

[48] G. Cano, F. Medina, and M. Horno, "Efficient spectral domain analysis of generalized multistrip lines in stratified media including thin, anisotropic and lossy substrates," *IEEE Trans. Microw. Theory Tech.*, vol. 40, no. 2, pp. 217-227, Feb. 1992.

[49] D. F. Williams, "Metal-insulator-semiconductor transmission lines," *IEEE Trans. Microw. Theory Tech.*, vol. 47, no. 2, pp. 176-181, Feb. 1999.

[50] J. D. Morsey, V. I. Okhmatovski, and A. C. Cangellaris, "Finite-thickness conductor models for full-wave analysis of interconnects with a fast integral equation method," *IEEE Adv. Packag.*, vol. 27, no. 1, pp. 24-33, Feb. 2004.

[51] G. Plaza, R. Marqués, and F. Medina, "Quasi-TM MoL/MoM approach for computing the transmission-line parameters of lossy lines," *IEEE Trans. Microw. Theory Tech.*, vol. 54, no. 1, pp. 198-209, Jan. 2006.

[52] N. K. Das and D. M. Pozar, "A generalized spectral-domain Green's function for multilayer dielectric substrate with application to multilayer transmission lines," *IEEE Trans. Microw. Theory Tech.*, vol. 35, pp. 326-335, Mar. 1987.

[53] N. K. Das and D. M. Pozar, "Full-wave spectral-domain computation of material, radiation, and guided wave losses in infinite multilayered printed transmission lines," *IEEE Trans. Microw. Theory Tech.*, vol. 39, no. 1, pp. 54-63, Jan. 1991.

[54] R. V. Hippel, *Dielectrics and Waves.* New York: John Wiley & Sons, Inc., 1954.

[55] H. Hasegawa and H. Yanai, "Characteristics of parallel-plate waveguide filled with a silicon-siliconxide system," *Electronics and Communications in Japan*, vol. 53-B, no. 10, pp. 63-73, 1970.

[56] G. A. Balanis, *Advanced Engineering Electromagnetics*, New York: John Wiley & Sons Inc., 1989.

[57] R. E. Collin, *Field Theory of Guided Waves*, 2nd ed., New York: IEEE, Inc., 1991.

[58] R. F. Harrington, *Field Computation by Moment Methods*, London: Collier-Macmillan Ltd., 1968.

[59] T. Leung and C. A. Balanis, "Pulse dispersion distortion in open and shielded microstrips using the spectral-domain method," *IEEE Trans. Microw. Theory Tech.*, vol. 36, no. 7, pp. 1223-1226, Jul. 1988.

[60] T. Senior, "Approximate boundary conditions," *IEEE Trans. Antennas Propag.*, vol. 29, no. 5, pp. 826-829, Sep. 1981.

[61] D. C. Jenn, A. Prata Jr., W. V. T Rusch, and M. R. Barclay, "A resistive sheet approximation for mesh reflector antennas," *IEEE Trans. Antennas Propag.*, vol. 37, no 11. 1484-1486, Nov. 1989.

[62] S. Amari and J. Bornemann, "LSE- and LSM- mode sheet impedances of thin conductors," *IEEE Trans. Microw. Theory Tech.*, vol. 44, no. 6, pp. 967-970, Jun. 1996.

[63] J. P. Gilb and C. A. Balanis, "MIS slow-wave structures over a wide range of paramters," *IEEE Trans. Microw. Theory Tech.*, vol. 40, no. 12, pp. 2148-2154, Dec. 1992.

[64] M. Konno, "Conductor loss in thin-film tranmission lines," *Electronics and Communications in Japan*, pt. 2, vol. 82, no. 10, pp. 83-91, Sep. 1999.

[65] R. C. Hansen and W. T. Pawlewicz, "Effective conductivity and microwave reflectivey of thin metallic films," *IEEE Trans. Microw. Theory Tech.*, vol. 30, no. 11, pp. 2064-2006, Nov. 1982.

[66] R. F. Harrington and J. R. Mautz, "An impedance sheet approximation for thin dielectric shells," *IEEE Trans. Antennas Propag.*, vol. 35, no. 4, pp. 531-534, Jul. 1975.

[67] R. T. Kollipara, "Dispersion characteristics of moderately thick microstrip lines by the spectral domain method," *IEEE Trans. Microw. Guid. Wave Lett.*, vol. 2, no. 3, pp. 100-101, Mar. 1992.

[68] J. C. Rautio and V. Demir, "Microstrip conductor loss models for electromagnetic analysis," *IEEE Trans. Microw. Theory Tech.*, vol. 51, no. 8, pp. 915-921, Mar. 2003.

[69] J. M. Pond, C. M. Krowne, and W. Carter, "On the application of complex resistive boundary conditions to model transmission lines consisting of very thin superconductors," *IEEE Trans. Microw. Theory Tech.*, vol. 37, no. 1, pp. 181-190, Jan. 1989.

[70] C. M. Krowne, "Relationships for Green's function spectral dyadics involving anisotropic impedance conductors imbedded in layered anisotropic media," *IEEE Trans. Antennas Propag.*, vol. 37, no. 9, pp. 1207-1211, Sep. 1999.

[71] T. E. Deventer, P. B. Katehi, and A. C. Cangellaris, "An integral equation method for the evaluation of conductor and dielectric losses in high-frequency interconnects," *IEEE Trans. Microw. Theory Tech.*, vol. 37, no. 12, pp. 1964-1972, Dec. 1989.

[72] J. C. Liou and K. M. Lau, "Analysis of slow-wave transmission lines on multi-layered semiconductor structures including conductor loss," *IEEE Trans. Microw. Theory Tech.*, vol. 41, no. 5, pp. 824-829, May 1993.

[73] J. Aguilera, R. Marqués, and M. Horno, "Quasi-TEM surface impedance approaches for the analysis of MIC and MMIC transmission lines, including both conductor and substrate loss," *IEEE Trans. Microw. Theory Tech.*, vol. 43, no. 7, pp. 1553-1558, Jul. 1995.

[74] C. M. Krowne, "Dyadic Green's function modifications for obtaining attenucation in microstrip transmission layered structures with complex media," *IEEE Trans. Microw. Theory Tech.*, vol. 50, no. 1, pp. 112-122, Jan. 2002.

[75] A. N. Deleniv, M. S. Gashinova, and I. B. Vendik, "SDA full-wave analysis of boxed multistrip superconducting lines of finite thickness embedded in a layered lossy medium," *IEEE Trans. Microw. Theory Tech.*, vol. 51, no. 1, pp. 74-81, Jan. 2003.

[76] J. Y. Ke and C. H. Chen, "Modified spectral-domain approach for microstrip lines with finite metallization thickness and conductivity," *IEE Proc.-Microw. Antennas Propag.*, vol.142, no. 4, pp. 357-363, Aug. 1995.

[77] J. F. Kiang, "Integral equation solution to the skin effect problem in conductor strips of finite thickness," *IEEE Trans. Microw. Theory Tech.*, vol. 39, no. 3, pp. 452-460, Mar. 1991.

[78] M. Farina and T. Rozzi, "Spectral domain approach to 2D-modelling of open planar structures with thick lossy conductors," *IEE Proc.-Microw. Antennas Propag.*, vol.147, no. 5, pp. 321-324, Oct. 2000.

[79] I. P. Theron and J. H. Cloete, "On the surface impedance used to model the conductor losses of microstrip structures," *IEE Proc.-Microw. Antennas Propag.*, vol.142, no. 1, pp. 35-40, Feb. 1995.

[80] J. P. Gilb and C. A. Balanis, "Pulse distortion on multilayer coupled microstrip lines," *IEEE Trans. Microw. Theory Tech.*, vol. 37, no. 10, pp. 1620-1628, Oct. 1989.

[81] J. H. Mathews and K. D. Fink, *Numerical Methods Using MATLAB*, 4th ed., New Jersey: Pearson Education, Inc., 1999.

[82] A. F. Peterson, *Computational Methods to Electromagnetics*, New York: John Wiley & Sons, Inc., 1998.

[83] K. A. Michalski, "Extrapolation methods for Sommerfeld integral tails," *IEEE Trans. Antennas and Propag.*, vol. 46, no. 10, pp. 1405-1418, Oct. 1998.

[84] M. Kobayashi and F. Ando "Dispersion characteristics of open microstrip lines," *IEEE Trans. Microw. Theory Tech.*,vol. 35, no. 2, pp.101-105, Feb, 1987.

[85] F. Schnieder and W. Heinrich, "Model of thin-film microstrip line for circuit design," *IEEE Trans. Microw. Theory Tech.*, vol. 49, no. 1, pp. 104-110, Jan. 2001.

[86] P. Pramanick and P. Bhartia, "An accurate description of dispersion in microstrip," *Microwave Journal*, vol. 26, pp. 89-96, Dec. 1983.

[87] H. Braunisch and D. H. Han, "Broadband characterization of package dielectrics," in *IEEE Electronic Components and Technology Conference Proceedings.*, 2003, pp. 1258-1263.

[88] R. D. Lutz, V. K. Tripathi and A. Weisshaar, "Enhanced transmission characteristics of on-chip interconnects with orthogonal gridded shield," *IEEE Adv. Packag.*, vol. 24, no. 3, pp. 288-293, Aug. 2001.

[89] C. Y. Ng, M. Chongcheawchamnan, M. S. Aftanasar, I. D. Robertson, P. R. Young, and J. Minalgiene,"Characterisation of TFMS lines fabricated using photoimageable thick-film technology," *IEE Proc.-Microw. Antennas Propag.*, vol. 150, no. 3, pp. 125-130, Jun. 2003.

[90] W. Ryu, S. H. Baik, H. Kim, J. Kim, M. Sung and, J. Kim, "Embedded microstrip interconnection lines for gigahertz digital circuits," *IEEE Adv. Packag.*, vol. 23, no. 3, pp. 495-503, Aug. 2000.